Self-assembly of dipolar particles

Ludovic Spiteri

UNIVERSITÉ DE LORRAINE

Laboratoire Physique et Chimie Théoriques

ÉCOLE DOCTORALE C2MP
Chimie Mécanique Matériaux Physique

T H È S E

pour obtenir le titre de

Docteur de l'Université de Lorraine

Mention : Physique

Présentée par

Ludovic SPITERI

Self-assembly of dipolar particles

soutenue le 21 décembre 2018

Jury :

Rapporteurs :	Jean-François JOANNY	-	ESPCI Paris
	Alois WÜRGER	-	Université de Bordeaux
Examinateurs :	Hervé MOHRBACH	-	Université de Lorraine
	Igor M. KULIĆ	-	Institut Charles Sadron
Directeur :	René MESSINA	-	Université de Lorraine
Co-directrice :	Lydiane BÉCU	-	Université de Lorraine

Laboratoire de Physique et Chimie Théoriques (LPCT) - UMR CNRS 7019
Université de Lorraine, 1, Boulevard Arago, 57070 Metz, France

Remerciements

Avant toutes choses, si ces trois années de recherches ont pu aboutir à l'ensemble des résultats présentés dans ce manuscrit de thèse, c'est grâce à mon directeur de thèse René Messina. Je le remercie de m'avoir proposé un sujet de thèse passionnant et d'avoir toujours fait preuve d'une grande disponibilité, de beaucoup de pédagogie, de dynamisme et d'encouragement. J'ai ainsi pu bénéficier de très bonnes conditions pour progresser et mener à bien cette thèse. Je souhaite aussi grandement remercier Lydiane Bécu en tant que co-directrice, Igor Stanković, David Gonzalez-Rodriguez et Hervé Mohrbach qui ont prêté leur talent à l'accomplissement de ces travaux de recherche. Merci d'avoir toujours été disponible pour m'apporter aide et conseils avisés avec gentillesse. J'ai aussi eu la chance de pouvoir échanger avec d'autres personnalités du laboratoire aux qualités scientifiques et humaines remarquables, Martin M. Müller, Yves Grandati, Claude Dal Capello et Alain Berard. Je souhaite également remercier les responsables et personnels de l'école doctorale C2MP/SESAMES et des laboratoires LPCT et LCP-A2MC pour leur accueil et leur appui indispensable à la réalisation de cette thèse. Ayant été un utilisateur assidu du cluster, je remercie Philippe Senot et Étienne Gallant de m'avoir fourni tous les outils nécessaires à son utilisation.

Je n'aurai pas pu réaliser tout cela sans l'indéfectible soutien moral de ma famille. Je remercie mes parents, mon grand frère et surtout ma petite sœur à qui j'adresse un remerciement tout particulier pour avoir toujours pris très soin de moi. Je souhaite aussi remercier deux de ses amies, Juliette Stinco et Angélique Alexandre, pour leur sollicitude. Je suis extrêmement reconnaissant envers mes amis les proches pour leur indispensable soutien, à commencer par ma meilleure amie, Christelle Lisowski, qui me supporte (dans tous les sens du terme) depuis plus d'une dizaine d'années. Merci d'avoir toujours été présente, attentive, patiente et d'être née quatre jours seulement après moi, je me sens vieillir moins seul, merci ! Je remercie Thomas Szostok pour l'amitié et l'intérêt sincère qu'il me porte depuis plusieurs années, ce qui compte énormément pour moi. Merci à Kheira Oudina pour son inestimable bienveillance à mon égard, ainsi qu'à Giordano Benacchio pour toute sa considération. Bien évidemment, je n'oublie pas les camarades et collègues rencontrés durant mon parcours universitaire, qui sont aussi devenus des amis, Feng Yan, Da Li, Wen Luo, Enhao Chou, Moussa Diallo, Moussa Seydi et Ali Mourad. Merci pour votre attention et votre gentillesse.

Je souhaite finalement exprimer ma grande reconnaissance envers Jean-François Joanny et Alois Würger, qui m'ont fait l'honneur de bien vouloir être rapporteurs de cette thèse, ainsi que Igor M. Kulić d'avoir accepté d'examiner cette thèse.

Résumé

Chapitre 1 : Introduction

L'auto-assemblage est défini comme un processus par lequel des composants désordonnés forment spontanément et de façon autonome des structures ou des motifs ordonnés. Il s'agit aussi d'un phénomène omniprésent générateur d'ordre dans la nature : la formation des membranes cellulaires, des systèmes planétaires ou des cristaux en sont quelques exemples. L'auto-assemblage des particules dipolaires comme méthode ascendante (dite "bottom-up") offre une nouvelle voie pour la fabrication de matériaux fonctionnels. Actuellement, les systèmes dipolaires servent au développement de nombreuses applications telles que les valves, les absorbeurs de choc, les cristaux photoniques et même à l'élaboration de nouveaux traitements médicaux. Par ailleurs, les systèmes dipolaires sont abondants en physique de la matière condensée (molécules et nanoparticules ferromagnétiques, particules colloidales magnétiques, bactérie magnétotactique, ...). Ils représentent un défi important du fait de l'anisotropie et de la longue portée de l'interaction dipôle-dipôle. De manière générale, l'auto-assemblage de particules magnétiques est essentiellement gouverné par la recherche d'un niveau d'énergie minimal. Le principal objectif de ce travail de recherche est de prédire les microstructures des ces systèmes en considérant de façon adéquate l'interaction complexe dipôle-dipôle ainsi que les effets stériques et ceux dus à un éventuel confinement. Les aimants sphériques tendent naturellement à s'organiser en chaînes, et ce, même en l'absence de champ magnétique. Ces dernières représentent un système ordonné simple et facilement réalisable en appliquant un champ magnétique extérieur. De nombreuses structures peuvent être comprises (ou déduite) à partir de chaînes dipolaires. Le premier volet de cette thèse s'articule en trois chapitres et a pour objet de décrire de manière détaillée les interactions entre des chaînes dipolaires. Le second volet, également scindé en trois chapitres, traite des questions de cristallisation qui sont primordiales pour l'élaboration de nouveaux matériaux.

Chapitre 2 : Préambule - modèle général

En guise de préambule à la présentation de nos travaux de recherches, nous revoyons les notions théoriques essentielles de l'interaction dipolaire classique. Nous en profitons pour rappeler l'équivalence entre (i) l'interaction de deux dipôles ponctuelles et celle (ii) de deux sphères magnétiques (uniformément magnétisées). Cette thèse s'intéressant à des assemblées de N sphères magnétiques, nous avons préconisé deux méthodes d'optimisation : (i) *Sequential Least SQuare Programming* (SLSQP) et (ii) *Constrained Optimization BY Linear Approximations* (COBYLA).

Chapitre 3 : Interaction de filaments dipolaires

Ce manuscrit débute avec une analyse théorique de l'interaction de filaments dipolaires tels que des aiguilles ou des chaînes aimantées dans un fort champ magnétique extérieur. L'interaction de deux aiguilles uniformément magnétisées de taille finie L et séparées d'une distance R est revisitée. Tous les régimes pertinents d'attraction et répulsion sont étudiés et discutés en détail. Pour deux aiguilles en vis-à-vis à faible séparation inter-aiguilles ($R/L \lesssim 0.2$), le potentiel de paire répulsif est gouverné par une loi de puissance en R^{-1}, contrastant avec la loi de puissance en R^{-3} trouvée à forte séparation ($R/L \gtrsim 2.5$). Ainsi, un adoucissement du potentiel de paire émerge à très courte séparation aiguille-aiguille. L'origine de cet adoucissement est un écrantage à longue portée induit par des paires attractives distantes compensant la répulsion provenant des paires proches. Toute cette compréhension acquise en revisitant l'interaction effective entre des aiguilles dipolaires a été ensuite exploitée pour rationaliser l'interaction effective des chaînes constituées de sphères magnétiques. Lorsque les corrélations de volume exclu sont faibles, c'est-à-dire au-delà d'une séparation équivalente à la taile de quelques billes, les chaînes en vis-à-vis possèdent pratiquement la même interaction effective que celle entre deux aiguilles. En effet, en contraste avec le comportement des aiguilles, les chaînes dipolaires montrent un durcissement typique à très courte séparation (au voisinage du contact). Cette spécificité est due à la nature discrète des chaînes qui rend l'écrantage de la répulsion moins efficace.

Chapitre 4 : Agrégation de chaînes dipolaires

Ce chapitre aborde le problème de l'agrégation colonnaire de chaînes dipolaires. Dans cette étude, nous prédisons les microstructures des états fondamentaux en fonction du nombre de chaînes N constituant un bouquet. Les chaînes infiniment longues sont d'abord analysées pour des raisons d'universalité. Pour un très faible nombre de chaînes en interaction ($N \leq 3$), les rubans sont les microstructures les plus stables. Au-delà ($N \geq 4$), des bouquets de chaînes arrangées selon un motif en forme de fermeture Éclair à section compacte apparaissent. Pour toutes les microstructures prédites par nos calculs de minimisation, le réseau sous-jacent est un réseau tétragonal centré correspondant également à l'état fondamental du massif. L'énergie du cristal massif est approchée selon une loi de puissance en $N^{-1/2}$. Une remarquable stabilité est obtenue lorsque la section du bouquet de chaînes correspond à un carré ou à un rectangle dont le rapport d'aspect est proche de ce dernier (c'est-à-dire l'unité). Le cas des chaînes de taille finie composées de n billes est aussi discuté. On montre notamment que quelques centaines de billes par chaîne sont nécessaires pour retrouver quantitativement le comportement obtenu dans le cas infini ($n = \infty$). Par ailleurs, l'écart relatif en énergie par rapport au cas infini suit une simple loi de puissance en n^{-1}.

Chapitre 5 - Chaînes dipolaires : De la structure rectiligne à la structure hélicoïdale

Le cas complexe des chaînes hélicoïdales dipolaires est traité ici en considérant au préalable des cas limites plus simples tels que les chaînes linéaires ou en zigzag. Adopter cette approche s'est révélé être très utile pour mieux comprendre les caractéristiques physiques robustes et pertinentes qui s'appliquent aux édifices hélicoïdaux. A partir de l'analyse de l'interaction de deux chaînes linéaires et en zigzag (en fonction de la distance de séparation), une description précise et claire des mécanismes de transition ferromagnétique/antiferromagnétique (c'est-à-dire des chaînes possédant des moments dipolaires égaux ou opposés) est établie. Un comportement similaire est noté entre : (i) le profil d'énergie de la chaîne en zigzag seul (en fonction de sa compaction) et (ii) le profil d'énergie de l'interaction entre deux chaînes en zigzag en fonction de leur séparation mutuelle (à compaction fixée). Par ailleurs, les chaînes en zigzag ne peuvent battre énergétiquement les chaînes

linéaires que lorsque ces premières sont très compressées. Concernant les chaînes hélicoïdales, les microstructures d'énergie minimale sont calculées en fonction de plusieurs paramètres importants tels que le pas, le rayon, et la distance de séparation. Selon le rayon de l'hélice, l'état fondamental est concentrique (pour un rayon suffisamment grand comparé à la taille d'une bille) ou non concentrique avec aucun enchevêtrement des chaînes hélicoïdales (pour un rayon suffisamment petit). À rayon fixé, le profil d'énergie en fonction du pas pour une hélice isolée est similaire au profil d'énergie obtenu pour une double hélice parfaitement concentrique. De plus, quand le pas n'est pas trop petit, la distribution des moments dipolaires obtenue pour deux hélices en interaction est essentiellement dictée par la distribution régnant dans une hélice isolée.

Chapitre 6 : Sédimentation de particules dipolaires dans une monocouche

Le traitement des problèmes de cristallisation débute par l'exploration du confinement bidimensionnel. On s'y intéresse en particulier à travers l'étude de la sédimentation d'une monocouche inclinée et constituée de colloïdes superparamagnétiques où la répulsion interparticulaire est ajustable via un champ magnétique externe appliqué. Expérience, théorie et simulations sont combinées afin d'examiner la structure à l'équilibre de la monocouche. Un modèle simple issu de la théorie de la fonctionnelle de la densité, basé sur une approximation de la densité locale à température nulle, est développé. Notre modèle analytique capture avec succès l'ordre inhomogène variant de l'état solide à l'état liquide observé expérimentalement. Les simulations Monte Carlo corroborent ces résultats et permettent d'explorer une gamme encore plus large de conditions de sédimentation et de couplages magnétiques. En particulier, les simulations indiquent qu'une forte cristallisation se produit près de la paroi inférieure du récipient. Par ailleurs, le paramètre de maille associé au cristal est typiquement dicté par une simple loi de puissance émanant de l'équilibre entre la force de gravité et l'interaction dipôle-dipôle.

Chapitre 7 : Particules dipolaires en couche exposées à un champ magnétique externe

La cristallisation bidimensionnelle est maintenant examinée en considérant l'effet d'un champ magnétique appliqué perpendiculairement à une monocouche (ou une bicouche) cristalline constituée d'aimants sphériques ferromagnétiques. Les calculs de minimisation qui concernent la monocouche montrent que le réseau cristallin dans l'état fondamental est toujours rhombique. À champ magnétique nul, l'état fondamental correspond à un cristal hexagonal (cas particulier de la structure rhombique) s'accompagnant d'une dégénérescence continue de l'orientation du moment dipolaire. À champ magnétique fini, l'angle de rhombicité croît de façon monotone avec l'intensité du champ magnétique appliqué. Cette déformation du réseau a aussi pour effet de lever la dégénérescence continue associée au réseau hexagonal. En revanche, le super-réseau formé par la bicouche est invariant par rapport au champ magnétique appliqué et coïncide avec le réseau tétragonal centré. Par ailleurs, les deux couches constitutives adoptent toujours un réseau hexagonal parfait. À l'aide des symmetries particulières prédites par nos minimisations numériques préliminaires, des expressions analytiques exactes des états fondamentaux des deux systèmes, monocouche et bicouche, sont établies avec succès.

Chapitre 8 : Cristaux dipolaires tridimensionnels

Finalement, nous nous sommes intéressés aux problèmes de cristallisation dans le massif composé de sphères aimantées en établissant un diagramme de phase de l'état fondamental en fonction de la densité. Une nouvelle phase appelée prisme clinohexagonal, rendant compte de tous les états fondamentaux à n'importe quelle densité, est découverte. Cette nouvelle phase consiste simplement en un réseau prismatique oblique à base hexagonale. Plus spécifiquement, nos calculs ont montré qu'aux densités intermédiaires, la phase prisme clinohexagonal coïncide avec la phase orthorhombique centrée. L'analyse des paramètres d'ordre géométriques montre principalement que l'obliquité de la cellule unitaire de la phase prisme clinohexagonal croît avec la densité. Dans le régime des (très) hautes densités (c'est-à-dire au voisinage de la densité de la phase hexagonale compacte), un cas limite de la phase prisme clinohexagonal sans obliquité émerge. Ces résultats fournissent une vision unifiée et clarifiée des transitions solide-solide se produisant à température

nulle dans les systèmes dipolaires.

Chapitre 9 : Conclusion et perspectives

Les résultats présentés dans cette thèse aide à comprendre plus profondément les mécanismes physiques impliqués dans l'auto-assemblage de particules dipolaires. Par ailleurs, ces résultats rationalisent les observations expérimentales récentes. Enfin, nos résultats pourraient constituer une base robuste et s'avérer très utile pour la réalisation et la compréhension de futurs travaux de recherches visant par exemple :

- l'effet du confinement (par exemple par le biais d'un cylindre) et/ou l'effet de la gravité sur l'auto-assemblage des sphères dures dipolaires ;
- la réalisation d'expériences et/ou de simulations numériques sur la cristallisation en monocouche ou bicouche (composée d'aimants permanents) sous champ extérieur perpendiculaire ;
- l'effet de la température sur la cristallisation (par exemple sur la coexistence entre la phase tétragonale centrée et la phase clinohexagonale prisme) ;
- l'établissement du diagramme de phase d'un gaz de particules dipolaires unidimensionnelle à température finie ;
- le comportement de phase de mélanges à plusieurs composants.

List of publications

The research work contained in this thesis has been published in the following scientific journals:

1. R. Messina, L. Spiteri, On the interaction of dipolar filaments. *European Physical Journal E.* 39 (2016).

2. L. Spiteri, R. Messina, Dipolar Crystals: The Crucial Role of the Clinohexagonal Prism Phase. *Physical Review Letters.* 119 (2017).

3. L. Spiteri, R. Messina, Columnar aggregation of dipolar chains. *Europhysics Letters.* 120 (2017).

4. L. Spiteri, R. Messina, D. Gonzalez-Rodriguez, L. Bécu, Ordering of sedimenting paramagnetic colloids in a monolayer. *Physical Review E.* 98 (2018).

5. L. Spiteri, R. Messina, I. Stanković, Interaction of dipolar helical chains including linear- and zigzag-chains. (submitted to *The Journal of Chemical Physics*)

Contents

1 Introduction **1**

2 Preamble: General model **5**

2.1 Dipole moments 5

2.1.1 Magnetic field 6

2.1.2 Dipolar interaction 7

2.2 Magnetic spheres 8

2.2.1 Isolated magnetic sphere 8

2.2.2 Interaction of two magnetic spheres 9

2.3 Energy minimization 12

2.3.1 Method without derivatives 12

2.3.2 Method with derivatives 12

2.3.3 Strategy to reach the global minimum 13

I Dipolar chains in interaction **15**

3 Interaction of dipolar filaments **17**

3.1 Introduction 17

3.2 Model 18

3.2.1 Two-chain interaction 18

3.2.2 Two-needle interaction 20

3.3 Magnetic needles 21

3.3.1 Facing needles 21

3.3.2 Shifted needles 26

3.4 Magnetic chains 30

3.4.1 Facing chains 30

3.4.2 Touching shifted chains 34

3.5 Concluding remarks 35

4 Bundles of dipolar chains **37**

4.1 Introduction 37

4.2 Model 38

4.3 Method . . . 40
4.4 Infinitely long chains . . . 40
4.5 Finite-size chains . . . 43
4.6 Concluding remarks . . . 45

5 Dipolar chains: From linear to helical form 47
5.1 Introduction . . . 48
5.2 Model and computational details . . . 48
5.2.1 Helical chain geometry . . . 48
5.2.2 Dipole-dipole interaction . . . 51
5.2.3 Energy minimization . . . 52
5.3 Dipolar linear chains . . . 52
5.3.1 Single linear chain . . . 52
5.3.2 Interaction of two linear chains . . . 53
5.4 Dipolar zigzag chains . . . 55
5.4.1 Single zigzag chain . . . 55
5.4.2 Interaction of two zigzag chains . . . 58
5.5 Dipolar helical chains . . . 60
5.5.1 Single helical chain . . . 60
5.5.2 Interaction of two helical chains . . . 62
5.6 Concluding remarks . . . 67

II Crystallization of dipolar particles 69

6 Sedimentation of dipolar particles in a monolayer 71
6.1 Introduction . . . 71
6.2 Experimental system . . . 72
6.3 Theoretical model . . . 74
6.4 Monte Carlo simulations . . . 77
6.5 Density profiles . . . 78
6.6 Concluding remarks . . . 81

7 Layered dipolar particles in external magnetic field 83
7.1 Introduction . . . 83
7.2 Model . . . 84
7.3 Method . . . 85

7.4 Monolayer in external field . . . 86
7.5 Bilayer in external field . . . 89
7.6 Concluding remarks . . . 91

8 Three-dimensional dipolar crystals 93
8.1 Introduction . . . 93
8.2 Model . . . 94
8.3 Method . . . 95
8.4 Dipolar crystal phases . . . 97
8.5 Geometric order parameters . . . 100
8.6 Concluding remarks . . . 104

9 Conclusion and perspectives 107

A SLSQP algorithm 111
A.1 Nonlinear programming problem . . . 111
A.2 Line search strategy . . . 112
A.3 Quadratic programming problem . . . 112
A.4 The search direction . . . 113
A.5 The step length . . . 113
A.6 The Hessian matrix . . . 114

B Layered dipolar particles in external magnetic field: Analytical expressions 115
B.1 Monolayer in external field . . . 115
B.1.1 General expressions for the ground state . . . 116
B.1.2 Hexagonal lattice approximation (HLA) . . . 118
B.1.3 Solid/Gas transition . . . 118
B.2 Bilayer in external field . . . 119
B.2.1 General expressions for the ground state . . . 121
B.2.2 Solid/Gas transition . . . 122

Bibliography 123

Chapter 1

Introduction

Self-assembly is a process in which disordered components spontaneously and autonomously organize into ordered structures or patterns due to interactions among the pre-existing components themselves, see Fig. 1.1. This phenomenon is ubiquitous in nature, besides life on Earth is an outstanding example of functional self-assembly [2, 3, 4]. Indeed, the functionality of the cell, which is the fundamental unit to all the living beings, is ensured through many self-assembling processes (e.g. the assembly of the DNA double helix or the formation of lipid bilayer membranes). Examples of self-assembly can be also mentioned in physics and chemistry [2] such as the planetary systems, the weather systems (as ordered patterns), the phase-separated polymers, the formation of peptide amphiphile nanofibers as well as the molecular, liquid and colloidal crystals. The tailoring of the self-assembly process can be achieved by different means: biomolecules (via their bonding properties), template (via pattern or confinement) and external field (electric, magnetic, laser or gravity fields). Among this variety of strategies, magnetic-field-guided (or equivalently electric-field-guided) self-assembly allows an important freedom to design controlled structures [5].

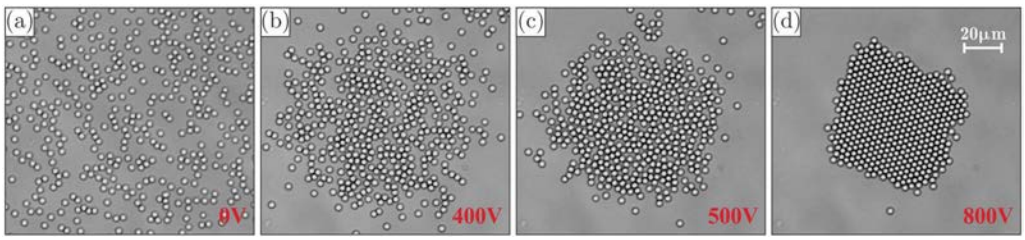

Figure 1.1: An illustrative example of self-assembly process occurring in an experiment with colloidal particles in external rotating electric fields: Panels (a)-(d) depict about 450 silica particles of 2.12 μm diameter, undergoing a transition from a (dilute) fluid state to a crystalline state upon a gradual increase of the field ($U = 0, 0.4, 0.5, 0.8$ kV, respectively). Image reproduced from [1]. In the shown example the horizontally field rotated with the frequency of $\nu = 30$ kHz.

This thesis deals with self-assembled dipolar particles. Our theoretical approach will be based on the dipolar hard sphere (DHS) model which consists of hard spheres with embedded point-like dipole at their centers. From a conceptual aspect, the DHS model is the simplest one incorporating anisotropic long-range interaction which allows to explore in a more universal fashion the structure and phase behavior. Consequently, it is an ideal model system often used as reference for the understanding of more complicated systems in condensed matter [5]. The dipolar hard spheres can be found at a wide range of length scale, for instance magnetic balls [6], granulates [7], dust particles [8], colloidal particles [9], or other nanoparticles [10]. Such components play a key role in condensed matter physics, especially for the following fields: crystallization [11, 12], crystal growth [13], dipolar colloidal suspensions (ferrofluids [14, 15], magnetorheological fuilds [16, 17]) or complex (dusty) plasmas [18]. Note also that some living organisms synthesize dipolar nanoparticles [19], thus the interest of the DHS model may expand to the biology.

The dipolar hard spheres provide a great practical interest too. The self-assembly of dipolar hard spheres as bottom-up method offers a new route for the fabrication of functional materials [2]. Some devices currently exploited are already based on the dipolar hard spheres, for instance magnetorheological dampers (vehicle's suspensions, human prosthesis), magnetorheological finishing (polishing method), cooling system (loudspeakers), liquid seals (hard disks) or centrifugation (disease detection method). Many others devices are in development such as photonic crystals [20], impact absorbers [21, 22, 23] to decrease the shock caused by a crash, a gun shot or a earthquake, spacecraft thrusters [24], decontamination systems [25], micropumps [26], medical treatments [27, 28, 29, 30], magnetic morphing mirrors [31] and self-healing electric circuits [32].

On the theoretical side, Jacobs and Beans in 1955 [33] have broken new ground by using a "chain-of-spheres" model to predict experimental observations on magnetic behavior of elongated iron particles. Later, this interest for spherical magnets was further amplified by the investigations of de Gennes and Pincus in 1970 [34] demonstrating the formation of chains of spherical ferromagnetic grains along the applied external magnetic field in a dilute magnetic fluid. On the other hand, Luttinger and Tisza proposed in 1946 a method to calculate the dipolar crystal ground states and successfully applied it in cubic systems [35]. It is only in the early 1990s that the theoretical studies on infinitely long chains in strong external magnetic field [36, 37] have inspired Tao *et al.* [38] to discover that the overall

ground state in dipolar crystals is the body-centered tetragonal structure. Dipolar particles are still a highly active field of research. Recent investigations have shown that magnetic spheres in athermal systems form a broad diversity of structures (e.g., chains, rings, tubes) that depend on parameters such as the number of beads [39, 40, 41, 42, 43, 44, 45, 46, 47], the external field [45, 47], the confinement [43, 44], the mechanical forces [39, 46], etc. This rich phase behavior encourages further exploration and understanding.

The overall goal of this thesis is to further understand the effects of intimate physical mechanisms involved in the self-assembly of dipolar particles based on a physically, simple and transparent approach. It is now well-known that dipolar systems exhibit a strong tendency even without magnetic/electric field to form chains [48]. Many structures made up of dipolar spheres can be built from dipolar chains as basic building blocks, for instance the body-centered tetragonal and the hexagonal structures. The dipolar chains are clearly of prime interest to understand the process of assembly of magnetic spheres into crystal structures. We decompose this manuscript into two main parts. The first part deals with dipolar chains in interaction and the second one involves the crystallization of dipolar particles. Beforehand, as a preamble, we introduce in Chapter 2 the general model.

The main first part of the thesis gather three published studies about interacting dipolar chains, each appearing as separate chapter. We start our manuscript with an investigation on the interaction of dipolar filaments. The aim here is to revist the physics of two interacting dipolar needles. Doing so deeper understanding is gained and exploited to grasp the behavior of interacting dipolar chains, see Chapter 3. Then in Chapter 4, focus is put on the columnar aggregation mainly dictated by the number of constitutive dipolar chains. The dipolar chains, whether linear or zigzag-like, also turn out to capture the interaction of more generic dipolar helical chains, see Chapter 5.

In the second part devoted to the crystallization, we present three detailed studies as well. The two-dimensional confinement is explored in Chapter 6 through the sedimentation of (repulsive) dipolar colloids in a tilted monolayer subject to a perpendicular magnetic field. Then, Chapter 7 deals with (attractive) ferromagnetic layered dipolar particles under a perpendicular magnetic field. So far, what we have learned to the (bulk) body-centered tetragonal ground state structure can be obtained from chain or layer aggregation. Thereby, the last Chapter 8 covers the bulk crystal phase behavior of dipolar hard spheres prepared at any density.

Chapter 2

Preamble: General model

Contents

2.1 Dipole moments 5

2.1.1 Magnetic field 6

2.1.2 Dipolar interaction 7

2.2 Magnetic spheres 8

2.2.1 Isolated magnetic sphere 8

2.2.2 Interaction of two magnetic spheres 9

2.3 Energy minimization 12

2.3.1 Method without derivatives 12

2.3.2 Method with derivatives 12

2.3.3 Strategy to reach the global minimum 13

2.1 Dipole moments

The Oersted's experiment in 1820 has shown that a compass needle is deviated in the vicinity of a current flowing through a conducting wire. Thereby, Oersted has also revealed the strong link between the electric current and the magnetic field. The Biot-Savart law [49] determining the equation of the magnetic field generated by a electric current is established by Biot and Savart shortly after the Oersted's observations. These significant developments are considered as the starting point of the magnetism. The strong relation between electric current and magnetism involves at the microscopic scale, the motion of electrons (e.g. around the atomic nuclei or their own axes) is the source of the magnetic field. The magnetic dipole can be identified through the torque exerted in presence of magnetic field. Typically, representation of dipole moments are illustrated in Fig. 2.1.

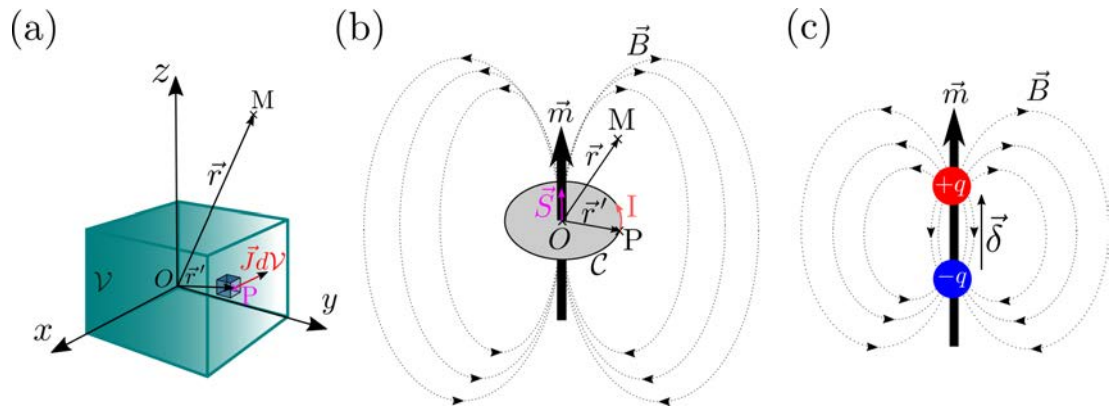

Figure 2.1: Schematic representation of the magnetic dipole according to: (a) the model of the current distribution $\vec{J}(\vec{r}\,')$ in a volume $\mathcal{V}$, $\vec{m} = \frac{1}{2}\iiint_{\mathcal{V}} \vec{r}\,' \wedge \vec{J}(\vec{r}\,')d\mathcal{V}$; (b) the model of the closed loop $\mathcal{C}$ carrying a current I, $\vec{m} = I\vec{S}$; (c) the model of the pair of fictitious magnetic charges $(+q,-q)$, $\vec{m} = q\vec{\delta}$. The dashed lines depict the magnetic field lines and the associated arrows indicate the direction of the magnetic field $\vec{B}$.

2.1.1 Magnetic field

The expression of the magnetic field $\vec{B}(\vec{r})$ generated by a point-like dipole $\vec{m}$ at the position $\vec{r}$ [50, 51, 52]:

$$\vec{B}(\vec{r}) = \frac{\mu_0}{4\pi}\frac{1}{r^3}\left[3\frac{(\vec{m}\cdot\vec{r})\vec{r}}{r^2} - \vec{m}\right], \tag{2.1}$$

where $r = \|\vec{r}\|$ and $\mu_0 = 4\pi \times 10^{-7}$ (in SI units) is the vacuum permeability. When we are dealing with N magnetic dipoles $(\vec{m}_1, ..., \vec{m}_N)$, the total magnetic field $\vec{B}(\vec{r})$ at the distance $\vec{r}$ follows the superposition principle [50, 51]:

$$\vec{B}(\vec{r}) = \sum_{i=1}^{N} \frac{\mu_0}{4\pi}\frac{1}{\| \vec{r} - \vec{r}_i \|^3}\left[3\frac{(\vec{m}_i\cdot(\vec{r}-\vec{r}_i))(\vec{r}-\vec{r}_i)}{\| \vec{r} - \vec{r}_i \|^2} - \vec{m}_i\right], \tag{2.2}$$

where $\vec{r}_i$ designates the positions of the dipole $\vec{m}_i$ $(i = 1, ..., N)$. If not differently specified in the manuscript, N will refer to as a number of particles.

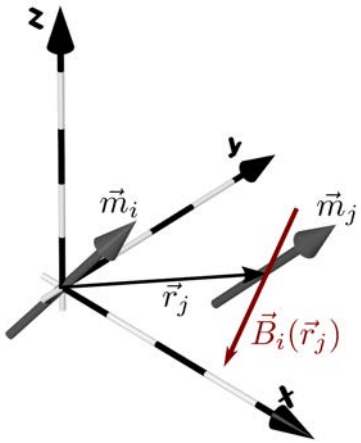

Figure 2.2: Scheme of two interacting magnetic dipoles $\vec{m}_i$ and $\vec{m}_j$.

2.1.2 Dipolar interaction

The interaction energy between two magnetic dipoles $\vec{m}_i$ and $\vec{m}_j$ located at $\vec{r}_i$ and $\vec{r}_j$, respectively, is obtained through the so-called Zeeman interaction term [50]

$$U(\vec{r}_{ij}) = -\vec{m}_j \cdot \vec{B}_i(\vec{r}_j), \tag{2.3}$$

$\vec{B}_i(\vec{r}_j)$ being the magnetic field produced at $\vec{r}_j$ by the dipole $\vec{m}_i$, see Fig. 2.2. By using Eq. (2.1), it involves the following expression of the dipole-dipole interaction

$$U(\vec{r}_{ij}) = \frac{\mu_0}{4\pi}\frac{1}{r_{ij}^3}\left[\vec{m}_i \cdot \vec{m}_j - 3\frac{(\vec{m}_i \cdot \vec{r}_{ij})(\vec{m}_j \cdot \vec{r}_{ij})}{r_{ij}^2}\right], \tag{2.4}$$

where $\vec{r}_{ij} = \vec{r}_j - \vec{r}_i$ and $r_{ij} = \|\vec{r}_{ij}\|$. In the case of N interacting dipoles the summation of all the pair interactions gives the total interaction energy

$$U = \frac{1}{2}\sum_{i,j}^{N}\frac{\mu_0}{4\pi}\frac{1}{r_{ij}^3}\left[\vec{m}_i \cdot \vec{m}_j - 3\frac{(\vec{m}_i \cdot \vec{r}_{ij})(\vec{m}_j \cdot \vec{r}_{ij})}{r_{ij}^2}\right]. \tag{2.5}$$

The non-uniformity of the magnetic field $\vec{B}(\vec{r})$ in the space involves a non-zero gradient. For that reason, a magnetic dipole $\vec{m}_i$ exerts a force $\vec{F}_{ij}$ on a dipole $\vec{m}_j$

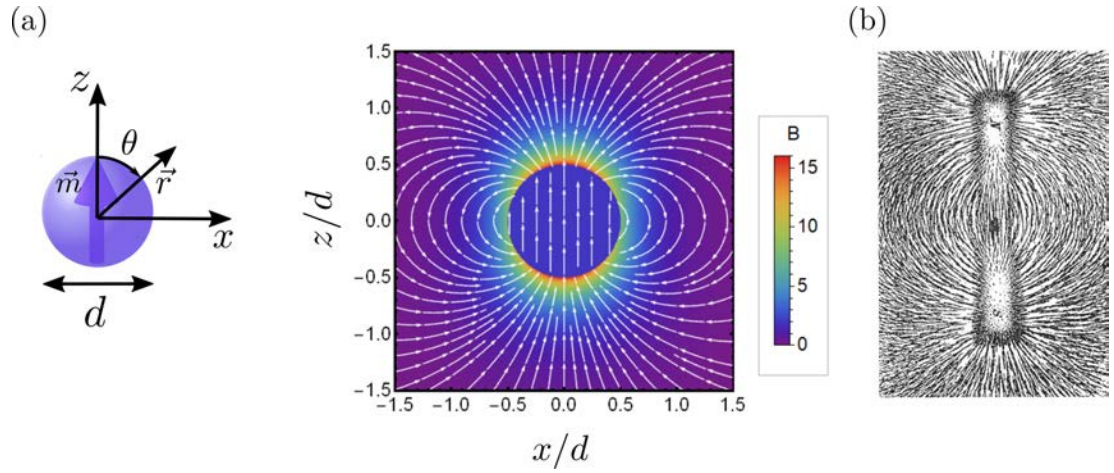

Figure 2.3: (a) A two-dimensional view of the landscape of the magnetic field intensity B originating from an isolated magnetic sphere placed at the origin. The white lines depict the magnetic field lines and the arrows give the direction of $\vec{B}$. (b) Magnetic field lines made visible by iron filings sprinkled on a paper placed above a bar magnet [53].

according to the expression $\vec{F}_{ij} = -\overrightarrow{\text{grad}}\, U(\vec{r}_{ij})$. From Eq. (2.4), it follows

$$\vec{F}_{ij} = \frac{3\mu_0}{4\pi r_{ij}^5}\left[(\vec{m}_i\cdot\vec{r}_{ij})\vec{m}_j + (\vec{m}_j\cdot\vec{r}_{ij})\vec{m}_i + (\vec{m}_i\cdot\vec{m}_j)\vec{r}_{ij} - 5\frac{(\vec{m}_i\cdot\vec{r}_{ij})(\vec{m}_j\cdot\vec{r}_{ij})\vec{r}_{ij}}{r_{ij}^2}\right]. \quad (2.6)$$

This expression is easily generalized to obtain the force $\vec{F}_i$ sustained by a dipole $\vec{m}_i$ in the presence of an assembly of $N-1$ dipoles

$$\vec{F}_i = \sum_{\substack{j=1\\ i\neq j}}^{N} \vec{F}_{ij}. \quad (2.7)$$

2.2 Magnetic spheres

2.2.1 Isolated magnetic sphere

We now consider a magnetic sphere uniformly magnetized with a diameter $d = 1$ and a (integrated) magnetic moment $\vec{m} = m\vec{e}_z = \vec{e}_z$, see Fig. 2.3(a). It is convenient to assume $y = 0$ because of the azimuthal symmetry (i.e., the field pattern is rotation

invariant around the z-axis) and also to introduce the polar angle θ with the vector position $\vec{r} = r(\sin\theta, \cos\theta)$, see Fig. 2.3(a). So far, we have only mentioned the magnetic field $\vec{B}(\vec{r})$ for a *point-like* dipole, see Eq. (2.1). However, the magnetic system we are looking at is made up of uniformly magnetized beads, see Fig. 2.3(a). In fact, it turns out that a uniformly magnetized sphere generates (outside the sphere) the same magnetic field as that produced by a point-like dipole (of identical strength) located at its center [50]. The landscape of the magnetic field intensity (with $\frac{\mu_0}{4\pi} = 1$) in the (x, z)-plane, see Fig. 2.4(a), is calculated from

$$B = \begin{cases} 2, & r < \dfrac{1}{2}, \\ \dfrac{\sqrt{4\cos^2\theta + \sin^2\theta}}{r^3}, & r \geq \dfrac{1}{2}, \end{cases} \tag{2.8}$$

where $r = \sqrt{x^2 + z^2}$ and $B = \sqrt{B_x^2 + B_z^2}$ with B_x and B_z stemming from Eq. (2.1). Concerning the magnetic field lines [54], see Fig. 2.4(a), we have

$$r(\theta) = K \sin^2\theta, \tag{2.9}$$

where K denotes the distance at which the field lines crosses the equator (i.e., the x-axis in Fig. 2.3(a)).

2.2.2 Interaction of two magnetic spheres

To gain a sound understanding of the pair dipolar interaction, it is necessary to begin by considering two parallel dipole moments $\vec{m}_1$ and $\vec{m}_2$ located at $\vec{r}_1 = (x_1, z_1)$ and $\vec{r}_2 = (x_2, z_2)$, see Fig. 2.4(a). Such a situation is realized for instance in the presence of a strong homogeneous external magnetic field. More specifically, let us consider two identical dipoles immersed in a strong magnetic field $\vec{B} = B\vec{e}_z$, with $\vec{e}_z$ being a unit vector along the $z-$axis, so that $\vec{m}_1 = \vec{m}_2 = \vec{m} = m\vec{e}_z$. In the same spirit of the equivalence between the magnetic field produced by a sphere and point-like dipole discussed in Section 2.2.1, it can be also shown [55] that two uniformly polarized/magnetized spheres interact identically to two point-like dipoles concentrated in each respective sphere's center. It is convenient to introduce the energy scale as

$$U_{\uparrow\uparrow} \equiv \frac{Cm^2}{d^3}. \tag{2.10}$$

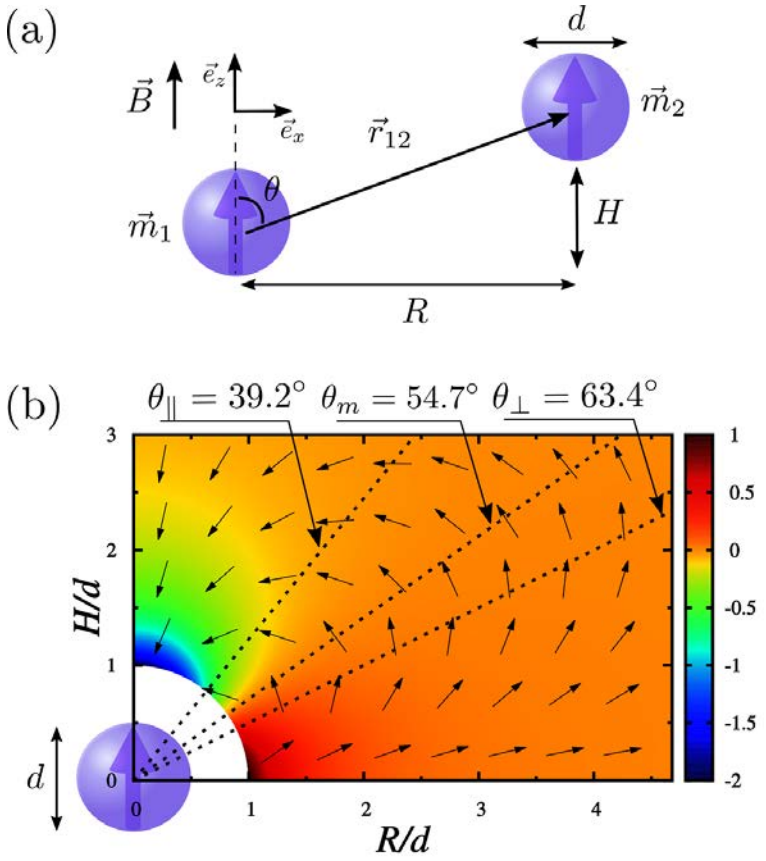

Figure 2.4: (a) Geometry setup for two interacting dipolar beads $\vec{m}_1$ and $\vec{m}_2$ with relative spatial separation $\vec{r}_{12}$. Notice that R corresponds to the distance between the dipole moments axis. (b) Energy landscape of $\tilde{U}(\tilde{R}, \tilde{H})$, see equation (2.11) and text, for two interacting dipoles with one placed at the origin. The white area around the origin corresponds to a depletion zone. The arrows indicate the direction of the magnetic force. The magic angle θ_m together with the zero (transverse and longitudinal) force angles ($\theta_{\perp}$ and $\theta_{\parallel}$, respectively) are also indicated.

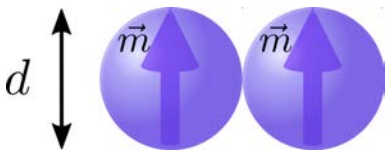

Figure 2.5: Two parallel dipoles at contact standing side by side.

Physically, it represents the repulsive potential value for two hard spheres of diameter d at contact carrying parallel dipoles that stand side by side, see Fig. 2.5. This definition involves that the magnetic field strength and the force will be given in units of $\frac{U_{\uparrow\uparrow}}{m}$ and $\frac{U_{\uparrow\uparrow}}{d}$, respectively. In general C will depend on the intervening medium as well as the nature of the dipoles (magnetic vs electric). Thereby, by using Eq. (2.4), the reduced potential energy of interaction $\tilde{U}$ for two such magnets reads

$$\tilde{U}(\vec{r}_{12}/d) = \frac{U(\vec{r}_{12})}{U_{\uparrow\uparrow}} = \frac{1}{\tilde{r}_{12}^3}\left[1 - 3\cos^2\theta\right], \tag{2.11}$$

where $\tilde{r}_{12} = \frac{r_{12}}{d} = \sqrt{\tilde{R}^2 + \tilde{H}^2}$ and $\cos^2\theta = \frac{\tilde{H}^2}{\tilde{R}^2+\tilde{H}^2}$ with $\tilde{R} = R/d$ and $\tilde{H} = H/d$, see also Fig. 2.4(a). A landscape of the potential energy of interaction as a function of $\tilde{R}$ and $\tilde{H}$ is provided in Fig. 2.4(b). The special angle θ_m for which $\tilde{U}(\theta_m = \text{acos}(1/\sqrt{3}) \simeq 54.7°) = 0$ is called the *magic angle*, see also Fig. 2.4(b).

The force normal to $\vec{B}$, denoted $\vec{F}_\perp$, is merely given by $\vec{F}_\perp = -\overrightarrow{\text{grad}}_R\, U$. In reduced units, one obtains:

$$\tilde{F}_\perp = \frac{F_\perp}{\frac{U_{\uparrow\uparrow}}{m}} = \frac{3\sin\theta}{\tilde{r}_{12}^4}\left[1 - 5\cos^2\theta\right]. \tag{2.12}$$

The special angle $\theta_\perp$ for which $\tilde{F}_\perp = 0$ is then given by $\theta_\perp = \text{acos}(1/\sqrt{5}) \simeq 63.4° > \theta_m$. In other words, when approaching (say from infinite separation) the dipoles at prescribed shift $\tilde{H}$, one switches from repulsion to attraction at $\theta_\perp$, see also Fig. 2.4(b). In standard textbooks, see e.g. Ref. [56], the magic angle always refers to the zero energy point. Notice that the *radial* component of the force (i.e., $\tilde{F}_{\text{rad.}} = \frac{3(1-3\cos^2\theta)}{\tilde{r}_{12}^4}$) has the same angular dependency [57]. However, to have a complete picture of the dipolar interaction, it is natural to introduce the notion of zero (longitudinal/transverse) force angle as done here.

Similarly, the longitudinal force parallel to $\vec{B}$, $\vec{F}_\parallel$, is merely given by $\vec{F}_\parallel = -\overrightarrow{\text{grad}}_H\, U$. By analogy with Eq. 2.12, one can write:

$$\tilde{F}_\parallel = \frac{F_\parallel}{\frac{U_{\uparrow\uparrow}}{m}} = \frac{3\cos\theta}{\tilde{r}_{12}^4}\left[3 - 5\cos^2\theta\right] \tag{2.13}$$

showing that the special angle $\theta_\parallel$ for which $\tilde{F}_\parallel = 0$ is then given by $\theta_\parallel = \text{acos}(\sqrt{3/5}) \simeq 39.2°$ so that $\theta_\parallel < \theta_m < \theta_\perp$, see also Fig. 2.4(b).

2.3 Energy minimization

2.3.1 Method without derivatives

A substantial part of our investigations is concerned by constrained optimization problems stemming from the search for ground state energies of the dipolar systems while fully respecting the tedious nonoverlapping condition between the hard spheres. To solve such optimization problems, two deterministic algorithms had to be used. One called Constrained Optimisation BY Linear Approximations (COBYLA) is a gradient-free algorithm created by Powell [58] which primarly employs linear approximations of the objective and constraint functions. These linear approximations are obtained by linear polynomial interpolation at $n + 1$ points (vertices) in the space of the n variables arranged as a simplex. The optimization procedure follows the idea of Nelder and Mead [59] to drive the shrinkage of the simplex. The goodness of different vertices during the different stages of the COBYLA algorithm is measured by a merit function, however the constraints are treated individually during the calculation of the new solution. Throughout the procedure, a regular shape of the simplex is maintained by means of a trust region radius (progressively adjusted) during the optimization.

2.3.2 Method with derivatives

The second algorithm called Sequential Least SQuare Programming (SLSQP) is a gradient-based algorithm, published by Kraft [60], belonging to the sequential quadratic programming (SQP) class of methods for optimization problems, see also Appendix A. Basically, the SQP methods rely on the so-called line search strategy. Starting from an initial guess, iterative updated of the objective function are computed using each time an optimal search direction. The search direction is determined by employing a quadratic approximation of the objective function with a linear approximation of the constraints to transform the nonlinear problem into a linear least square (LSQ) subproblem. Then, the LSQ suproblem is solved via an adapted Lawson and Hanson's method (NNLS algorithm) [61]. On the other hand, the Hessian matrix (stemming from the quadratic approximation) is updated by Broyden, Fletcher, Goldfarb and Shanno (BFGS) approximation and the step length of the optimization is adjusted by an appropriate merit function, see also Appendix A.

2.3.3 Strategy to reach the global minimum

Both COBYLA and SLSQP algoritms are local optimizers and provide local minima, whereas our objective is to find ground states, that is, global minima. To achieve this aim, the optimization algorithms had to be runned separately with different starting points. Each run providing a solution corresponding to a local minimum, the best of all these local minima obtained should be the global minimum of the objective function in the search space considered. Note that all our minimizations throughout this manuscript have been realized by means of the open-source library for NonLinear optimization (NLopt library) [62].

Part I

Dipolar chains in interaction

Chapter 3

Interaction of dipolar filaments

The present chapter addresses the interaction of two magnetic filaments, such as magnetic chains or needles, and whose results were published in *European Physical Journal E* [63].

Contents

3.1 Introduction 17

3.2 Model 18

3.2.1 Two-chain interaction 18

3.2.2 Two-needle interaction 20

3.3 Magnetic needles 21

3.3.1 Facing needles 21

3.3.2 Shifted needles 26

3.4 Magnetic chains 30

3.4.1 Facing chains 30

3.4.2 Touching shifted chains 34

3.5 Concluding remarks 35

3.1 Introduction

Magnetic materials with elongated linear shapes are quite ubiquitous in nature [19] and every day-life. In nature, such objects that are sensitive to the earth's magnetic field can be found for example in magnetotactic bacteria [64, 65], birds [66] or algaes [67]. One dimensional magnetic chain-like structures can be beneficial in biomedicine [68, 69] for drug delivery [70] or hyperthermia treatment [71]. In

nanotechnology, magnetic nanowires have enormous application potential in ultra-high density storage [72].

Recent experiments [5, 57, 73, 74, 75] have been devoted to the analysis of the interaction of one-dimensional magnetic bodies under an external field which is closely related to our problem. Tanase and coworkers [73] looked at the response of nickel nanowires to magnetic fields and were able to monitor the resulting pair-interaction. Kornev and coworkers [57, 75] have pointed out that magnetic *needles* made up of carbon nanotubes filled with magnetic particles are promising candidates for self-assembly into regular superstructures. Darras *et al.* [9] have reported on *ribbon formation* due to lateral aggregation of magnetic chains made up of superparamagnetic colloids.

On the theoretical side, the case of *infinite* chains made up of spherical dipolar beads is well understood [36, 37, 76]. Thereby the pair interaction is characterized by an exponential decay with the inter-chain separation as advocated by Halsey and Toor in the 90s [36, 37]. Much less is known for *finite* sized chains. A combined experimental/theoretical study was undertaken by Furst and Gast [77] who observed the lateral attraction of dipolar chains and the resulting rheological response. Messina and Stankovic [42] recently showed that elongated dipolar rod-like structures made up of parallel chains that exhibit a local tetragonal arrangement [38] are energetically more favorable than round clusters [78]. Based on the method of collective variables, Cebers [79] predicted an orientational ordering of a suspension of magnetic needles in the absence of magnetic field. On the other hand, Belobrov et al. [80, 81, 82] have advocated the relevance of degenerated vortex ground states in (finite and infinite) two- and three-dimensional dipole systems.

3.2 Model

3.2.1 Two-chain interaction

The model of two parallel magnetic chains is sketched in Fig. 3.1(a). Such a configuration is realized for instance in the presence of a strong homogeneous external magnetic field $\vec{B} = B\vec{e}_z$, $\vec{e}_z$ being a unit vector along the $z-$axis, so that all the magnetic moments $\vec{m} = m\vec{e}_z$ are identical. The total reduced potential energy of

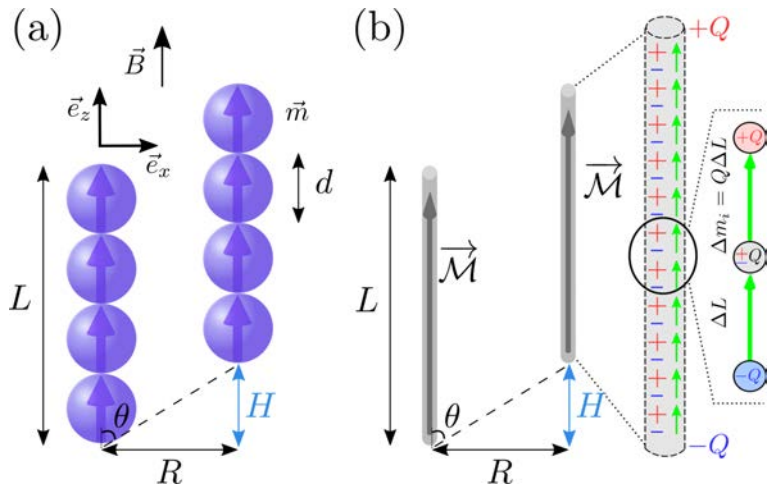

Figure 3.1: (a) Geometry setup for two interacting parallel magnetic chains. In this illustration $N = 4$ so that the chain length $L = 4d$. (b) Geometry setup for two needles of length L with dipole moment $\vec{\mathcal{M}}$. Notice that R always corresponds to the distance between the dipole moments axis. On the far right, a cartoon of (identical) infinitesimal constitutive dumbbell-like dipoles $\Delta\vec{m}_i = Q\Delta L\vec{e}_z$ with $\vec{\mathcal{M}} = \sum_i \Delta\vec{m}_i = QL\vec{e}_z$ is sketched. The mechanism of charge cancellation within the needle is illustrated too, see also text around Eq. (3.8).

two chains made up of N beads each is given by

$$\tilde{U}_N^{\rm tot} = \frac{U_N^{\rm tot}}{U_{\uparrow\uparrow}} = \frac{1}{2}\sum_{i=1}^{2N}\sum_{\substack{j=1\\ i\neq j}}^{2N}\frac{U(\vec{r}_{ij})}{U_{\uparrow\uparrow}} \quad (r_{ij}\geq d), \tag{3.1}$$

where $U_{\uparrow\uparrow}$ is the energy scale, see Eq. (2.10). The sum in Eq. (3.1) can be separated into two terms,

$$\tilde{U}_N^{\rm tot} = 2\tilde{U}_N^{\rm intra} + \tilde{U}_N^{\rm cc}, \tag{3.2}$$

where $\tilde{U}_N^{\rm intra}$ is the *intra-chain* contribution to the total energy, whereas $\tilde{U}_N^{\rm cc}$ is the *inter-chain* (or cross chain) contribution to the total energy. More explicitly, the reduced intra-chain energy $\tilde{U}_N^{\rm intra}$ is given by

$$\tilde{U}_N^{\rm intra} = -\sum_{i=1}^{N-1}\sum_{j=i+1}^{N}\frac{2}{(j-i)^3} = -2\sum_{i=1}^{N-1}\frac{N-i}{i^3}. \tag{3.3}$$

This always negative energy in Eq. (3.3) can be seen as the *cohesive* energy of a magnetic chain.

On the other hand, the inter-chain term $\tilde{U}_N^{\rm cc}$ in Eq. (3.2) can be either positive or

negative depending on the relative $\tilde{H}/\tilde{R}$-shift of the two chains. Taking advantage of the symmetry of the system, we arrive at the simple expression for the inter-chain interaction energy

$$\tilde{U}_N^{\mathrm{cc}}(\tilde{H},\tilde{R}) = \sum_{i=-N+1}^{N-1} (N-|i|)\left\{\frac{1}{[(i+\tilde{H})^2+\tilde{R}^2]^{\frac{3}{2}}} - \frac{3(i+\tilde{H})^2}{[(i+\tilde{H})^2+\tilde{R}^2]^{\frac{5}{2}}}\right\}. \tag{3.4}$$

with $\tilde{R} = R/d$ and $\tilde{H} = H/d$, see also Fig. 3.1(a).

The effective reduced force between these two chains in the direction perpendicular to the external magnetic field (or equivalently the chains axis) is then given by

$$\begin{aligned}\tilde{F}_{\perp}^{\mathrm{chain}} &= -\frac{\partial}{\partial\tilde{R}}\tilde{U}_N^{\mathrm{cc}}(\tilde{H},\tilde{R}) \\ &= \sum_{i=-N+1}^{N-1} (N-|i|)\left\{\frac{3\tilde{R}}{[(i+\tilde{H})^2+\tilde{R}^2]^{\frac{5}{2}}} - \frac{15\tilde{R}(i+\tilde{H})^2}{[(i+\tilde{H})^2+\tilde{R}^2]^{\frac{7}{2}}}\right\}.\end{aligned} \tag{3.5}$$

Similarly, the longitudinal effective force along the chains axis (or equivalently the magnetic field direction) is given by

$$\begin{aligned}\tilde{F}_{\parallel}^{\mathrm{chain}} &= -\frac{\partial}{\partial\tilde{H}}\tilde{U}_N^{\mathrm{cc}}(\tilde{H},\tilde{R}) \\ &= \sum_{i=-N+1}^{N-1} (N-|i|)\left\{\frac{9(i+\tilde{H})}{[(i+\tilde{H})^2+\tilde{R}^2]^{\frac{5}{2}}} - \frac{15(i+\tilde{H})^2}{[(i+\tilde{H})^2+\tilde{R}^2]^{\frac{7}{2}}}\right\}.\end{aligned} \tag{3.6}$$

That way, when talking about attraction vs repulsion, it is the sign of these related effective forces that will matter.

3.2.2 Two-needle interaction

Consider two identical uniformly magnetized needles of length L with negligible section, see Fig. 3.1(b). The total dipole moment of one magnetic needle is $\vec{\mathcal{M}} = \lambda L\vec{e}_z$ with λ standing for the linear dipole moment density strength. For two such parallel magnetic needles shifted from a length H in the z-direction we have:

$$\begin{aligned}U_{\mathrm{needles}} = C\lambda^2 \int_0^L dz_1 \int_H^{H+L} dz_2 \left[\frac{1}{[(z_2-z_1)^2+R^2]^{3/2}}\right] \\ - 3C\lambda^2 \int_0^L dz_1 \int_H^{H+L} dz_2 \left[\frac{(z_2-z_1)^2}{[(z_2-z_1)^2+R^2]^{5/2}}\right].\end{aligned} \tag{3.7}$$

The two involved double integrals in Eq. (3.7) can be analytically evaluated and the final result reads:

$$U_{\text{needles}} = \frac{2C\lambda^2}{\sqrt{R^2+H^2}} - \frac{C\lambda^2}{\sqrt{(H+L)^2+R^2}} - \frac{C\lambda^2}{\sqrt{(H-L)^2+R^2}}. \tag{3.8}$$

This result can strikingly also be seen as stemming from two dumbbell-like (electric) dipoles carrying opposite *effective charges* Q and $-Q$ at both ends, see Fig. 3.1(b), where $Q = \lambda$ [1]. This representation is also referred to as *magnetic charges* in the literature, see e.g. [75] [83, pp. 34 ff]. Again here, transverse and longitudinal forces are merely given by

$$\begin{aligned} F_{\perp}^{\text{needle}} &= -\frac{\partial}{\partial R} U_{\text{needles}}(H,R) \\ &= \frac{2CR\lambda^2}{[R^2+H^2]^{3/2}} - \frac{CR\lambda^2}{[(H+L)^2+R^2]^{3/2}} - \frac{CR\lambda^2}{[(H-L)^2+R^2]^{3/2}} \end{aligned} \tag{3.9}$$

and

$$\begin{aligned} F_{\parallel}^{\text{needle}} &= -\frac{\partial}{\partial H} U_{\text{needles}}(H,R) \\ &= \frac{2HC\lambda^2}{[R^2+H^2]^{3/2}} - \frac{(H+L)C\lambda^2}{[(H+L)^2+R^2]^{3/2}} - \frac{(H-L)C\lambda^2}{[(H-L)^2+R^2]^{3/2}}, \end{aligned} \tag{3.10}$$

respectively. In the next section, we are going to explore in depth the physics of two interacting needles by exploiting Eq. (3.8).

3.3 Magnetic needles

3.3.1 Facing needles

3.3.1.1 Effect of inter-needle separation distance

When dealing with facing magnetic needles (i.e., $H = 0$), the first natural question that arises is how different is the (repulsive) interaction from the well known $1/R^3$-repulsion of two point-like dipoles? The elongated shape of the needles makes obviously the inter-needle interaction non-trivial.

[1] It is realized quickly by summation of the four interactions between the charges Q and $-Q$. Note that the same trick applies to a rod with *finite* diameter [75] [83, pp. 34 ff]. The crucial point here is that the divergence of the polarization/magnetization vanishes within the polar-

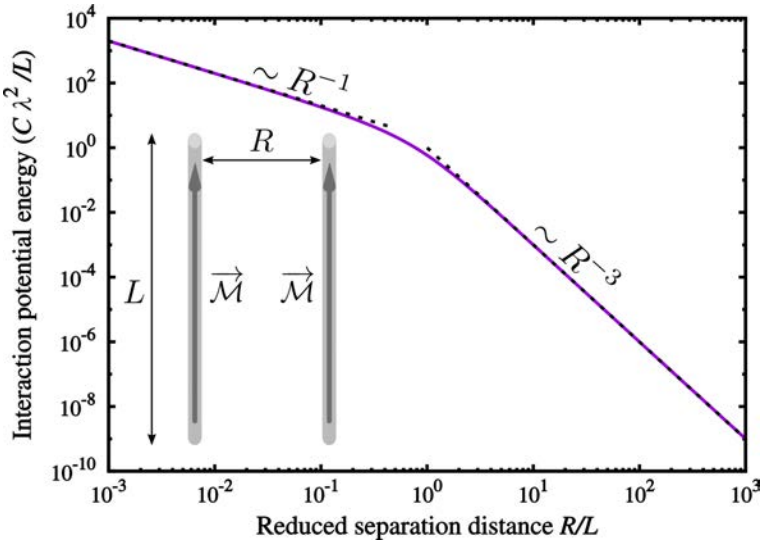

Figure 3.2: Inter-needle interaction potential U_{needles} [see Eq. (3.11)] as a function of the reduced separation distance R/L. Limiting power laws as given by Eq. (3.12) and Eq. (3.13) are indicated with dashed lines. The inset serves as an illustration for the system.

In order to shed light on this intriguing question we rewrite Eq. (3.8) for $H = 0$ at prescribed needle size L, yielding

$$\frac{U_{\text{needles}}(H=0)}{C\lambda^2/L} = \frac{2L}{R} - \frac{2}{\sqrt{1+R^2/L^2}}. \tag{3.11}$$

The corresponding profile of Eq. (3.11) is depicted in Fig. 3.2. As expected at large relative separation distances ($R/L \gg 1$) the behavior of point-like dipoles (with moments $m = \mathcal{M} = \lambda L$) is recovered where

$$\frac{U_{\text{needles}}}{C\lambda^2/L} = \frac{L^3}{R^3} + \mathcal{O}(L^5/R^5) \sim \frac{1}{R^3} \quad (R/L \gg 1). \tag{3.12}$$

As a matter of fact, at separations $R \approx 2.5L$, the value of U_{needles} is already within 10% of that obtained with point-like dipoles.

We now come to the intriguing limit where needles are close compared to their extension ($R/L \ll 1$). A Taylor expansion of U_{needles} in Eq. (3.11) at short separa-

ized/magnetized object.

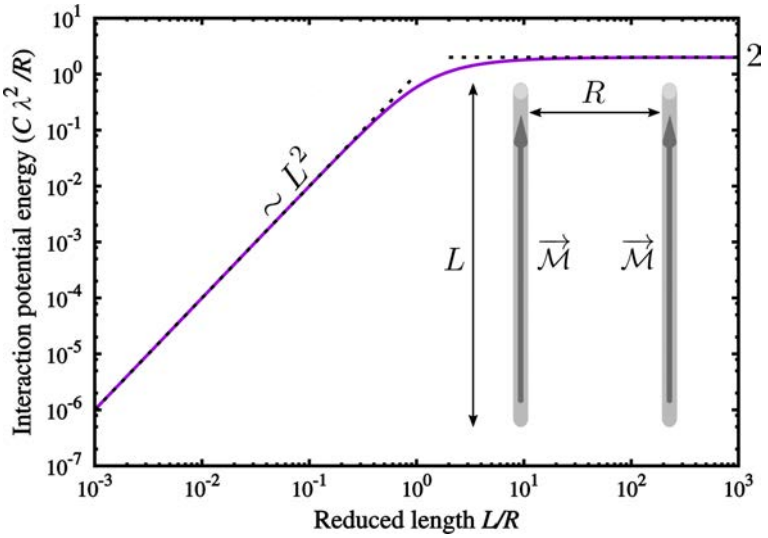

Figure 3.3: Inter-needle interaction potential U_{needles} [see Eq. (3.14)] as a function of the reduced needle length L/R. Limiting power laws as given by Eq. (3.15) and Eq. (3.16) are indicated with dashed lines. The inset serves as an illustration for the system.

tions $R/L \ll 1$ leads to

$$\frac{U_{\text{needles}}}{C\lambda^2/L} = \frac{2L}{R} - 2 + \mathcal{O}(R^2/L^2) \sim \frac{1}{R} \quad (R/L \ll 1) \tag{3.13}$$

showing that a simple inverse power law prevails. This result comes naturally when referring to the dumbbell-like dipole picture. Hence, the repulsive interaction is considerably softened in this regime of short separation distances compared to that occurring with point-like dipoles.

3.3.1.2 Effect of needle length

We now would like to study an other relevant parameter, namely the effect of needle size L at given separation R on the inter-needle interaction. In this situation with $H = 0$ at prescribed separation R, Eq. (3.8) becomes

$$\frac{U_{\text{needles}}(H=0)}{C\lambda^2/R} = 2 - \frac{2}{\sqrt{1 + L^2/R^2}}. \tag{3.14}$$

The profile of Eq. (3.14) is sketched in Fig. 3.3. For short needles ($L/R \ll 1$), one obtains

$$\frac{U_{\text{needles}}}{C\lambda^2/R} = \frac{L^2}{R^2} + \mathcal{O}(L^4/R^4) \sim L^2 \sim \mathcal{M}^2 \quad (L/R \ll 1) \tag{3.15}$$

which evidently reflects again the behavior of two interacting point-like dipoles.

For large needles ($L/R \gg 1$), the potential energy in Eq. (3.14) becomes

$$\frac{U_{\text{needles}}}{C\lambda^2/R} = 2 + \mathcal{O}(R/L) \quad (L/R \gg 1) \tag{3.16}$$

suggesting a non-trivial saturation behavior for large needles. [2] Again, this result (3.16) is immediate with the magnetic charges picture. It is to say that when needles are large enough, their mutual repulsion remains unchanged upon increasing their size. This phenomenon is due to a *long range screening* mediated by dipolar interactions that involve pairs lying outside the magic angle, see drawing in Fig. 3.4.

To better understand and describe this screening effect, we consider the interaction between a needle and a nearby symmetrically placed point-like dipole as sketched in the drawing of Fig. 3.4. This interaction potential energy can be written as follows

$$U_m^{\text{needle}} = C\lambda m \int_{-L/2}^{L/2} dz \frac{1}{(z^2+R^2)^{3/2}} - 3C\lambda m \int_{-L/2}^{L/2} dz \frac{z^2}{(z^2+R^2)^{5/2}}, \tag{3.17}$$

which after integration leads to [3]

$$U_m^{\text{needle}} = C\lambda m \frac{L}{(R^2+L^2/4)^{3/2}}. \tag{3.18}$$

The corresponding profile of Eq. (3.18) is depicted in Fig. 3.4, where two typical

[2] Notice that Eqs. (3.13) and (3.16) are essentially the same but merely differ by the energy normalization.

[3] Notice that result (3.18) could be equally well obtained with the magnetic charges representation. Firstly, one computes the magnetic field, $\vec{B}_\pm$, produced by the two poles of the needle at $\vec{m}$-location, which reads: $\vec{B}_\pm = -C\lambda L(R^2+L^2/4)^{-3/2}\vec{e}_z$. Then, inserting this expression in $U_m^{\text{needle}} = -\vec{m}\cdot\vec{B}_\pm$, one arrives at Eq. (3.18). This being said, the screening argument would not be appropriate in this approach.

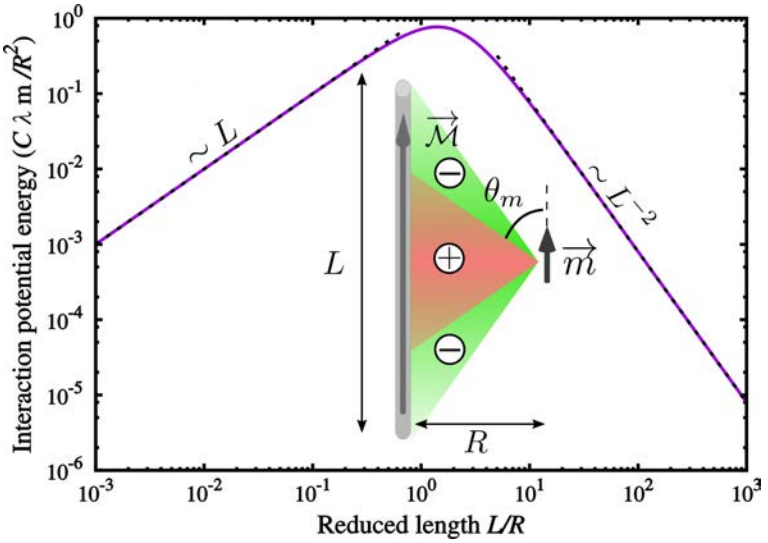

Figure 3.4: Potential of interaction between a needle and a test point-like dipole U_m^{needle} [see Eq. (3.18)] as a function of the reduced needle length L/R. Limiting power laws as given by Eq. (3.19) are indicated with dashed lines. The shaded region (with plus sign) of the inset represents the angular field (prescribed by the magic angle θ_m) where interacting pairs (i.e., the point-like dipole and the infinitesimal elements of the needle) contribute *positively* to the potential energy. All the other pairs lying outside this "positive" zone contribute *negatively* (signaled by minus sign in the concerned areas) to the potential energy and are responsible for the screening.

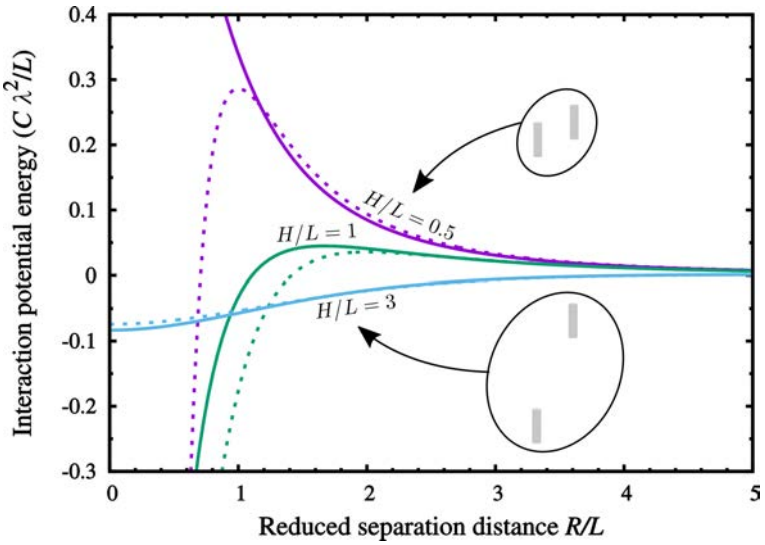

Figure 3.5: Inter-needle interaction potential U_{needles}, see Eq. (3.8), as a function of the reduced separation distance R/L for several reduced shifts H/L. The profiles for point-like dipoles with $\vec{m} = \vec{\mathcal{M}}$ are shown with dashed lines. The insets provide a sense of scale for $H/L = 0.5$ and $H/L = 3$.

regimes emerge:

$$\frac{U_m^{\text{needle}}}{C\lambda m/R^2} = \begin{cases} \dfrac{L}{R} + \mathcal{O}(L^3/R^3) \sim L & \text{for } L/R \ll 1, \\ \dfrac{8R^2}{L^2} + \mathcal{O}(R^4/L^4) \sim L^{-2} & \text{for } L/R \gg 1. \end{cases} \tag{3.19}$$

In the regime of short needles the potential energy U_m^{needle} increases with L as expected. However, when needles are large enough the screening is such that the potential energy U_m^{needle} decays as L^{-2}.

3.3.2 Shifted needles

The natural next step is to study the more general case of shifted needles. In that situation two relevant forces come into play: (i) transversal forces (perpendicular to the needles axis) and (ii) longitudinal ones (parallel to the needles axis). These features are going to be discussed in detail in the very next paragraphs.

3.3.2.1 Transversal forces

The starting point of the discussion is the very general expression of potential of interaction energy $U_{\text{needles}}(R, H)$ given by Eq. (3.8). To address transversal forces, we are asked to look at the variation of $U_{\text{needles}}(R, H)$ with respect to inter-needle distance separation R at prescribed inter-needle shift distance H. One has to bear in mind that R always represents the distance between the needles axis, see Fig. 3.1. Typical profiles of $U_{\text{needles}}(R/L)$ for prescribed values of H/L are reported in Fig. 3.5 corresponding to three scenarios:

- At strong shift, see e.g. $H/L = 3$ in Fig. 3.5, the needles virtually behave like point-like dipoles. Thereby, a long range attraction for $R/L \lesssim 6$ sets in.
- At intermediate shift, see e.g. $H/L = 1$ in Fig. 3.5, deviation from the point-like dipole behavior becomes noticeable when the (transverse) separation R is of the order of the needle extension L.
- At small enough shift, see e.g. $H/L = 0.5$ in Fig. 3.5, the needle-needle interaction becomes *purely repulsive* in strong qualitative contrast with the behavior of point-like dipoles.

Whereas when dealing with point-like dipoles the magic angle θ_m is unique, it is no longer true with extended objects such as needles. Hence the *zero energy angle*, θ_U, will depend in a non-trivial way on the reduced separation distance R/L (or equivalently the reduced shift H/L) as a result of the root of

$$U_{\text{needles}}[\theta = \text{atan}(R/H) = \theta_U] = 0. \tag{3.20}$$

It is important to recall that the zero energy angle θ_U does *not* represent an attraction/repulsion transition but merely a *sign switch* in the value of the potential of interaction. In order to access the physically relevant former point, it is the zero (transverse) force angle $\theta_\perp$ defined through the root of

$$F_\perp^{\text{needle}} = -\frac{\partial}{\partial R} U_{\text{needles}}[\theta = \text{atan}(R/H) = \theta_\perp] = 0 \tag{3.21}$$

that we have to look at.

Profiles of zero energy and force angles stemming from Eq. (3.20) and Eq. (3.21) combined with Eq. (3.8) are depicted in Fig. 3.6. The zero force angle $\theta_\perp$ as well as that in energy θ_U grow monotonically with inter-needle separation R/L

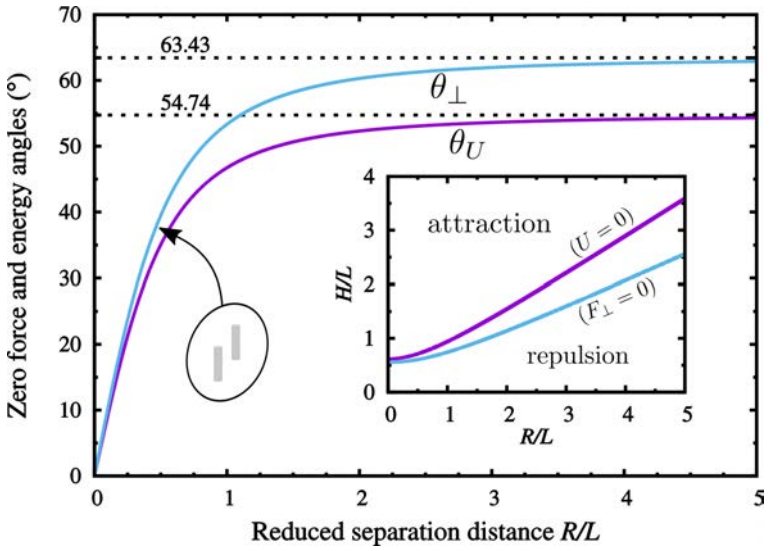

Figure 3.6: Zero energy angle θ_U and zero (transverse) force angle $\theta_\perp$ as a function of reduced inter-needle separation R/L. The limiting values obtained for point-like dipoles with $\vec{m} = \vec{\mathcal{M}}$ are shown with horizontal dashed lines. The inset on the left shows a zero transversal force configuration for $R/L = 0.5$ to provide a sense of scale. The inset on the right shows the curves in the $(R/L, H/L)$-plane verifying $U_{\text{needles}} = 0$ and $F_\perp^{\text{needle}} = 0$ as indicated by $U = 0$ and $F_\perp = 0$, respectively. The regions of attraction ($F_\perp^{\text{needle}} < 0$) and repulsion ($F_\perp^{\text{needle}} > 0$) are indicated.

and saturate to the values of point-like dipoles (i.e., $\theta_\perp \simeq 63.4°$ and $\theta_m \simeq 54.7°$, respectively), see Fig. 3.6. At $R = 2L$, $\theta_\perp$ as well as θ_U are already pretty close to these limiting values within less than 5% deviation. The regime of short separation distance, where the needle-needle separation is smaller or of the order of the needles size ($R \lesssim L$), shows a strong deviation from the point-like dipoles behavior, see Fig. 3.6. As a result, a repulsion/attraction transition in the transverse direction only occurs for shifts larger than a certain critical value $H_\perp^c$ that is roughly the half needle size ($H_\perp^c \simeq 0.56L$). [4] Similarly, a switch in the sign of the potential energy can only occur for a shift larger than $H_U^c/L = \frac{-1+\sqrt{5}}{2} \simeq 0.62$.

3.3.2.2 Longitudinal forces

To have a complete picture of the inter-needle interaction, we now address longitudinal forces. To do so, an inspection of the profiles of $U_{\text{needles}}(H)$ at prescribed reduced inter-needle separation R/L will be insightful, see Fig. 3.7. As expected, a

[4] As a matter of fact it can be readily shown that $H_\perp^c/L$ is the root of $x^6 + 3x^5 - 3x^4 + x^3 + 3x^2 - 1 = 0$.

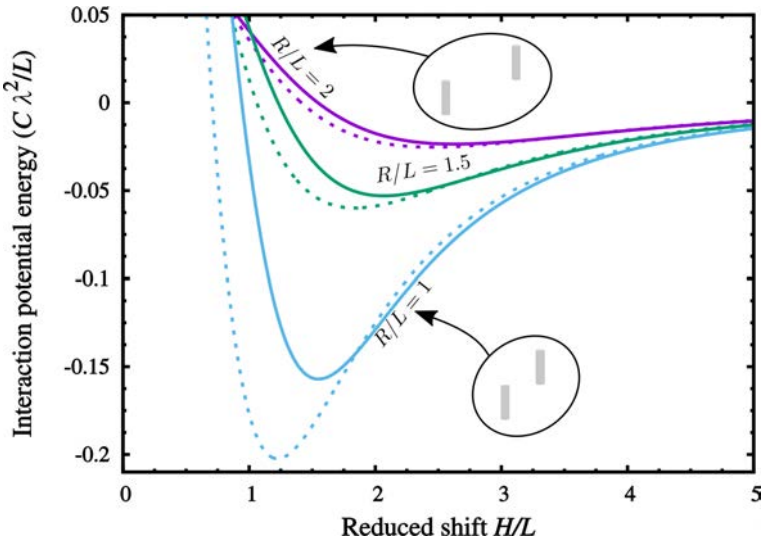

Figure 3.7: Inter-needle interaction potential U_{needles}, see Eq. (3.8), as a function of the reduced shift H/L for several reduced separations R/L. The profiles for point-like dipoles with $\vec{m} = \vec{\mathcal{M}}$ are shown with dashed lines. The insets provide a sense of scale for $R/L = 1$ and $R/L = 2$.

repulsion/attraction transition can be readily seen upon shifting the needles. More specifically, the minimum in $U_{\text{needles}}(H)$ gets deeper when approaching the needles, i.e. by diminishing R/L. Concomitantly, the position of the minimum is shifting to lower values of H/L when decreasing R/L. Notice that minima are always deeper when dealing with equivalent point-like dipoles especially when $R/L \sim 1$, see Fig. 3.7.

The zero energy and (longitudinal) force angles are reported in Fig. 3.8. By analogy with $\theta_\perp$, the zero (longitudinal) force angle $\theta_\parallel$ is defined through the root of

$$F_\parallel^{\text{needle}} = -\frac{\partial}{\partial H} U_{\text{needles}}[\theta = \text{atan}(R/H) = \theta_\parallel] = 0. \tag{3.22}$$

The point-like dipole behavior for both θ_U and $\theta_\parallel$ is recovered from $H/L \gtrsim 2$ within less than 3% and 9% deviation, respectively. Interestingly, attraction is only allowed for non overlapping needles in the longitudinal direction, i.e. $H/L > 1$. Nevertheless, negative values for $U_{\text{needles}}(H)$ can be obtained with $H \geq H_U^c \simeq 0.62L$ as already discussed.

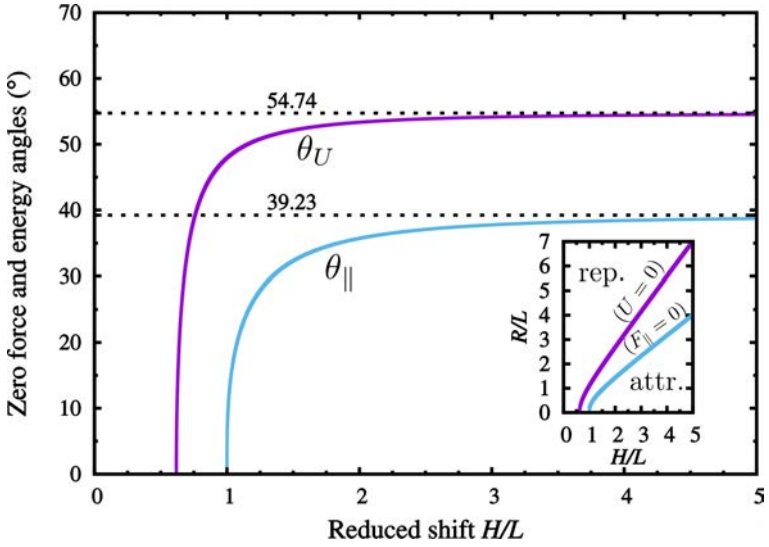

Figure 3.8: Zero energy angle θ_U and zero (longitudinal) force angle $\theta_\parallel$ as a function of reduced inter-needle shift H/L. The limiting values obtained for point-like dipoles with $\vec{m} = \vec{\mathcal{M}}$ are shown with horizontal dashed lines. The inset shows the curves in the $(R/L, H/L)$-plane verifying $U_{\text{needles}} = 0$ and $F_\parallel^{\text{needle}} = 0$ as indicated by $U = 0$ and $F_\parallel = 0$, respectively. The regions of attraction ($F_\parallel^{\text{needle}} < 0$) and repulsion ($F_\parallel^{\text{needle}} > 0$) are indicated.

3.4 Magnetic chains

3.4.1 Facing chains

3.4.1.1 Effect of inter-chain distance separation

After having discussed in depth the physics of the interaction of magnetic needles, we can confidently tackle the homologous case of magnetic chains. It is a good idea to start with facing chains and thereby explore and understand the regimes where whether or not a needles behavior is observed. To perform this task we now dissect the potential of interaction given by Eq. (3.4) at $H = 0$ yielding

$$U_N^{\text{cc}}(R) = \frac{Cm^2}{d^3} \sum_{i=-N+1}^{N-1} (N - |i|) \left\{ \frac{1}{[i^2 + (R/d)^2]^{\frac{3}{2}}} - \frac{3i^2}{[i^2 + (R/d)^2]^{\frac{5}{2}}} \right\}. \tag{3.23}$$

To make the comparison with needles meaningful we recall that $\vec{\mathcal{M}} = N\vec{m} = \lambda L \vec{e}_z$ and $L = Nd$ so that $\lambda = m/d$, whereas point-like dipoles are realized when $N = 1$. Profiles of $U_N^{\text{cc}}(R)$ as given by Eq. (3.23) can be found in Fig. 3.9 where three regimes emerge:

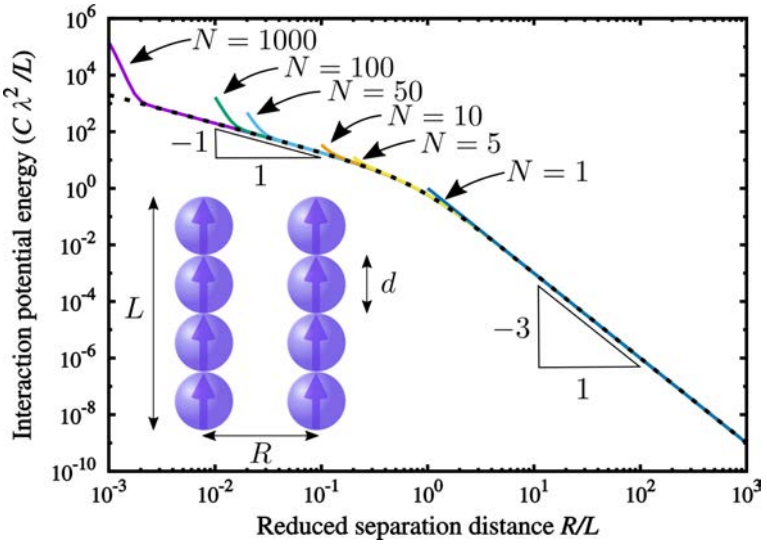

Figure 3.9: Profiles of the inter-chain interaction potential $U_N^{\rm cc}$ [see Eq. (3.23)] as a function of the reduced separation distance R/L for different number of beads N. The profile for needle-needle interaction [see Eq. (3.11)], identical to that in Fig. 3.2, appears as a dashed line. The inset serves as an illustration for the system (there $N = 4$).

- Distant chains with $R/L \gtrsim 2$ behave like point-like dipoles, i.e. $U_N^{\rm cc} \sim R^{-3}$, as expected.

- At an intermediate separation a typical needle-like behavior is recovered with the typical softening characterized by $U_N^{\rm cc} \sim R^{-1}$.

- Interestingly, at very short separation close to contact ($R/d \lesssim 2$), a *hardening* sets in. The latter is due to the discrete nature of the dipole moments that enhances the repulsion near contact. [5] The distance dependence in the hardening regime, see Fig. 3.9, is a complicated matter and moreover shows a non-trivial behavior as a function of N. It is careful to introduce the relative energy deviation, $\delta U_N^{\rm cc}$, defined as

$$\delta U_N^{\rm cc} = \frac{U_N^{\rm cc} - U_{\rm needles}}{U_N^{\rm cc}}, \tag{3.24}$$

  whose profiles as a function of R/d can be found in Fig. 3.10. It reveals that the distance interval (say $R_{\rm hardening}/d$) where hardening sets in is a very slowly (roughly logarithmically) growing function of N.

[5] Note that this hardening effect would still be present and quantitatively identical if the beads were uniformly magnetized over the volume or surface.

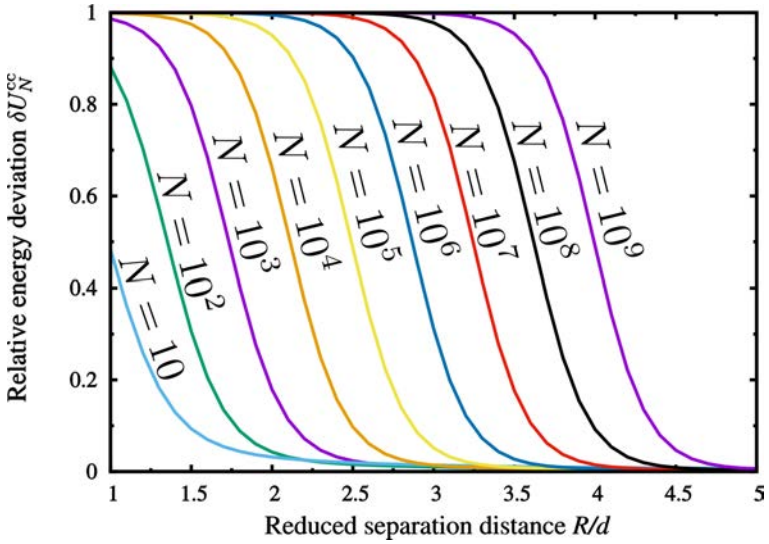

Figure 3.10: Relative energy deviation profiles δU_N^{cc} [see Eq. (3.24)] as a function of the reduced separation distance R/d for several values of N.

3.4.1.2 Effect of chain length

In order to study the effect of chain length and to be in a position to compare it with that of needle length we will consider the common reduced length L/R. Profiles of $U_N^{cc}(L/R)$ for several values of N are sketched in Fig. 3.11, where three regimes can be clearly identified:

- At sufficiently large chain separation (i.e., $L/R \lesssim 0.3$) a point-like dipole is recovered where $U_N^{cc} \sim L^2$ as it should be.
- A plateau sets in at intermediate reduced chain length L/R. The width of this plateau increases in an non-trivial manner with the number of beads N.
- For chains near contact $R/d \lesssim 2$, the interaction potential energy U_N^{cc} increases again due to a *weaker screening* with discrete beads. In this regime, a high number of beads N enhances this increase in potential energy.

To gain more insight into the degree of repulsion screening occurring with chains, we consider the analogous approach of a needle interaction with a point-like dipole that is contained in Eq. (3.18). Thereby, the potential of interaction for a chain standing next to a bead, $U_N^{cm}(R)$, see also inset of Fig. 3.12, reads:

$$U_N^{cm}(R) = \frac{Cm^2}{d^3} \sum_{i=-(N-1)/2}^{(N-1)/2} \left\{ \frac{1}{[i^2 + (R/d)^2]^{\frac{3}{2}}} - \frac{3i^2}{[i^2 + (R/d)^2]^{\frac{5}{2}}} \right\}. \tag{3.25}$$

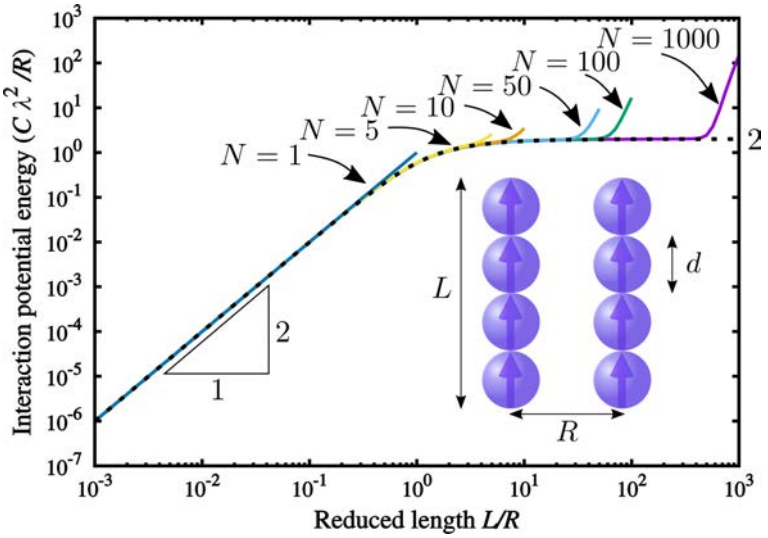

Figure 3.11: Inter-chain interaction potential $U_N^{\rm cc}$ [see Eq. (3.23)] as a function of the reduced length L/R for several values of N. The profile for needle-needle interaction [see Eq. (3.14)], identical to that in Fig. 3.3, appears as a dashed line. The inset serves as an illustration for the system.

The case $N = 1$ can serve as a reference for the *unscreened* repulsion between two equally elevated point-like dipoles, see Fig. 3.12. Upon increasing the chain length or equivalently N, one notices that the repulsion, more precisely the value of $U_N^{\rm cm}(R)$ as well as its (sign changed) derivative, diminishes near the contact zone, see Fig. 3.12. However, in contrast to the needle case, the screening is only *partial* for chains even at $N \to \infty$ owing to the discrete nature of the constitutive beads, see Fig. 3.12. The contact values of the interaction potential energy $\tilde{U}_N^{\rm cm}(\tilde{R}) = \frac{U_N^{\rm cm}(R)}{U_{\uparrow\uparrow}}$ (recalling that $\tilde{R} = R/d$) and especially that of the force

$$\tilde{F}_N^{{\rm cm}(\perp)}(\tilde{R}) = -\frac{\partial \tilde{U}_N^{\rm cm}}{\partial \tilde{R}} = \sum_{i=-(N-1)/2}^{(N-1)/2} \frac{3\tilde{R}}{\left(i^2+\tilde{R}^2\right)^{5/2}} - \frac{15 i^2 \tilde{R}}{\left(i+\tilde{R}^2\right)^{7/2}} \tag{3.26}$$

quickly saturate upon increasing N toward $\tilde{U}_{N\to\infty}^{\rm cm}(\tilde{R}=1) \simeq 0.146$ and $\tilde{F}_{N\to\infty}^{{\rm cm}(\perp)}(\tilde{R}=1) \simeq 0.989$, respectively. These values can be compared to the contact values for the unscreened case ($N = 1$), see Fig. 3.12, where $\tilde{U}_1^{\rm cm}(1) = 1$ and $\tilde{F}_1^{{\rm cm}(\perp)}(1) = 3$, see also Eq. (2.12).

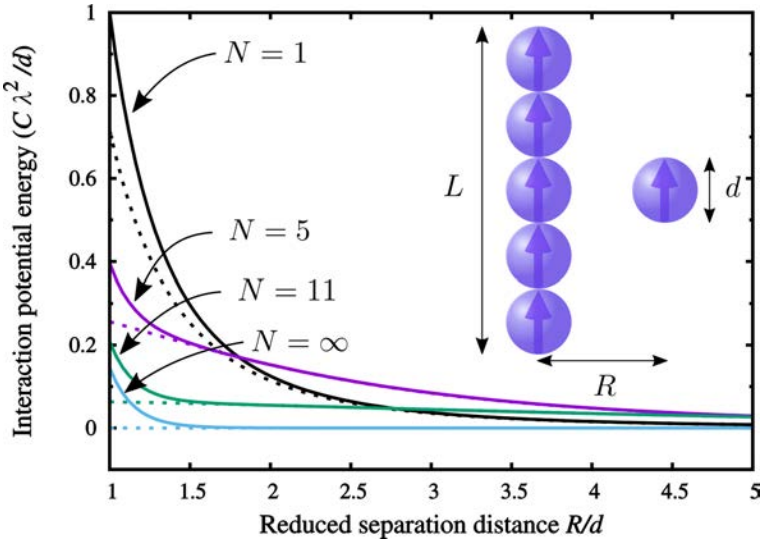

Figure 3.12: Potential of interaction between a chain and a test point-like dipole $U_N^{\rm cm}$ [see Eq. (3.25)] as a function of the reduced separation distance R/d. Dashed curves correspond to the situation where the chain is replaced by a needle of same length L and same (global) dipole moment $N\vec{m}$. The inset serves as an illustration of the system (there $N = 5$).

3.4.2 Touching shifted chains

In the light of what precedes, it is expected that *shifted* chains will behave like needles as soon as the chains are not in the contact zone. A careful separate analysis, see Fig. 3.10, indicates that the inter-chain separation R/d is a very slowly (roughly logarithmically) growing function of N at prescribed relative energy deviation $\delta U_N^{\rm cc}$. In order to have a good representation of excluded volume correlations and dipolar interactions for shifted magnetic chains we will consider two relevant cases: (i) *barely touching chains* with $\tilde{R} = 1$, as also done by Jennings et al. [84] in the past, where one bead is touching at most one bead of the other chain and (ii) *assembled chains* having the shortest possible separation $\sqrt{3}/2 \leq \tilde{R} \leq 1$ at given shift so that one bead can touch up to two beads of the other chain.

The inter-chain potential of interaction for $N = 10$, see Eq. (3.4), as a function of the reduced shift $\tilde{H} = H/d$ can be found in Fig. 3.13. An oscillatory behavior is reported giving rise to alternating longitudinal attraction/repulsion upon shifting the chains. Thereby, the periodicity is essentially dictated by the bead size. In more detail, the highest energy is obtained for (unshifted) facing chains where $H = 0$, see Fig. 3.13. Then, upon shifting the two chains the energy first decays until $\tilde{H} = 1/2$ when $\tilde{R} = \sqrt{3}/2$ (for assembled chains in contact) and $\tilde{H} \simeq 0.53$ when

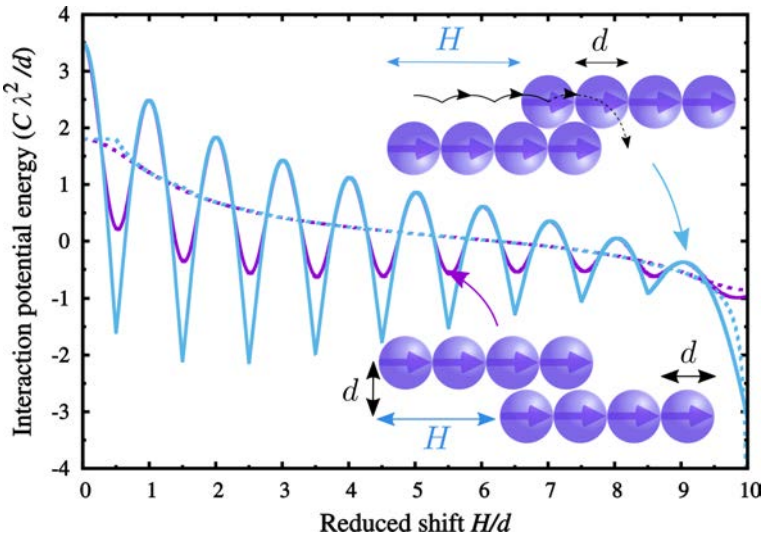

Figure 3.13: Reduced potential of interaction between two shifted chains $\tilde{U}_{10}^{cc}$ [see Eq. (3.4)] as a function of the reduced shift H/d. Dashed curves correspond to the situation where the chains are replaced by needles of same length L and (global) dipole moment $10\vec{m}$. The lower inset illustrates the situation where chains have a fixed transverse separation $R = d$ that is referred to as barely touching chains (there $N = 4$). The upper inset shows the path of the end-bead for gliding chains in contact (there $N = 4$).

$\tilde{R} = 1$ (for barely touching chains). This first local minimum is significantly deeper for assembled chains with touching beads where $\tilde{H} = \sqrt{3}/2$, see Fig. 3.13. By further shifting the two chains, oscillations take place where the *global minimum* is reached for assembled chains at $\tilde{H} = 5/2$. This latter point is discussed in depth in a separate publication [45] where it is shown that this shift of two and half beads always leads to the global minimum of two assembled chains.

3.5 Concluding remarks

To summarize, we have shed some light on the problem of interacting magnetic filaments. By revisiting the effective interaction of dipolar needles we have been in a position to better understand and characterize the interaction of magnetic chains.

The most significant signature for the interaction of needles is the *softening* occurring at short separation (compared to the needle size) characterized by an inverse power law R^{-1} of the transverse separation R. The origin of this softening is a long range screening mediated by attractive pairs compensating the repulsion stemming from neighboring pairs, see Fig. 3.4. In general, a dipole-like behavior is

recovered when the needles are separated by distances of the order of the needles itself. A repulsion/attraction transition takes place for smaller (longitudinal) shifts than with point-like dipoles for the transverse component of the force. The trend is reversed for the longitudinal component of the force.

Dipolar chains (in registry) exhibit a typical *hardening* at very short separation, i.e. when they are separated by a few beads size. This feature is in strong qualitative contrast with the needle behavior and it is due to the discrete nature of the chains. In this regime of inter-chain separation, the discretization matters and as a result the screening of facing bead-pairs by distant ones becomes less efficient. Otherwise, at the *contact* zone, a remarkable non-trivial oscillatory behavior in the inter-chain pair potential, whose periodicity is dictated by the bead size, sets in for shifted chains.

This work should be helpful to predict and/or to explain to some extent the phase behavior encountered in experimental dipolar systems such as magnetic nanomaterials [57, 73, 85, 86, 87, 88], living and bio-inspired systems [19, 65, 89], polymeric/colloidal systems [5, 90, 91, 92] or granular piles [93]. In particular, the *ribbon formation* consisting of magnetic chains that has been reported experimentally by several researchers [9, 74, 94] can be accounted for by our study.

Chapter 4

Bundles of dipolar chains

This chapter provides a theoretical investigation of the columnar aggregation of dipolar chains published in *Europhysics Letters* [95].

Contents

4.1 Introduction 37
4.2 Model 38
4.3 Method 40
4.4 Infinitely long chains 40
4.5 Finite-size chains 43
4.6 Concluding remarks 45

4.1 Introduction

A well-known and spectacular effect in dipolar systems is the formation of chain-like structures that can be achieved even with zero magnetic/electric field [48]. These dipolar chain-like systems are ubiquitous in the every-day life and have many potential applications. In the biological world, so-called *magnetotactic bacteria* own a permanent magnetic moment and the resulting chain structure can act as a cellular compass needle [64, 96, 97]. In nanotechnology, dipolar chains can be employed to develop the next generation of hard drives [98].

The intriguing association of linear dipolar chains has been actively studied in various experiments [5, 9, 77, 94, 99, 100, 101]. A mechanism based on lateral aggregation that is fluctuation mediated was first suggested by Halsey and Toor [36]. Later, Martin *et al.* [102] showed by computer simulation that, even in the absence of thermal fluctuations, topological defects in chains still lead to lateral coarsening. Weis also reported ribbon-like formation in two-dimensional systems by computer

simulations [103, 104] corroborated theoretically by Messina *et al.* [45, 63]. Closely related to our systems of interest, Faraudo *et al.* [105] as well as Martin *et al.* [106] observed the formation of bundles of chains in zipper configurations in their computer simulations.

From a theoretical viewpoint, it is of fundamental importance to understand the ground state of dipolar systems and especially here the case of bundles of chains. The non-trivial self-assembly originating from dipolar interactions is very challenging to understand due to the long range and strong anisotropy involved there. The theoretical pioneering works in the 1990's Halsey and Toor [36, 37] and those of Tao and Sun [38, 107] addressing the ground state of a bulk dipolar crystal have immensely helped scientists and engineers to understand the phase behavior of dipolar colloidal suspensions. A crucial finding is the body-centered tetragonal (bct) structure as the bulk ground state. For finite systems, the role of *rings* is essential in the low temperature limit (with no external magnetic/electric field) [33, 34, 41, 44, 108, 109, 110, 111].

4.2 Model

The length scale of the system is set by the diameter $d = 1$ of the spherical dipolar particle whose dipole moment strength is $m = |\vec{m}| = 1$, see Fig. 4.1.

N infinitely long ferromagnetic chains are generated by N dipolar spheres in a unit cell that are periodically repeated in z-direction, see Fig. 4.1. In general, for such a unit cell containing N dipolar particles located at $\vec{r}_1, \ldots, \vec{r}_N$, the dipolar energy per unit cell, U_{cell}, is given by:

$$\begin{aligned} U_{\text{cell}} &= \frac{1}{2}\sum_{i,j}^{N}{\sum_{\vec{\mathcal{N}}_z}}' \frac{C}{|\vec{r}_{ij}+\vec{\mathcal{N}}_z|^3} \\ &\times \left[m^2 - 3\frac{\left[\vec{m}\cdot(\vec{r}_{ij}+\vec{\mathcal{N}}_z)\right]^2}{|\vec{r}_{ij}+\vec{\mathcal{N}}_z|^2} \right], \end{aligned} \tag{4.1}$$

where $\vec{\mathcal{N}}_z = \mathcal{N}_z \vec{n}_z$ designates the Bravais vector along the z-axis ($\vec{n}_z$ being the unit spanning vector, see also Fig. 4.1) with integer component $\mathcal{N}_z$ ranging from $-\infty$ to $+\infty$. The prime in Eq. (4.1) indicates that, when $\vec{n}_z = 0$, i must be different from j. In order to overcome the slow convergence in Eq. (4.1), an efficient Lekner-like sum technique for systems with periodicity in one direction was used [112]. The

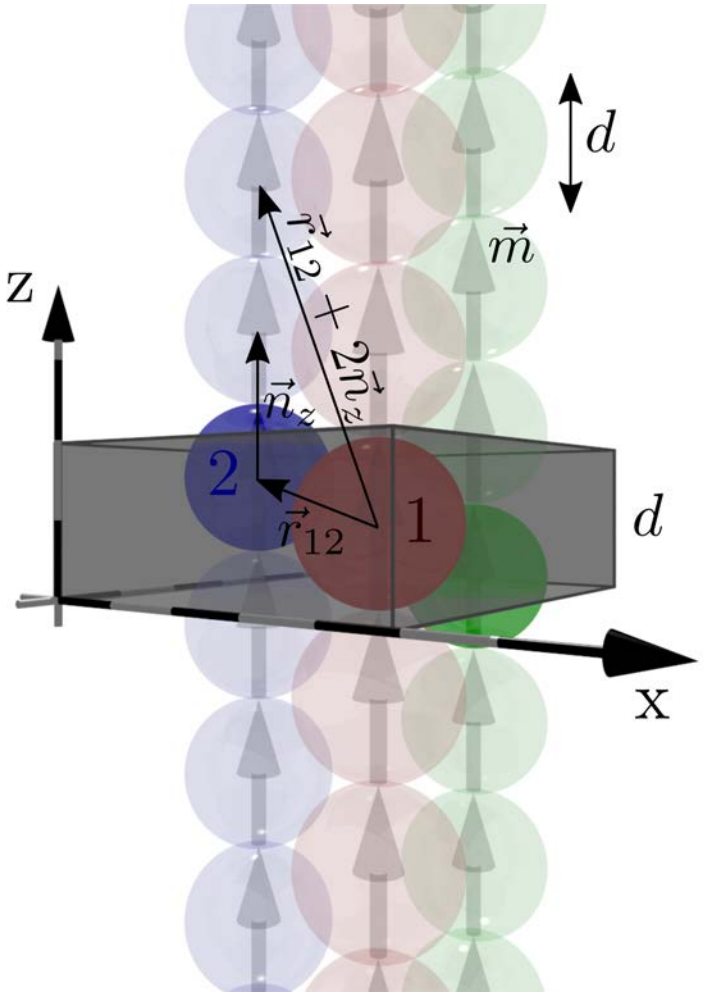

Figure 4.1: (colour on-line) Scheme of the geometrical setup for interacting infinite dipolar chains. A unit cell containing three spherical dipolar particles ($N = 3$) with its periodic replica are shown, see also text.

energy scale is set by $U_{\uparrow\uparrow}$, see Eq. (2.10). Thereby, the binding energy per particle, u_N, is merely given by $u_N = \frac{1}{N}\frac{U_{\text{cell}}}{U_{\uparrow\uparrow}}$.

4.3 Method

The minimization of u_N involves $3N$ parameters which are the Cartesian coordinates of the constitutive particles in the unit cell. The efficient method called SLSQP, taking natively into account constraints and requiring derivatives of the objective function [62], is employed, see Section 2.3.2. In order to find the global minimum, typically 10^3 to 10^6 starting random configurations were considered. More efficiency is gained when considering touching (percolating) chains to start the minimization procedure.

4.4 Infinitely long chains

An overview of our minimization results can be found in Fig. 4.2. A detailed phase diagram as a function of the number of chains N is provided there, where Fig. 4.2(a) indicates the profile of the (reduced) binding energy u_N accompanied with the corresponding microstructures. Top views of these chain bundles together with the corresponding energy values are gathered in Fig. 4.2(b) for the sake of clarity and completeness. A remarkable general feature is that the minimal energy structures always consist of a compact columnar aggregation made up of zippered chains. More specifically, two touching dipolar chains possess the shortest possible separation between chain-axes $\frac{\sqrt{3}}{2}$ corresponding to a vertical shift along the z-axis of $1/2$, see also Fig. 4.2(a) for $N = 2$.

It is instructive to compare the binding energy gain relative to the purely two-dimensional ribbon case made up of N infinite chains, see Fig. 4.2(a). In the regime of (very) little $N < 4$, it is the ribbon structure that possesses the lowest energy, see Fig. 4.2(a). At $N = 4$, the relevant square base structure sets in with a strong energy drop. Besides, the binding energy $u_4 = -2.744$ is already very close to that of an infinitely wide ribbon (i.e., perfect hexagonal lattice) which is -2.759 [44]. The binding energy keeps on decreasing until $N = 6$ where a local minimum in the u_N-profile is reached. [1] This special minimum occurring at $N = 6$ corresponds to a

[1] Note that in this regime of small number of chains N, the five-chain bundle is exceptionally lower in energy than the four-chain structure with a square base ($u_5 < u_4$), see also Fig. 4.2. This

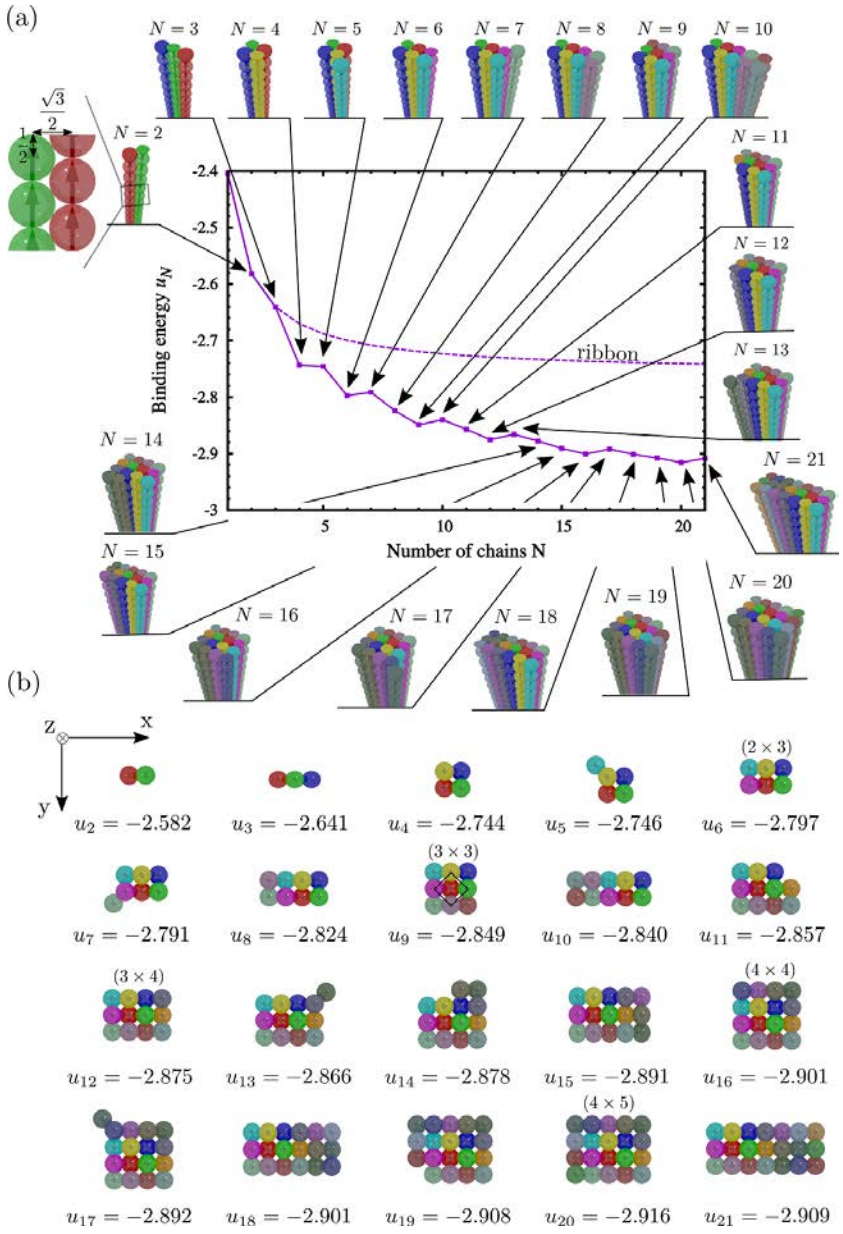

Figure 4.2: (colour on-line) (a) Reduced binding energy profiles u_N as a function of the number of infinitely long chains N. All the ground states are depicted with a perspective view. A cross section of the chain bundles is realized to better visualize the three-dimensional columnar arrangement. The energy profile of two-dimensional ribbons made up of N chains is also shown for the sake of comparison. A side view is also sketched for $N = 2$ to illustrate the typical vertical shift of $1/2$ between two touching chains, as well as the distance of closest approach $\sqrt{3}/2$ between the chain axes. (b) Top view of the ground states with the corresponding energy values u_N. An example of local bct arrangement is marked by a black unit cell for $N = 9$. The special rectangular and square bases leading to local minima in u_N are indicated for $N = 6, 9, 12, 16, 20$, see also Eq. (4.2).

perfect (2×3)-particle rectangular base, see also Fig. 4.2(b) for $N = 6$. The latter can also be seen as the result of removing a one particle-thick edge from the the square base of the nine-chain bundle, i.e., $((3-1) \times 3)$-particle base, see also Fig. 4.2(b) for $N = 9$.

As a matter of fact, this turns out to be a general rule: A chain bundle possessing a $((p-1) \times p)$-particle rectangular base, with p denoting an integer (larger than three), will always be a local minimum in the u_N-profile, see $N = 6, 12, 20$ in Fig. 4.2 with $p = 3, 4, 5$, respectively. The other special kind of ground states leading to local minima in the u_N-profile correspond to $(p \times p)$-square base chain bundles, see Fig. 4.2 with $N = 9, 16$ corresponding to $p = 3, 4$, respectively. Hence the base of these advocated stable structures follow a helical-like pathway that can be written as:

$$(2 \times 3) \to (3 \times 3) \to (3 \times 4) \to (4 \times 4) \to \ldots, \tag{4.2}$$

see also Fig. 4.2(b) for $N = 6, 9, 12, 16, 20$. It is worth to mention that the underlying lattice of these special stable structures (with square or rectangular base obeying Eq. (4.2)) coincides *exactly* with the bct one [38, 42]. Between two such consecutive local minima in u_N, a non-trivial phase behavior sets in when increasing N, see Fig. 4.2. Typically, two scenarios occur for these structures whose base do not obey Eq. (4.2):

(i) When the base is rectangular, see Fig. 4.2 for $N = 8, 10, 15, 18$, the structure is defect-free coinciding with a bct lattice.

(ii) Defects, i.e. vacancies or excess particles relative to the regular base following Eq. (4.2), emerge, see Fig. 4.2 with $N = 5, 7, 11, 13, 14, 17, 19$. In that situation, the underlying bct lattice is very slightly distorted. [2]

Having shown that chain-bundles are governed by an underlying bct lattice, a natural question that arises is: Upon increasing N, how fast does the binding energy u_N reach the bct bulk limit $u_\infty =: u^{(\mathrm{bct})} = -3.050$ [38]? In this context, it is useful

effect is merely due to strong finite size effects there.

[2] A meticulous inspection of the energy values of structures with defects reveals very tiny energy differences when compared to those stemming from a perfect undistorted bct lattice. Typically, only the fourth or higher digit of precision is affected.

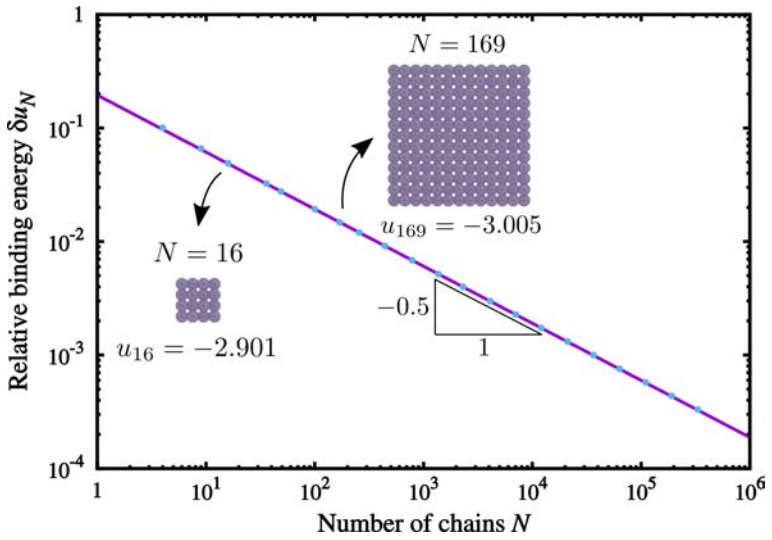

Figure 4.3: (colour on-line) Relative energy deviation profiles δu_N, see Eq. (4.3), as a function of the number of chains N for bundles with square base. For convenience, only some values of N are shown (blue dots) covering roughly six decades. The solid line is the best fit yielding a power law of the form $N^{-0.50}$. Two cross sections for $N = 16$ and $N = 169$ are sketched.

to introduce the relative energy difference, δu_N, defined as follows

$$\delta u_N = \frac{u_N - u^{(\mathrm{bct})}}{u^{(\mathrm{bct})}}. \tag{4.3}$$

Results for δu_N concerning square bases are provided in Fig. 4.3 over six decades. [3] The bct-limit energy is rather already nearly reached with a relative deviation of about 5% with $N = 16$ and 3% when $N = 36$. Interestingly, the energy deviation obeys $\delta u_N \sim 1/\sqrt{N}$. A very similar behavior was also reported in two-dimensional self-assembly of dipolar spheres [44].

4.5 Finite-size chains

We now would like to address the problem of columnar aggregation with chains of *finite* size. Thereby, the chain bundle corresponds now to a truncated (infinitely) long one, when each constitutive chain is made up of n beads, see inset of Fig. 4.4. [4] This system should be also of interest for the experimentalist who is manipulating

[3] Notice that in this situation no minimization is required.

[4] For bundles with finite chains, a straightforward brute force sum is performed to compute the binding energy. It is to say that no Lekner-like sum is employed.

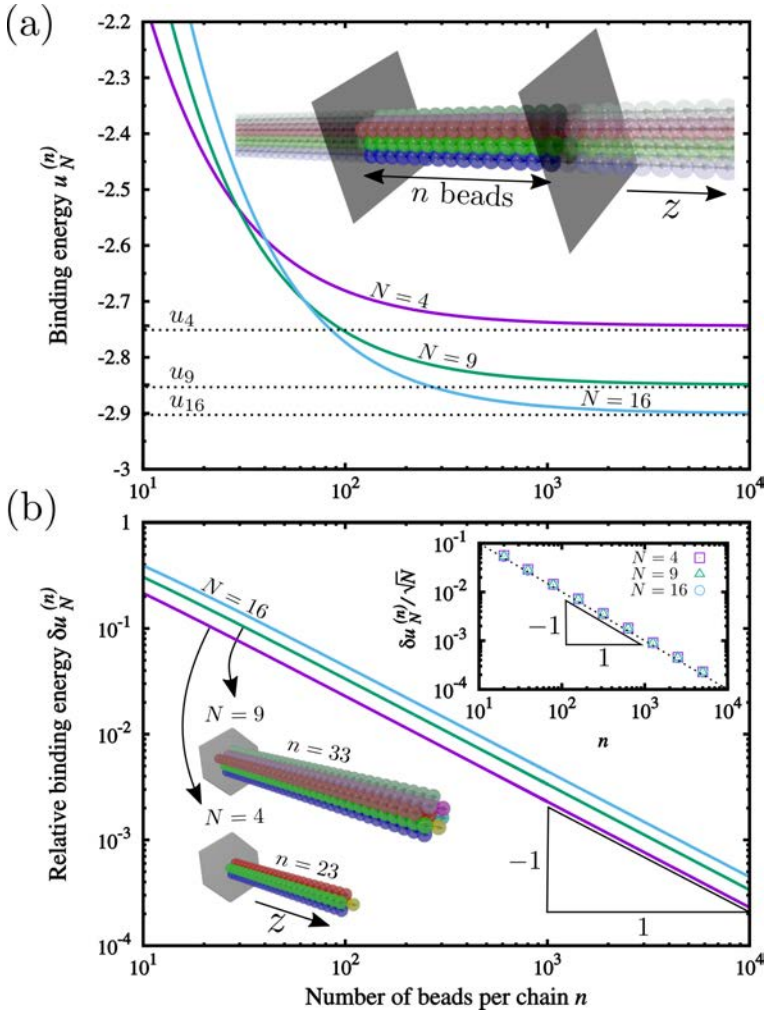

Figure 4.4: (colour on-line) (a) Reduced binding energy $u_N^{(n)}$ as a function of the number of beads n of the constitutive chains for chain-bundles with square base containing $N = 4, 9$ and 16 particles. The limiting energy values u_N obtained for infinite chains (i.e., when $n \to \infty$) are shown with horizontal dashed lines. The inset serves as an illustration for the meaning of the extracted (truncated) chain bundle of length n from the infinite chain bundle. (b) Reduced energy deviation profiles $\delta u_N^{(n)}$ as a function of n for $N = 4, 9$ and 16, see Eq. (4.4). The top right inset represents the rescaled energy deviation $\delta u_N^{(n)}/\sqrt{N}$. Microstructures are provided as inset, see bottom left, for $N = 4$ and 9 with $n = 23$ and 33, respectively, both corresponding to about 10% energy deviation.

finitely sized chains [48, 113, 114]. Profiles of the reduced binding energy, $u_N^{(n)}$, for three square cross sections with $N = 4, 9, 16$ are depicted in Fig. 4.4(a). Illustrative microstructures for these three square cross sections are provided as an inset in Fig. 4.4(b). Figure 4.4(a) tells us that the constitutive chains have to be long enough in order to qualitatively recover the behavior encountered with infinitely long chains. More specifically, the large the base the more stable the structure (i.e., $u_4 > u_9 > u_{16}$). Roughly, hundred beads are necessary to recover the expected (qualitative) behavior of infinite chains, see Fig. 4.4(a).

It is also insightful to quantify how fast the binding energy converges towards that of bundles with infinite chains (i.e., $u_N = u_N^{(\infty)}$). In the same spirit as δu_N given by Eq. (4.3), one now defines the energy deviation relative to infinite chains, $\delta u_N^{(n)}$, as

$$\delta u_N^{(n)} = \frac{u_N^{(n)} - u_N}{u_N}, \tag{4.4}$$

whose profiles can be found in Fig. 4.4(b). A remarkable power law in $1/n$ emerges, see Fig. 4.4(b), indicating a rather slow convergence. For instance, 1% deviation is observed when n is about $230, 340, 450$ for $N = 4, 9, 16$, respectively. Interestingly, a master curve is obtained upon rescaling $\delta u_N^{(n)}$ by $\sqrt{N}$, see inset of Fig. 4.4(b). These findings explain why chain bundles may have worse (i.e., less negative) binding energy than for ribbons as experimentally found for finitely sized chains made up of aligned glass spheres under an external electric field [113].

4.6 Concluding remarks

In summary, we have investigated the columnar assembly of N dipolar chains. An essential finding is the remarkable stability of chain bundles with square base. Rectangular bases with aspect ration close to unity represent also especially low energy ground states. A general notable result is the underlying bct lattice for all the ground states at any N. It was also shown that the bulk binding energy is reached with a rate governed by $1/\sqrt{N}$. We have also looked at the case of *finite* chains of length n and found that the relative energy deviation from the infinite case also follows a power law like $1/n$.

In the regime of very small number of chains $N \leq 3$, the ribbon structure is the winning one. However, for finite chains, the ribbon structure can persist up to

about hundred beads per chain with $N = 4$. More generally, our findings shed light on the experimentally observed columnar microstructures of glass spheres [113] or single-wall carbon nanotube polymer composites [115] under external electric field.

As part of works for this thesis, it has also been demonstrated [116] in Chapter 8 that the so-called clinohexagonal prism phase accounts for all the ground states in the bulk prepared at any prescribed density. In this respect, it would be interesting to explore in a future study the combined effect of (cylindrical) confinement and density on the the underlying lattice of the columnar aggregation of dipolar chains where helicity is expected [117, 118, 119].

Chapter 5

Dipolar chains: From linear to helical form

The study on the highly challenging interaction of two helical dipolar chains described in this chapter has also been submitted for publication in *The Journal of Chemical Physics* [120].

Contents

5.1 Introduction 48

5.2 Model and computational details 48

5.2.1 Helical chain geometry 48

5.2.2 Dipole-dipole interaction 51

5.2.3 Energy minimization 52

5.3 Dipolar linear chains 52

5.3.1 Single linear chain 52

5.3.2 Interaction of two linear chains 53

5.4 Dipolar zigzag chains 55

5.4.1 Single zigzag chain 55

5.4.2 Interaction of two zigzag chains 58

5.5 Dipolar helical chains 60

5.5.1 Single helical chain 60

5.5.2 Interaction of two helical chains 62

5.6 Concluding remarks 67

5.1 Introduction

Helical structures are ubiquitous in nature and scattered over a broad range of length scales. On the macroscopic scale, objects such as screws and spiral springs are common examples from the every-day life. On the molecular scale, the so-called α-helix [121, 122] present in proteins or the DNA double helix [123] are essential constituents in the realm of cell biology. On the nanoscale, bacterial flagella [124] and microtubules [125] are other relevant biological examples. In physical chemistry, carbon nanotubes [126, 127] or iron ones [128] and metal nanowires [129] can also exhibit helical motives. In complex fluids, helical morphologies emerge in self-assembled colloids in cylindrical confinement [117, 118, 130, 131, 132] or in V-shape grooves [133]. A compressed semiflexible polymer confined in a nanochannel leads to helix formation too [134]. In a similar context, helix formation can be kinetically driven during the homopolymer collapse process [135].

Dipolar particles can facilitate and/or induce the formation of self-assembled helical architectures. For instance, molecular magnets in suitable solvent can lead to supramolecular chirality of wormlike micelles [136]. Magnetic colloids can self-assemble into helical structures without the need for pre-existing templates [137, 138]. Similarly, experiments with so-called Janus particles (characterized by two different hemispheres leading to anisotropic pair potential) reveal spectacular spontaneous helical superstructures [139] that are corroborated by computer simulations [140]. More generally, patchy particles can be the siege of predictive supracolloidal helices [141].

It turns out that much less is known, especially on the theoretical side, about the interaction between dipolar helical structures. However, some theoretical attempts have been proposed in the past to elucidate interacting *charged* helices supposed to mimic DNA-DNA interaction [142, 143, 144, 145]. Thereby, it is legitimate to want to understand what are the basic physical mechanisms involved in the interaction of dipolar helices.

5.2 Model and computational details

5.2.1 Helical chain geometry

We extend the single helical chain model employed by Stanković *et al.* [119] to the case of two interacting helical chains. Consider two (infinite) helical parallel

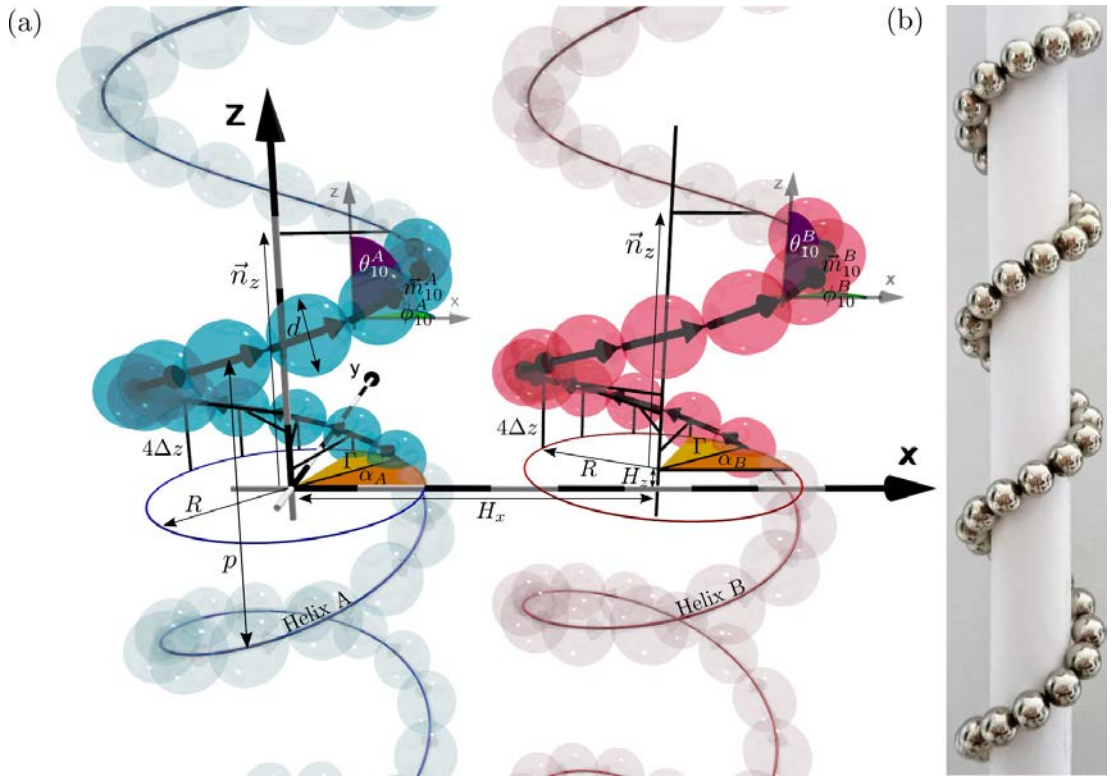

Figure 5.1: (a) Scheme of two interacting infinitely long and parallel helices A and B to the z-axis. For convenience, the axis of the helix A passes through the origin. The dark particles represent the spanning unit of the helices. The connecting helical backbone passing through the centers of the dipolar hard spheres for each helix is shown for clarity. The circular base of the corresponding embedding fictitious cylinder of radius R is depicted. For the sake of clarity, the polar and azimuthal angles (θ,ϕ) are only explicitly shown for two dipole moments labeled $\vec{m}_0^A$ and $\vec{m}_0^B$. (b) An illustrative helical chain made up of millimeter commercial magnetic beads sustained by a (solid) cylinder whose the diameter is about 1 cm.

chains, A and B, composed of dipolar hard spheres with a diameter $d = 1$, see Fig. 5.1(a). Each spherical particle $i^{A,B}$ embeds in its center a dipole moment $\vec{m}_i^{A,B}$ of identical magnitude $\mid \vec{m}_i^{A,B} \mid = m = 1$. The orientation of the dipole moment $\vec{m}_i^{A,B}$ is specified by the azimuthal and the polar angle $\phi_i^{A,B}$ and $\theta_i^{A,B}$, respectively. Hence $\vec{m}_i^{A,B} = (\cos\phi_i^{A,B}\sin\theta_i^{A,B}, \sin\phi_i^{A,B}\sin\theta_i^{A,B}, \cos\theta_i^{A,B})$. Both helical chains are geometrically identical and characterized by two (common) independent geometrical parameters, see Figure5.1(a):

- The radius R given by the distance between the axis of the helix and the centers of the particles.
- The distance Δz between the centers of two successive particles along the helix axis.

It is useful to define the azimuthal angular shift (or the helical twist) Γ between the centers of two successive particles, see Fig. 5.1(a). It is straightforward to show that $\Delta z = \sqrt{1 + 2R^2(\cos\Gamma - 1)}$ as a consequence of touching consecutive hard spheres. Each helical chain is generated by a unit cell containing N spherical particles periodically repeated (with a periodicity $\vec{n}_z$ where $n_z = |\vec{n}_z| = N\Delta z$ along the z-axis), see Fig. 5.1(a). The first particle of helix A is assumed to be at $\vec{r}_0^{\,A} = (x_0^A, y_0^A, z_0^A) = (R\cos(\alpha_A), R\sin(\alpha_A), 0)$ where α_A denotes the angle between $\vec{r}_0^{\,A}$ and the x-axis as sketched on Fig. 5.1(a). The Cartesian coordinates of the remaining $(N-1)$ particles read:

$$\begin{aligned} x_i^A &= R\left[\cos(i\Gamma)\cos(\alpha_A) - \sin(i\Gamma)\sin(\alpha_A)\right] \\ y_i^A &= R\left[\cos(i\Gamma)\sin(\alpha_A) + \sin(i\Gamma)\cos(\alpha_A)\right] \\ z_i^A &= i\Delta z. \end{aligned} \tag{5.1}$$

Similarly, the Cartesian coordinates of the particles belonging to helix B read (see also Fig. 5.1(a)):

$$\begin{aligned} x_i^B &= H_x + R\left[\cos(i\Gamma)\cos(\alpha_B) - \sin(i\Gamma)\sin(\alpha_B)\right] \\ y_i^B &= R\left[i\cos(\Gamma)\sin(\alpha_B) + \sin(i\Gamma)\cos(\alpha_B)\right] \\ z_i^B &= H_z + i\Delta z. \end{aligned} \tag{5.2}$$

The separation H_x is the distance between the helices axes and H_z ($\leq \Delta z$) is the relative shift between the helical chains along the z-axis, see Fig. 5.1(a). To ensure the periodicity of each helix along the z-axis, the helical twist is subject to the

condition $\Gamma = \frac{K}{N}2\pi$ where $K \in \mathbb{N}$ is the number of turns of the helix around its axis within the unit cell. Note that in Fig. 5.1(a), $K = 1$.

In order to quantify the compactness of the helical chains, it is useful to introduce the pitch p of the backbone of the helical chains given by:

$$p = \frac{n_z}{K}. \tag{5.3}$$

5.2.2 Dipole-dipole interaction

For a unit cell containing $2N$ dipolar particles located at $\vec{r}_0^A, r_0^B, ..., \vec{r}_N^A, \vec{r}_N^B$, the dipolar energy per unit cell, U_{cell}, can be written as

$$U_{\text{cell}} = U_{\text{self}}^A + U_{\text{self}}^B + U_{\text{cross}}^{AB}. \tag{5.4}$$

U_{self}^A and U_{self}^B in Eq. (5.4) correspond to the cohesive energy of the helical chains A and B, respectively, and read:

$$\begin{aligned} U_{\text{self}}^{A,B} &= \frac{1}{2}\sum_{i,j}^{N}{}' \sum_{\vec{\mathcal{N}}_z} \frac{C}{|\vec{r}_{ij}^{A,B} + \vec{\mathcal{N}}_z|^3}\Bigg[\vec{m}_i^{A,B}\cdot\vec{m}_j^{A,B} \\ &\quad -3\frac{\vec{m}_i^{A,B}\cdot(\vec{r}_{ij}^{A,B}+\vec{\mathcal{N}}_z)\vec{m}_j^{A,B}\cdot(\vec{r}_{ij}^{A,B}+\vec{\mathcal{N}}_z)}{|\vec{r}_{ij}^{A,B}+\vec{\mathcal{N}}_z|^2}\Bigg]. \end{aligned} \tag{5.5}$$

U_{cross}^{AB} in Eq. (5.4) stands for the cross-energy between the two helical chains A and B, and reads:

$$\begin{aligned} U_{\text{cross}}^{AB} &= \frac{1}{2}\sum_{i,j}^{N} \sum_{\vec{\mathcal{N}}_z} \frac{C}{|\vec{r}_{ij}^{AB} + \vec{\mathcal{N}}_z|^3}\Bigg[\vec{m}_i^{A}\cdot\vec{m}_j^{B} \\ &\quad -3\frac{\vec{m}_i^{A}\cdot(\vec{r}_{ij}^{AB}+\vec{\mathcal{N}}_z)\vec{m}_j^{B}\cdot(\vec{r}_{ij}^{AB}+\vec{\mathcal{N}}_z)}{|\vec{r}_{ij}^{AB}+\vec{\mathcal{N}}_z|^2}\Bigg], \end{aligned} \tag{5.6}$$

where $\vec{r}_{ij}^{AB} = \vec{r}_i^A - \vec{r}_j^B$ and $\vec{\mathcal{N}}_z = \mathcal{N}_z\vec{n}_z$ designates the Bravais vector along the z-axis ($\vec{n}_z$ being the spanning vector) with integer component $\mathcal{N}_z$ ranging from $-\infty$ to $+\infty$. The prime in Eq. (5.5) indicates that, when $\vec{\mathcal{N}}_z = 0$, i must be different from j. In order to overcome the slow convergence in Eq. (5.4), an efficient Lekner-like sum technique for systems with periodicity in one direction was used [112]. The energy scale is set by $U_{\uparrow\uparrow}$, see Eq. (2.10). Thereby, the interaction potential energy

per particle, u, is merely given by $u = \frac{1}{2N}\frac{U_{\text{cell}}}{U_{\uparrow\uparrow}}$.

5.2.3 Energy minimization

At prescribed separation distance H_x, a system of two helices depends on $(4N+3)$ variables: The $4N$ variables stems from the two angular parameters (θ,ϕ) per dipolar sphere for the unit vector defining the direction of the dipole moment. The three other variables are the longitudinal shift H_z of the helix B and the angles of rotation α_A and α_B. To compute the energy minimum, we perform a minimization of u using a constrained minimization algorithm called SLSQP [62], see Section 2.3.2. Note that upon searching the global minimum, typically 10^3-10^4 starting random configurations were considered.

5.3 Dipolar linear chains

5.3.1 Single linear chain

A (straight) linear chain can be envisioned as a limit of a helical chain in two manners: (i) Either with a diverging pitch ($p \to \infty$ at fixed R) or (ii) in the limit of one particle per turn ($N = 1$). Thus, this relevant limit of the straight linear chain should be insightful to understand (non trivial) helical chains with arbitrary pitch. In this respect, a good starting point is the detailed study of the magnetic field produced by a dipolar linear chain. Figure 5.2(a) provides a two-dimensional view of the landscape of the intensity of the produced magnetic field together with its field lines. It clearly arises that high field values are strongly localized around the poles of the particles, see Fig. 5.2(a). This feature is also true for a single isolated sphere, see Fig. 5.2(b). However the magnetic field distribution becomes strongly anisotropic for a linear dipolar chain, compare Fig. 5.2(a) and (b). More specifically, the magnetic field around the poles is increased compared to the single dipolar particle case as it should be, see Fig. 5.2. Nonetheless, this zone is not relevant for the inter-chain interaction due to excluded volume effect. On the other hand, in the accessible area compatible with steric effect, the magnetic field becomes strongly screened [38, 63]. Consequently, the inter-chain interaction is in general limited to weak dipolar couplings. As far as field lines are concerned, a flattening is observed compared to the single dipolar hard sphere case, see Fig. 5.2. The z-component of the magnetic field along the chain axis, B_z, contains relevant

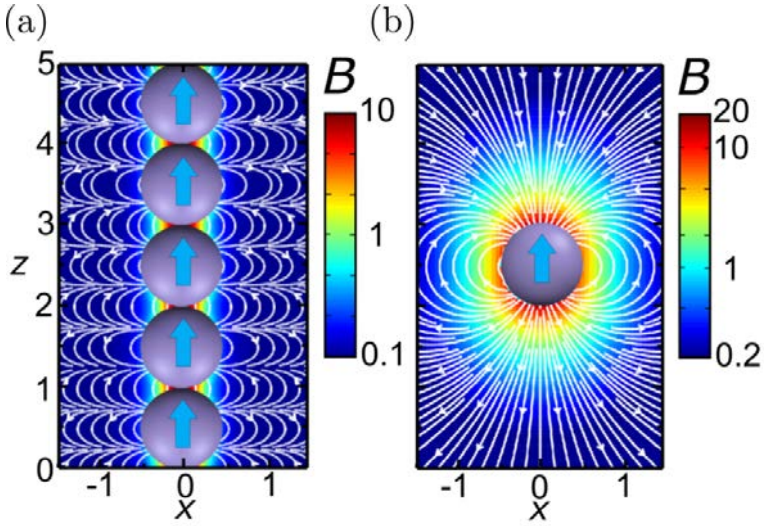

Figure 5.2: A two-dimensional view of the landscape of the magnetic field intensity $B = \|\vec{B}\|$ (in units of $\frac{U_{\uparrow\uparrow}}{m}$) originating from (a) a linear chain [see Eq. (2.2)] and (b) an isolated magnetic sphere [see Eq. (2.8)]. It is a representative portion of the infinite system in (a). The white lines depict the magnetic field lines and the arrows give the direction of $\vec{B}$.

information about the ground state of two interacting chains at prescribed relative shift. Typically two scenarios emerge related to the Zeeman energy term $(-m_z B_z)$:

- When B_z is positive, a parallel chain will have its dipole moments parallel to those of the chain at $x = 0$, see Fig. 5.2(a). This configuration will be referred to as a ferromagnetic state. This situation will occur when the two parallel chains are out-of-registry, see Fig. 5.2(a).

- When B_z is negative, a parallel chain will have its dipole moments antiparallel to those of the chain at $x = 0$, see Fig. 5.2(a). This configuration will be referred to as an antiferromagnetic state. This situation will occur when the two parallel chains are in- (or nearly in-) registry, see Fig. 5.2(a).

5.3.2 Interaction of two linear chains

Besides of its experimental relevance [9, 57, 74, 75, 94, 146, 147], the two chain case scenario is also of fundamental importance [38, 45, 63, 95, 106, 116, 148, 149]. In the context of interacting dipolar helical chains, it constitutes an important and instructive limiting case that we are going to address in this part. The phase diagram

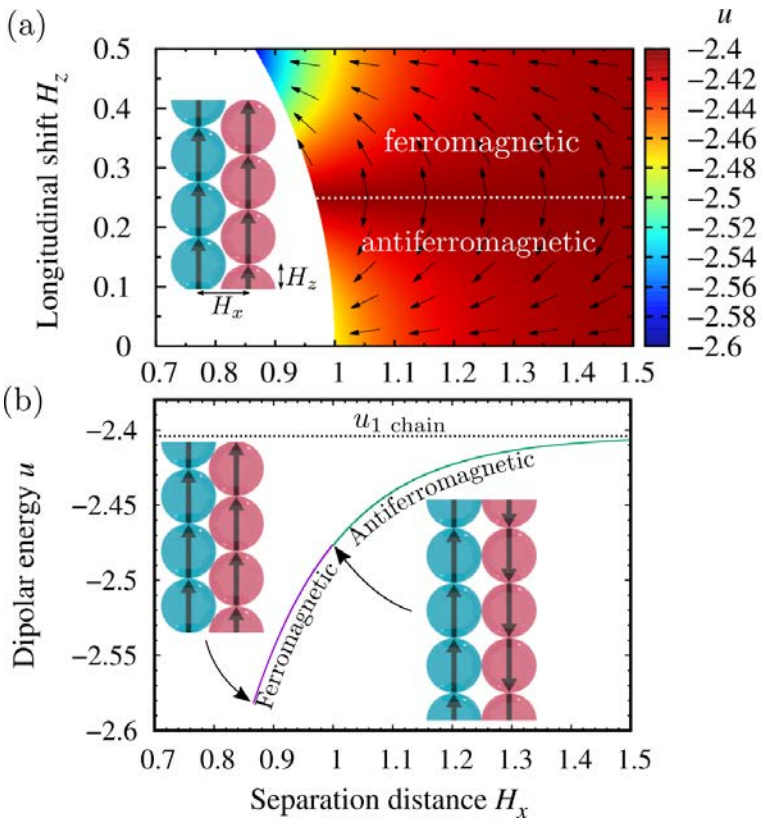

Figure 5.3: (a) Minimum energy landscape of the dipolar energy u as a function of the longitudinal shift H_z and the inter-chain separation distance H_x. Here, the origin $(0, 0)$ coincides with the center of a constitutive dipolar hard sphere. The white area around the origin corresponds to the forbidden overlapping zone. An illustration of the system is also provided as an inset. The arrows indicate the direction of the magnetic force per particle [see Eq. (2.7)]. The ferromagnetic and antiferromagnetic states are delineated by a white dashed line. (b) The energy profile of the ground states u as a function of H_x. The ground states at $H_x = \sqrt{3}/2$ (ferromagnetic) and $H_x = 1.0$ (antiferromagnetic) are sketched. The energy of a single linear chain is indicated with the dashed line.

(ferromagnetic vs antiferromagnetic state) in the (H_x, H_z)-plane, accompanied with the energy landscape, is presented in Fig. 5.3(a). The region of lowest energies corresponds to the interstice (around $H_x = 0.5$) left between two touching spheres (of a given chain) corresponding to a ferromagnetic state, see Fig. 5.3(a). The overall ground state occurs when two chains appear in the zipper configuration (with $H_x = \sqrt{3}/2$, $H_z = 0.5$, $u = u_{2\text{ chains}} = -2.582$) as expected [38, 95]. Upon sliding the chains from this overall ground state down to the point $(H_x = 1.0, H_z = 0.0)$ where chains are in contact and in-registry, the potential energy u exhibits a remarkable non-monotonic behavior, see Fig. 5.3(a). Interestingly the ferromagnetic/antiferromagnetic transition occurs at $H_z = 0.25$ in agreement with the magnetic field lines already discussed, see also Fig. 5.2(a). This feature holds for any allowed value of H_x including $H_x \to \infty$. The force fields in Fig. 5.3(a) indicate two stable ground states with touching chains: The ferromagnetic state with chains in-registry and the antiferromagnetic state with chains out-of-registry. The energy profile of the ground states as a function of the inter-chain distance H_x only is reported in Fig. 5.3(b). It is to say that at prescribed H_x, the special value of H_z leading to the lowest energy is selected. The ferromagnetic state is found to be energetically favorable for $H_x \lesssim 1$ [1] with chains out-of-registry ($H_z = 0.5$), see inset Fig. 5.3(b). Then, the antiferromagnetic state emerges when $H_x \gtrsim 1.0$ with chains in-registry ($H_z = 0$), see also illustration in Fig. 5.3(b).

5.4 Dipolar zigzag chains

5.4.1 Single zigzag chain

The zigzag chain motif is ubiquitous and highly relevant in condensed matter physics [150, 151, 152, 153, 154]. Geometrically speaking, the zigzag chain can be seen either as the association of two discontinuous linear chains in contact or as a special helical chain with two beads per turn (i.e., $N = 2$). In our formalism, the coordinates of the two constitutive particles are given by Eq. (5.1). We define the zigzag chain angular parameter β as $R = \dfrac{\sin\beta}{2}$, see also illustration in Fig. 5.4. Upon varying β

[1] A meticulous analysis of the data reveals that the transition between the ferromagnetic and antiferromagnetic states occurs at about $H_x = H_x^* = 0.9997$ which is surprisingly not exactly unity. At H_x^* a strong discontinuous transition occurs: For $H_x^* = H_x^{*-}$, the ferromagnetic state is characterized by a longitudinal shift $H_z = 0.5$ whereas for $H_x^* = H_x^{*+}$, the antiferromagnetic state emerges with $H_z = 0.022$. This transitions is followed by a continuous (relative) sliding of the two touching chains from H_x^{*+} to unity.

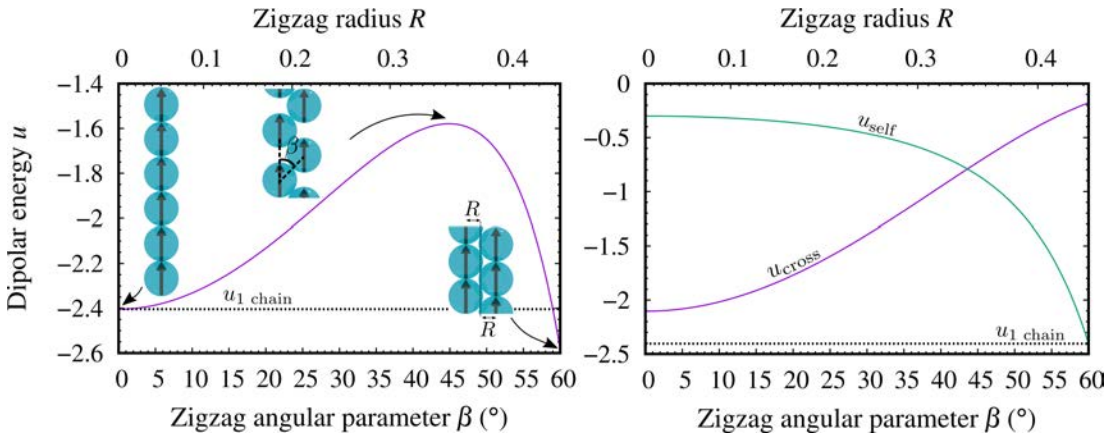

Figure 5.4: (Left panel) Minimum energy u for a single zigzag chain as a function of the angular parameter β corresponding to a zigzag chain radius R, see the insets. Three configurations are displayed for $\beta = 0.0°$ (linear chain), $44.4°$ (ordinary zigzag chain) and $\beta = 60.0°$ (ribbon), corresponding respectively to $R = 0.0, 0.35$ and $R = \sqrt{3}/4 \simeq 0.433$. (Right panel) The the self-energy contribution u_{self} and the cross-energy contribution u_{cross} as a function of the angular parameter β.

from 0° to 60° ($0 \leq R \lesssim 0.43$), the zigzag chain structure evolves continuously from a chain to a ribbon, see also Fig. 5.4. The ground state energy profile of the system as a function of β (or equivalently R) is presented in Fig. 5.4. As a general rule, it is found that the dipole moments always follow the z-axis (i.e. zigzag chain axis). The energy profile in Fig. 5.4 brings to light that almost all the various forms of zigzag chains are energetically worse than the straight chain. The energy limit of a single linear chain ($u = u_{1\text{ chain}} = -2.404$) is only beaten by a zigzag chain whose angular parameter is $\beta \gtrsim 59°$ (i.e., $R \gtrsim 0.429$), see Fig. 5.4. The non-monotonic shape of the energy profile, see Fig. 5.4, is the result of a competition between (i) the interaction of particles belonging to the same (discontinuous) chains (i.e. the self-energy contribution) and (ii) the interaction between inter-chain particles (i.e. the cross-energy contribution). The self-energy contribution diminishes the value of u with increasing β whereas the cross-energy increases the value of u. In details, for $\beta \lesssim 45°$, the self-energy variation is beaten by the cross-energy leading to an increase of the potential energy u, see Fig. 5.4. Thereby, the straight linear chain ($\beta, R = 0.0$) is stable against compression which is reminiscent of a spring at rest. The trend is inverted when $\beta \gtrsim 45°$.

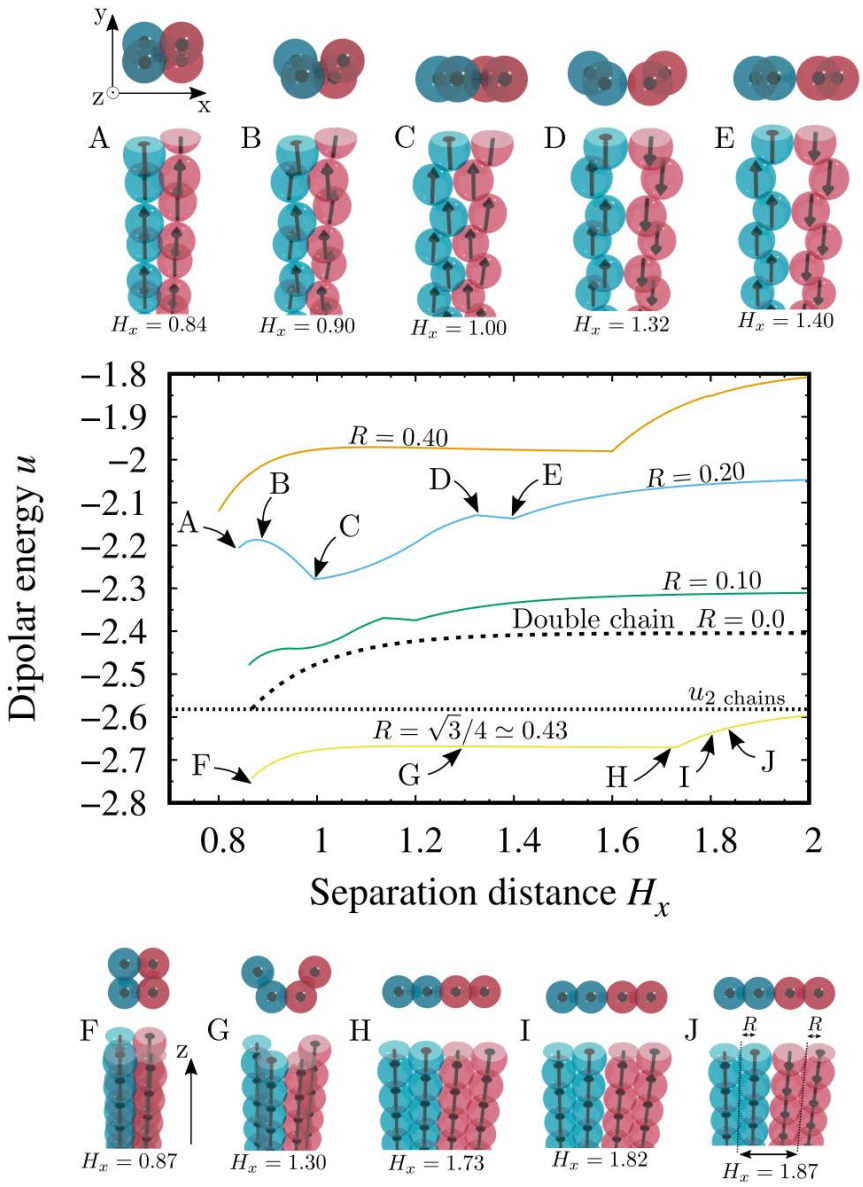

Figure 5.5: Energy profiles u as a function of the inter-zigzag chain distance H_x. Four relevant cases characterized by $R = 0.10, 0.20, 0.40$ and $R = \sqrt{3}/4 \simeq 0.43$ ($\beta = 11.5°, 23.6°, 53.1°$ and $\beta = 60.0°$) are displayed. The dashed line represents the limit case of the straight double chain ($R, \beta = 0.0$). Snapshots of the typical (labeled) ground states are depicted with a top- and perspective-view.

5.4.2 Interaction of two zigzag chains

We now come to the case of two interacting zigzag chains. An interesting experimental realization of this problem is provided by the assembly of magnetic Janus particles [147] or colloids with magnetic patches [155]. The total energy of interaction per particle u as a function of the inter-zigzag chain distance H_x, for various zigzag chain shapes with radius $R = 0.10, 0.20, 0.40$ and $R = \sqrt{3}/4 \simeq 0.43$, are displayed in Fig. 5.5. As a general feature, the energies stemming from zigzag chains with $R \lesssim 0.4$ are always higher than those of two interacting linear chains, see Fig. 5.5. This observation is highly analogous with the behavior of the energy profile of the single zigzag chain previously discussed, see Fig. 5.5. It turns out that for interacting zigzag chains, the dipole moments do not necessarily (perfectly) follow the zigzag chain axis, see snapshots in Figure 5.5. To discuss in more details the evolution of the microstructures, we start with the more extended zigzag chains characterized by small angular parameter β (here $\beta = 11.5°$ and $\beta = 23.6°$ or $R = 0.10$ and $R = 0.20$), see Fig. 5.5. Both zigzag chain pairs exhibit a similar microstructural evolution as a function of the inter-zigzag chain separation distance H_x. The same holds for the shape of the corresponding energy profiles (except for the position of the overall ground state), see Fig. 5.5. At the distance of closest approach $H_x \simeq 0.84$ for $R = 0.20$, the two zigzag chains interlock by adopting a rectangular cross-section in a ferromagnetic state as sketched in Fig. 5.5. This structure has the highest degree of contact between the zigzag chains at this smallest separation distance [2]. By slightly separating the zigzag chains from each other, the degree of contact between zigzag chains decreases where a remarkable V-shape of the cross-section sets in. The related dipole moments distribution becomes non uniform, see Fig. 5.5 for $H_x \simeq 0.90$. There is also a non trivial strong correlation between inter-zigzag chain dipole moments, see snapshots in Fig. 5.5 for $H_x \simeq 0.90$. By further separating zigzag chains from each other, they become coplanar and still remain interlocked in the gaps, see Fig. 5.5 for $H_x \simeq 1.00$ or $H_x \simeq 1.25$. The non uniform character of the dipole moments distribution persists as well as the cross zigzag chain dipole moment correlations, see Fig. 5.5 for $H_x \simeq 1.00$ or $H_x \simeq 1.25$. The global minimum observed for $H_x \simeq 1.00$ is related to an optimal interlocking of the two zigzag chains, see snapshot in Fig. 5.5. In a more general fashion, the highly non trivial monotonic energy profile is a result of a delicate interplay between

[2] This special (high density) state at closest approach is not always the overall ground state at prescribed zigzag chain shape (i.e. at given R or β).

steric effect and dipolar correlations. The local maximum occurring at $H_x \simeq 1.32$ correspond to a reversal of the dipole moment of one zigzag chain, leading to an antiferromagnetic state, see Fig. 5.5. Concomitantly there is a re-entrance of the V-shape of the cross-section and the zigzag chains are now in-registry. Then, there is a little decrease of the energy until $H_x \simeq 1.40$, see Fig. 5.5. This local minimum at $H_x \simeq 1.40$ corresponds geometrically to the contact of the two embedding cylinders, see snapshot in Fig. 5.5. Note that a re-entrance of the ribbon structure sets in. For $H_x \gtrsim 1.40$ the energy increases monotonically where the antiferromagnetic state persists.

The other typical form of the energy profile is reported for dense zigzag chains with $R = 0.40$ and $R \simeq 0.43$, see Fig. 5.5. The strong energy shift between $R = 0.40$ and $R \simeq 0.43$, see Fig. 5.5, merely reflects the high self-energy difference, see also Fig. 5.4. It is worth to mention that in this regime of high compaction of zigzag chains, the energy profile is in general much less complicated then those encountered at low compaction (here $R = 0.10$ and $R = 0.20$). The overall ground state coincides with the distance of closest approach (here $H_x \simeq 0.87$ for $R \simeq 0.43$) between the zigzag chains, see Fig. 5.5. There, the cross section is square and the zigzag chains are perfectly interlocked in the gaps, see snapshot for $H_x \simeq 0.87$ in Fig. 5.5. Upon increasing the inter-zigzag chain separation distance H_x, a cross-section with the V-shape sets in until $H_x \simeq 1.73$, see also snapshot $H_x \simeq 1.30$ in Fig. 5.5. The latter corresponds to a ribbon made up of four perfectly interlocking chains. Thereby, a plateau emerges for a large separation window ranging from $H_x \simeq 1.00$ to $H_x \simeq 1.73$. For $H_x \gtrsim 1.73$, the energy increases monotonically with H_x where the two zigzag chains remain coplanar, see Fig. 5.5. The ferromagnetic/antiferromagnetic transition occurs at $H_x \simeq 1.87$ where the zigzag chains get in-registry.

The magnetic phase diagram (ferromagnetic vs antiferromagnetic) in the plane (R, H_x) is depicted in Fig. 5.6. An insightful geometrical picture is provided by the contact of two embedding cylinders, see illustrative snapshot in Fig. 5.6, leading to the simple law $H_x = H_x^{(\mathrm{contact})} = 2R + 1$. Indeed, the numerically calculated (ferromagnetic/antiferromagnetic) transition line (see square symbols in Fig. 5.6) is in rather good agreement with the simple geometrical idea of touching embedding cylinders, see Fig. 5.6. As a matter of fact, an excellent agreement with the geometrical model is found in two limits: (i) the chain limit (with $R \lesssim 0.05$) and (ii) in the high packing regime (with $R \gtrsim 0.30$), see Fig. 5.6.

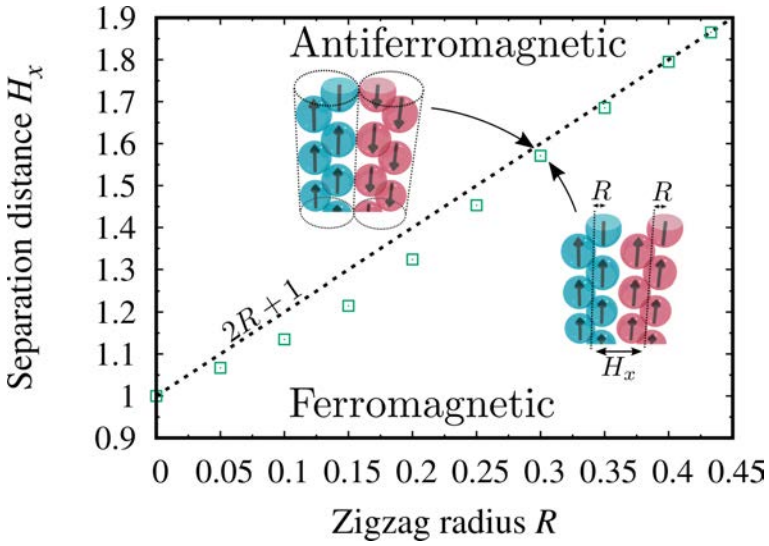

Figure 5.6: Phase diagram (ferromagnetic vs antiferromagnetic state) in the (R,H_x)-plane. The square symbols delimit the magnetic phase boundary. The dashed line ($H_x = 2R + 1$) represents the limit geometrical situation where the two cylinders embedding the zigzag chains are in contact (see inset) or cease interlocking. Two illustrative phases at $R = 0.30$ ($\beta = 36.9°$) are shown in inset.

5.5 Dipolar helical chains

5.5.1 Single helical chain

The understanding of the complex interaction between two helical dipolar chains necessitates beforehand to elucidate the ground state of of a single dipolar helical chain. The behavior of the minimum energy profile u as a function of the pitch p is sketched in Fig. 5.7(a). As already advocated in Ref. [119], a remarkable non-monotonic behavior is observed, see Fig. 5.7(a). As a general rule, the linear chain is stable against undulation in the extended helical chain regime. It is only at sufficiently high packing (or equivalently sufficiently small pitch) that energy is gained upon compacting the helical chain. Notice there the strong resemblance with the energy profile of a single zigzag chain, compare Fig. 5.4 and Fig. 5.7(a). We have also monitored the magnetic order parameter m_z [3]. Interestingly a vivid non-monotonic behavior is also reported, see Fig. 5.7(b). At weak compaction (in the linear chain limit) m_z is about unity. At high compaction m_z recovers high values up to $m_z \simeq 0.84$. Between this two limits, m_z can assume values as low

[3]In the case of a single dipolar chain each constitutive particle possesses the same projected dipole moment along the z-axis.

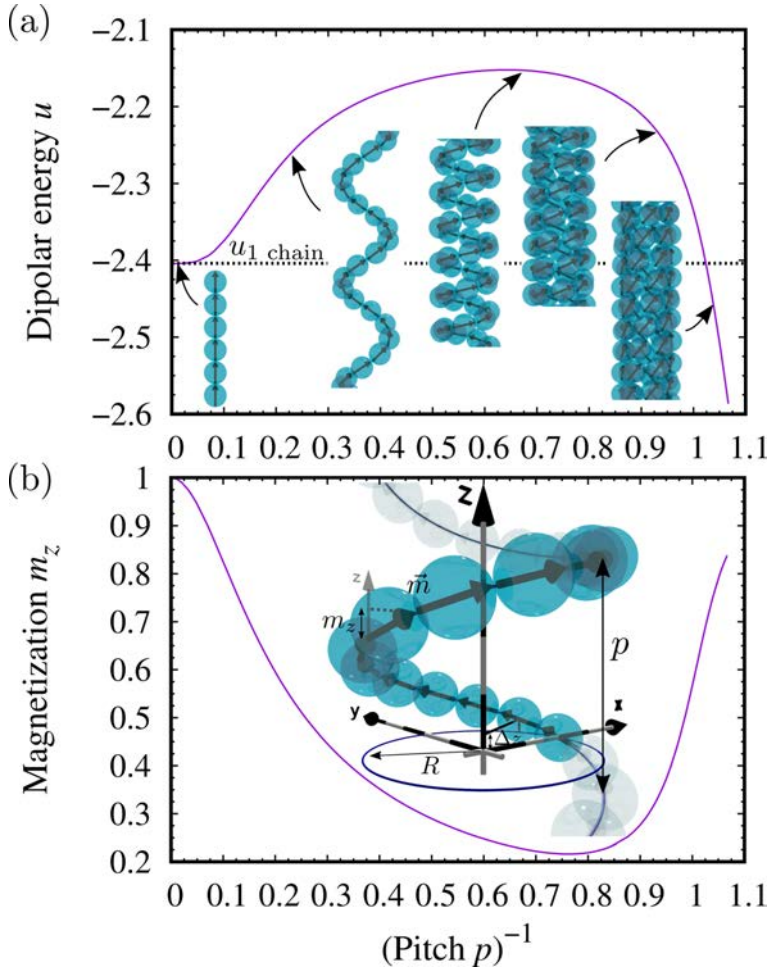

Figure 5.7: (a) Minimum energy u as a function of the pitch p for a single dipolar helical chain. Microstructures of the ground states are depicted for different values of p in inset. The radius of the helix is fixed at $R = 1.105$. (b) The z-component of the dipole moment m_z as a function of p. An illustration of m_z is sketched as an inset.

as $m_z \simeq 0.22$, reminiscent of tubular structures with stacked rings [41]. When the pitch is not too small ($p \gtrsim 1.3$ or $p^{-1} \lesssim 0.8$), the dipole moment $\vec{m}$ is tangential to the helical backbone, see also snapshots in Fig. 5.7(a), so that $m_z = \Delta z$.

5.5.2 Interaction of two helical chains

5.5.2.1 Effect of pitch length

Concentric double helical chains Dipolar linear- and zigzag-chains having been clarified, we now address the more complex situation of two interacting (more generic) helical chains. In this part, we discuss the influence of the pitch p on the interaction of two helical dipolar chains. We first look at the ground states consisting of concentric helical chains (i.e., $H_x = 0$). The corresponding energy profile u as a function of the pitch p is reported in Fig. 5.8(a). The shape of the profile is highly similar to that encountered in the case of the single helical chain, compare Fig. 5.7(a) with Fig. 5.8(a). At very high pitch the ground state corresponds to a ribbon of two chains (with $u = u_{2\ \text{chains}}$) as it should be, see Figure 5.8(a). In the other relevant limit of small pitch, the energy of the two chain-ribbon is more or less recovered, see Fig. 5.8(a). Depending of the choice of R, lower or higher energies than $u_{2\ \text{chains}}$ can be achieved.

We introduce the magnetic order parameter $< m_z >$ defined as:

$$< m_z^{A,B} >= \frac{1}{N} \sum_{i=0}^{N-1} m_{z,i}^{A,B}, \tag{5.7}$$

which will be referred to as the magnetization. Its profile as a function of the pitch p is displayed in Fig. 5.8(b). In agreement with the behavior of the energy profile, a similar shape is found for the magnetization $< m_z >$ when compared to the single helical chain case, see Fig. 5.7(b) and Fig. 5.8(b). It is to say that two concentric dipolar helical chains behave like a helical ribbon.

Separated helical chains Typical profiles of dipolar energy per particle u as a function of H_x are sketched in Fig. 5.9. In the large pitch regime (i.e., low compression regime), see Fig. 5.9 for $p \geq 7.3$ (or $N \geq 10$), a clear scenario emerges. The overall ground states at prescribed pitch correspond to two concentric helical chains. A remarkable common feature is the *unwinding* (or unentanglement) transition that sets in upon separating the helical chains from each other, see cor-

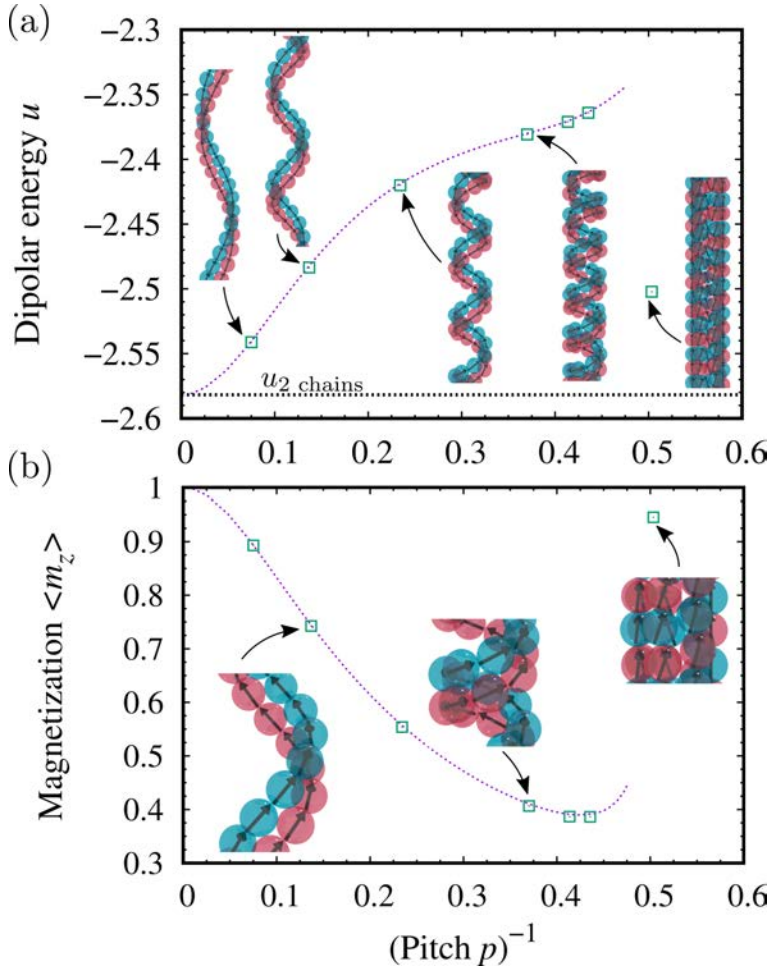

Figure 5.8: (a) Minimum energy u as a function of the pitch p for two concentric helical chains. The microstructures of the ground states are depicted in insets for different values of p. (b) The magnetization $< m_z >$ as a function of p. The dotted line stems from a minimization involving a single common m_z (or equivalently $\cos\theta$) value for all beads. Typical local dipole arrangements are displayed.

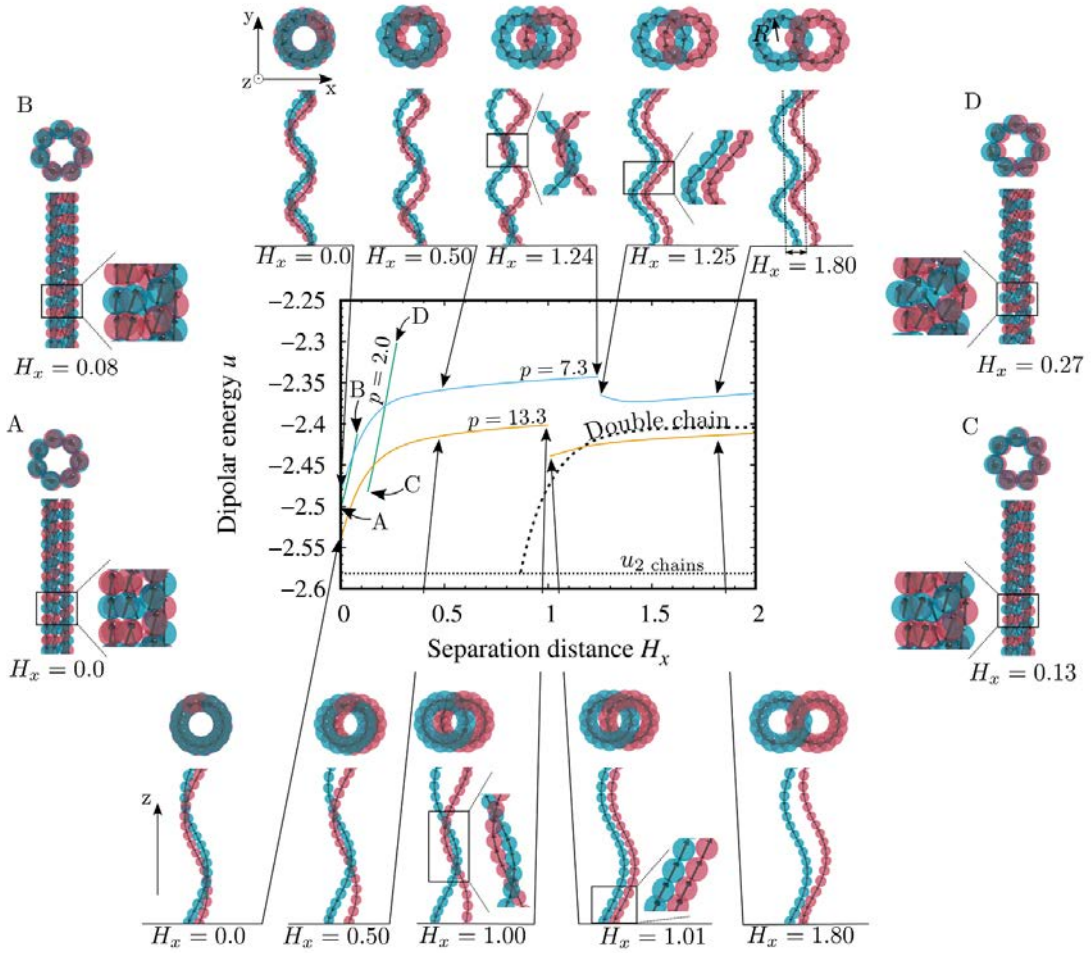

Figure 5.9: Minimum energy u as a function of the separation distance H_x at prescribed $R = 1.105$ for different values of the pitch p. The microstructural transformations as a function of H_x are illustrated (side and top view) on the upper panel for $p = 7.3$ ($N = 10$) and the lower panel for $p = 13.3$ ($N = 15$). Typical local dipole moment arrangements are highlighted. For the sake of clarity, the labeled microstructures A, B, C and D associated to $p = 2.0$ ($N = 7$) are deported on the sides.

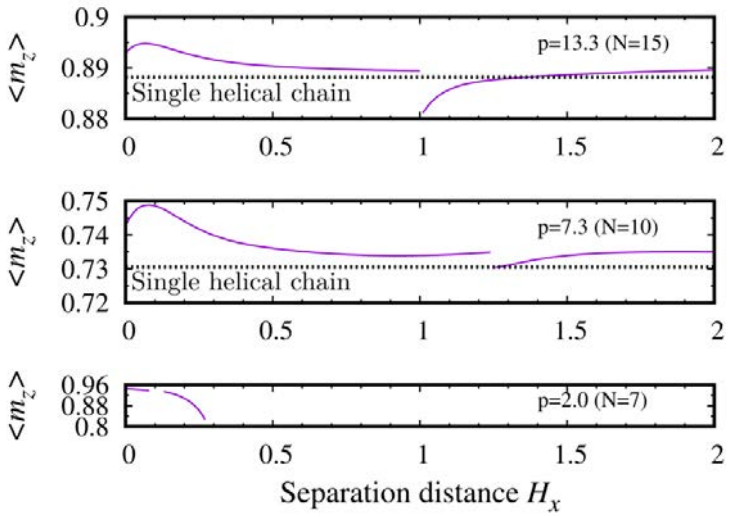

Figure 5.10: The magnetization $\langle m_z \rangle$ as a function of the separation distance H_x for $p = 13.3$ ($N = 15$), $p = 7.3$ ($N = 10$) and $p = 2.0$ ($N = 7$). The dashed line indicates the magnetization value for a single helical chain for $p = 7.3$ and $p = 13.3$. For the sake of clarity, the magnetization value ($\langle m_z \rangle = 0.29$) for the single helical chain case is not reported for $p = 2.0$.

responding snapshots in Fig. 5.9. This transition is concomitantly accompanied by a strong discontinuous energy drop, see Fig. 5.9. The double straight (linear) chain structure is asymptotically reached for a diverging pitch ($p \to \infty$) when $H_x = 0.0$ and $H_x = \sqrt{3}/2 \simeq 0.87$, see Fig. 5.9. In that limit situation ($p \gg 1$), the unentaglement transition occurs at $H_x \simeq 0.87$, see Fig. 5.9.

In the regime of small pitch (here $p = 2.0$ corresponding to a strong helix compression, see Fig. 5.9), severe constraints originating from strong excluded volume effects emerge leading to a edgy discontinuous energy profile, see Fig. 5.9. The overall ground state there is still described by two concentric helical chains. For $H_x \in [0.0, 0.08]$, there is a steep increase of the energy, see Fig. 5.9. Steric effects lead to a forbidden zone for $H_x \in [0.08, 0.13]$. Then, for $H_x \in [0.13, 0.27]$ a similar steep increase of the energy occurs which is followed by a wide forbidden zone going beyond $H_x \simeq 2.0$, see Fig. 5.9.

As far as the magnetization $\langle m_z \rangle$ is concerned, in general, it is identical on each chain leading to a ferromagnetic state (i.e. $\langle m_z^A \rangle = \langle m_z^B \rangle$), see Fig. 5.10 [4]. In the regime of large pitch ($p \geq 7.3$), the value of $\langle m_z \rangle$ remains rather constant during

[4]We have found in some instances that antiferromagnetic states (i.e., opposite magnetization of the two chains) emerge for tiny separation distance window, not shown in Fig. 5.9 and Fig. 5.10.

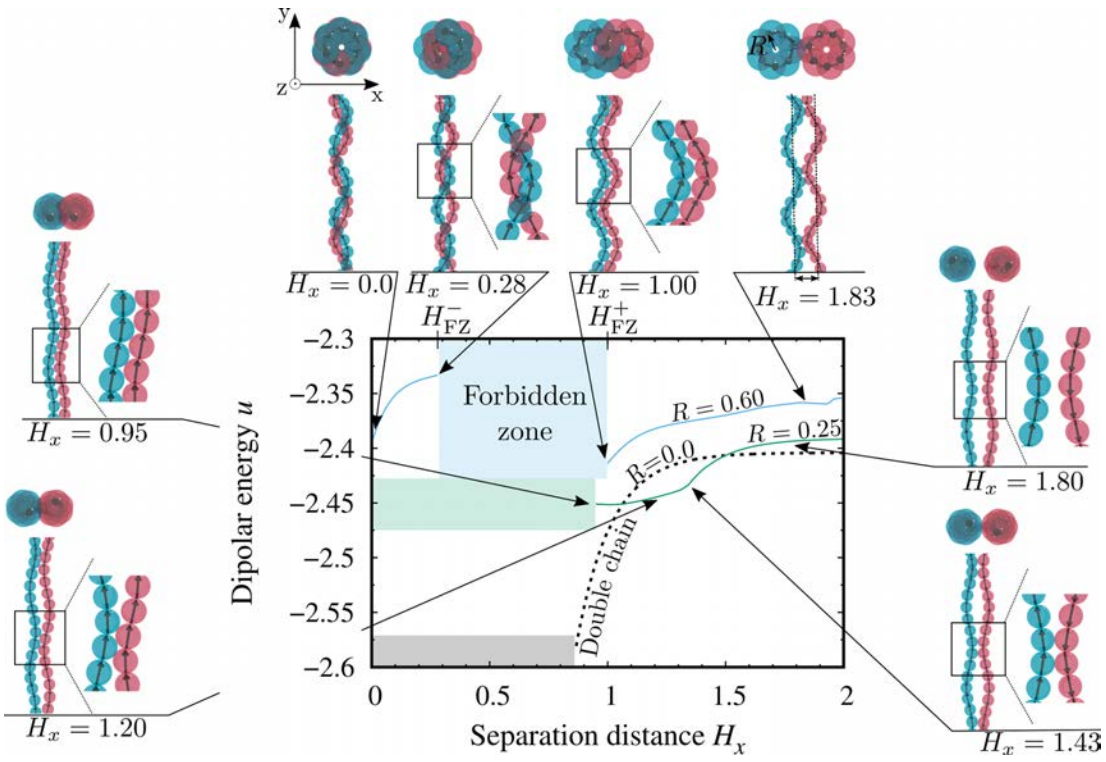

Figure 5.11: Minimum energy u as a function of the separation distance H_x (with $N = 7$) for different values of the helix radius $R = 0.0$ (double chain), 0.25 and $R = 0.60$. The microstructures of the helical chains are illustrated (side and top views) on the top for $R = 0.60$ and on the sides for $R = 0.25$. The three corresponding forbidden zones are shown and the lower limit (H_{FZ}^-) and the upper limit (H_{FZ}^+) are indicated for $R = 0.60$. Typical local dipole moment arrangements are highlighted.

the whole process of the two helical chain separation, see Fig. 5.10. In contrast, in the small pitch regime ($p \leq 2.0$), the magnetization $\langle m_z \rangle$ varies significantly and does not reflect that stemming from the single helical chain case (here $\langle m_z \rangle = 0.29$), see Fig. 5.10. This effect is attributed to the strong correlation between the two interlocking helical chains. Upon separating the helical chains from each other, $\langle m_z \rangle$ drops considerably over a rather short distance interval, see Fig. 5.10.

5.5.2.2 Effect of small helix radius

It is expected that for a small enough helix radius, concentric helical chains are forbidden due to steric effects. Hence, the present purpose is to look at the effect of small helix radius on the ground states of interacting dipolar helical chains. The energy profiles of u as a function of the separation distance H_x for several values of the helix radius R are depicted in Fig. 5.11. For $R = 0.60$, it is found to that

concentric helical chains are still allowed (with $u = -2.396$). Upon increasing the separation distance H_x between the helical chains ($H_x \in [0.0, 0.28]$), the energy increases and the helical chains are entangled there, see Fig. 5.11. The unwinding transition occurring at $H_x \simeq 1.0$ is preceded by a wide forbidden zone ($H_x \in [H_{\rm FZ}^-, H_{\rm FZ}^+]$ with $H_{\rm FZ}^- \simeq 0.28$ and $H_{\rm FZ}^+ \simeq 1.0$) resulting from steric effects, see Fig. 5.11. It is precisely at this unwinding transition that the overall ground state emerges (with $u = -2.414$), see Fig. 5.11. Notice that there is a short separation distance window $H_x \in [1.83, 1.95]$ where the antiferromagnetic state emerges, see Fig. 5.11.

Upon decreasing R until about $R \simeq 0.5$, $H_{\rm FZ}^-$ decreases (and vanishes for $R \simeq 0.5$), meaning that the allowed zone of interwinding helices shrinks, see Fig. 5.11. Concomitantly, $H_{\rm FZ}^+$ decreases as well, meaning that the unwinding transition is shifted to lower separation distances. It turns out that the width of the forbidden zone depends on R in a non trivial manner. Below $R \simeq 0.50$, entangled helical chains are forbidden ($H_{\rm FZ}^-$). We have observed that for some values of R the overall ground state can be shifted to higher values of $H_x > H_{\rm FZ}^+$. An illustrative example with $R = 0.25$ is provided in Fig. 5.11 where $H_{\rm FZ}^+ \simeq 0.95$ and the overall ground state is $H_x \simeq 1.01$ [5]. When approaching the limit of vanishing helix radius ($R \to 0$), the double chain-ribbon case is reached asymptotically where $H_{\rm FZ}^+ = \sqrt{3}/2 \simeq 0.87$. Notice the ferromagnetic/ antiferromagnetic transition occurring at $H_x \simeq 1.43$ which has to be compared with the value of $H_x^{\rm contact} = 2R + 1 = 1.50$.

5.6 Concluding remarks

To summarize, we have investigated the ground states of two interacting dipolar helical chains going from straight linear chain to helical chains via zigzag-like conformations. This geometrical pathway to the complex dipolar helical edifices has considerably helped us to rationalize their highly challenging interaction.

The straight linear chain case permits a precise quantitative analysis of the intricate interplay between excluded volume effect and dipolar correlations. In particular, the evolution of the ground state as a function of the inter-chain separation distance H_x has been addressed. There, a remarkable ferromagnetic/antiferromagnetic transition (i.e., chains possessing equal/opposite dipole moments) sets in around

[5] This observation is consistent with the behavior of interacting zigzag chains, see Fig. 5.5 with $R = 0.20$.

$H_x \simeq 1.0$. All these results concerning interacting linear chains can be rationalized with the knowledge of the magnetic field lines associated to the single chain. When dealing with interacting zigzag chains, an analogous behavior to the linear chain situation is found. For a single zigzag chain, it turns out that it is nearly always energetically beaten by the straight chain. It is only in the two-chain-ribbon regime (two touching chains out-of-registry) that the zigzag chain becomes energetically favorable. In a similar fashion, the potential energy becomes lower than that of the single ribbon only for highly compress zigzag chains (i.e. in the ribbon regime).

Given the strong one-dimensional character of helices, magnetic interactions are strongly screened and become negligible when dipolar helical chains are not interlocked. Typically, when the helix radius is large enough the overall ground state consists of two concentric helical chains winding around each other. Upon separation, a local energy minimum sets in where the helical chains are no longer entangled. At prescribed helix radius R, the overall ground state energy as a function of the pitch resembles also that found with a single helical chain. The same applies to the magnetization $\langle m_z \rangle$. The dipole moment distribution is essentially dictated by that found in an single (isolated) helical dipolar chain when the pitch is not too small. When the helix radius becomes small enough so that the helices can not wind around each other due to steric effects, then the ground state scenario is qualitatively affected. More specifically, the ground states consist of non-concentric and not entangled helical chains.

An interesting experimental realization of our system has been published very recently [156]. There, magnetic colloidal particles where dynamically shaked down by means of AC magnetic fields to achieve, among others, helical magnetic chains [156]. Our findings should shed some additional light on recent experimental studies highlighting the intriguing formation of multiturn helical superstructures with, for instance, magnetic colloids [137, 138] or Janus particles [139, 147, 157]. This work provides also possible hints about the role of dipolar interactions in the packing of α-helices [158] who are dipolar helical objects [159] too. Further interpretation and/or test of recent models [141, 160] and simulation data [140, 161, 162, 163] on closely related systems can also be accomplished thanks to this contribution.

Part II

Crystallization of dipolar particles

Chapter 6

Sedimentation of dipolar particles in a monolayer

This chapter covers a study on sedimentation of superparamagnetic particles combining experiment, theory and simulations. The main results were published in *Physical Review E* [164].

Contents

6.1 Introduction 71
6.2 Experimental system 72
6.3 Theoretical model 74
6.4 Monte Carlo simulations 77
6.5 Density profiles 78
6.6 Concluding remarks 81

6.1 Introduction

The self-assembly of colloidal particles into crystalline structures has attracted significant attention over the last decades [165, 166, 167, 168, 169, 170] (for a review, see [171]). Besides opening the way to many technological applications in various fields including photonics, chemical sensors and catalysis [172, 173, 174], the study of colloidal self-assembly has also provided new insights into the physics of crystallization thanks to the experimentally accessible length, time and energy scales of colloidal systems [7, 166, 175, 176, 177]. Sedimentation is commonly used to manufacture colloidal crystals, as it provides a simple way to locally increase the volume fraction of a colloidal suspension to induce crystallization. Since the seminal work by Perrin [178], sedimentation has stimulated a wealth of statistical mechanics studies of

Figure 6.1: A picture of the experimental device with the coil centered around the rectangular recipient resting on a tilted plate.

complex fluids under gravity [179, 180, 181, 182, 183, 184, 185, 186, 187, 188, 189] (for a review, see [190]). Measuring the equilibrium density profile of colloidal suspensions provides a method to characterize the thermodynamical properties of the system [180, 181]. The classical density functional theory (DFT) constitutes a well-known tool to describe the equilibrium density profiles for different interparticle interactions, including hard spheres or screened Coulomb [180, 182, 183], electrostatic [181, 184] or magnetic [185] pair potentials, and mixtures of colloids and polymers [186, 187].

Recently, crystallization in a tilted monolayer was studied for a system of hard spheres, allowing a full description of the phase diagram of two-dimensional hard-sphere colloids [188]. On the other hand, sedimentation experiments of a ferrofluid have been conducted recently in a three-dimensional system and successfully fitted by a perturbed virial expansion approach [189].

6.2 Experimental system

The experiments have been realized by Lydiane Bécu and David Gonzalez-Rodriguez at the LCP-A2MC laboratory in Metz. A suspension of superparamagnetic particles (Dynabeads M-450, Life Technologies) [1] is allowed to sediment to

[1] Diameter $2R = 4.4\ \mu$m, $\rho_{\text{part}} = 1.5$ g/cm^3, $V_{\text{part}} = 4/3\pi(2.2.10^{-6})^3$ m^3 and $\chi_{\text{eff}} = 6.10^{-11}$ Am/T [191].

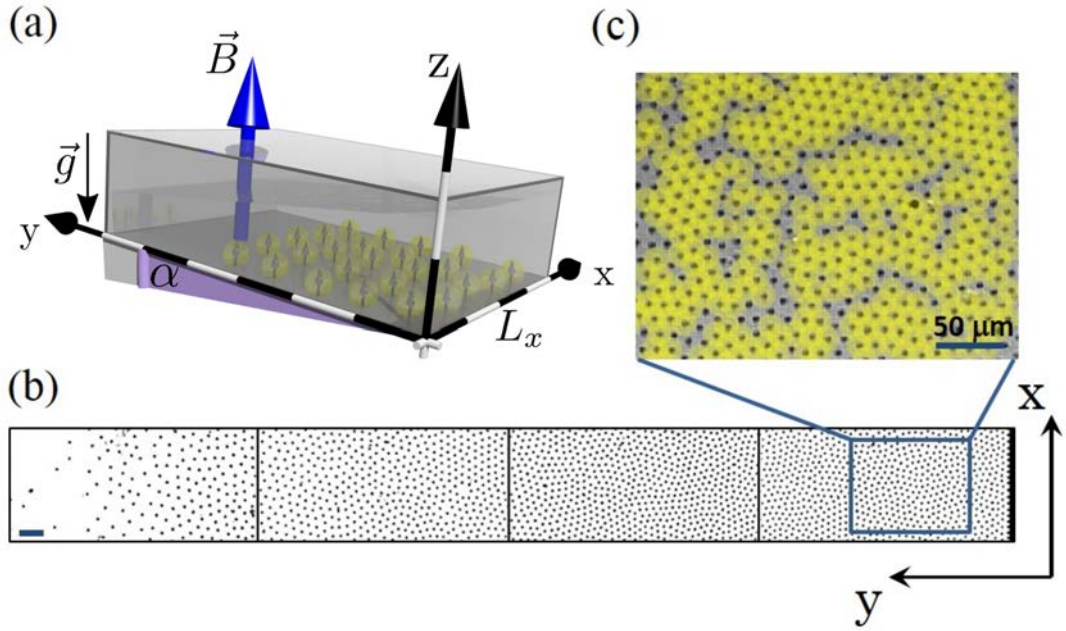

Figure 6.2: Sedimentation of a two-dimensional monolayer of paramagnetic colloids. (a) Sketch of the experimental setup allowing a layer of colloids confined in the (x,y)-plane to be tilted by an angle α to drive sedimentation along the y-direction. (b) Experimental sedimentation profile reconstructed from snapshots recorded at different positions y for a tilt-angle $\alpha = 1.6°$ at $B = 0.9$ mT. A threshold has been applied to the images for better visibility. The scale bar corresponds to 50 μm. (c) Detail of a typical experimental image. Particles arranged on a hexagonal lattice are surrounded by six neighbors and are highlighted in yellow.

the bottom of a rectangular quartz cuvette (Hellma analytics), forming a 1 cm × 1 cm bidimensional array of average initial density ρ_{i}. A coil of diameter 13 cm and height 2.5 cm with 95 loops is centered around the cuvette to generate a magnetic field B_z perpendicular to the array, inducing a repulsive magnetic potential between neighboring colloids. The coil and cuvette rest on a plate that can be tilted to a chosen angle α with respect to the horizontal, subjecting the particles to an in-plane gravity component, $g \sin \alpha$, which drives particle sedimentation along the y-direction, see Fig. 6.2 (a) for a sketch of the setup. The whole setup is built on the stage of an inverted microscope equipped with a CCD camera. It is thus possible to translate the setup along the y-direction in order to access the full density profile of the colloidal array. Due to the small angle existing between the sample plane and the imaging plane, the imaging plane needs to be refocused during stage translation, whereas focus differences within one image are negligible. A typical experimental snapshot reconstructed from images recorded along the y-direction is presented in Fig. 6.2(b). A dense ordered sediment is observed at the lowermost edge of the plane bottom around $y = 0$. In this region, the sediment exhibits a polycrystalline microstructure, characterized by localized crystallites with a hexagonal lattice (Fig. 6.2(c)) [177]. Upon increasing y, the ordering decreases (Fig. 6.2(b)).

6.3 Theoretical model

To quantify the ordering of the colloidal suspension, we investigate the spatial variation of the density profile, $\rho(y)$. The latter is defined as the laterally integrated density profile that reads

$$\rho(y) = \frac{1}{L_x} \int_0^{L_x} n(x, y) dx, \tag{6.1}$$

where $n(x, y)$ stands for the local particle density on the (x, y)-plane and L_x is the length across the bottom edge, see also Fig. 6.2(b). We analytically describe $\rho(y)$ by a DFT approach that we briefly describe in what follows. The pair potential of two parallel identical magnetic dipoles of magnitude χB, see Eq. (2.4), is

$$U_{ij}^{(\mathrm{dip})} = \frac{\mu_0}{4\pi} \frac{\chi^2 B^2}{r_{ij}^3}, \tag{6.2}$$

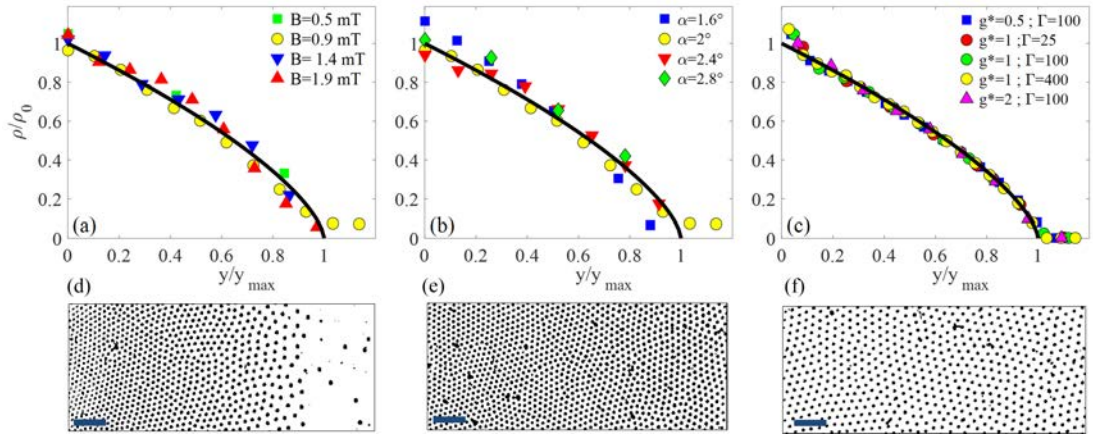

Figure 6.3: Density profiles normalized according to the theoretical model as a function of the normalized upslope distance, see Eq. (6.13) and definition of $y_{\max}$ and ρ_0 in the text. The black line in each plot is the theoretical prediction given by Eq. (6.13). Experimental profiles (a) for different values of the magnetic field B at fixed inclination angle $\alpha = 2°$ and (b) for different values of α at constant magnetic field $B = 0.9$ mT. (c) Simulation profiles for different values of g^* and Γ. Experimental snapshots of the sedimented monolayer recorded at y =490-980 μm are shown for $\alpha = 2°$ and B =0.5 mT (d), B =0.9 mT (e) and B =1.9 mT (f). The scale bars correspond to 50 μm.

where μ_0 is the permeability, χ is the magnetic susceptibility, and r_{ij} is the distance between the two dipolar particles i and j. At prescribed coordinate y, it is assumed that the local density $\rho(y)$ results from a hexagonal lattice with lattice constant $a(y)$ yielding $\rho(y) = 2/[\sqrt{3}a(y)^2]$. Thereby, the dipole potential energy associated with particle i located at y_i obeys

$$U_i^{(\mathrm{dip})} = \frac{1}{2}\sum_j U_{ij}^{(\mathrm{dip})} = \frac{2M}{5}\frac{\mu_0}{4\pi}\chi^2 B^2 \rho(y_i)^{3/2} \tag{6.3}$$

where $M = 2^{-7/2}3^{3/4}5M_0 \approx 11.116$ is a geometrical constant with $M_0 \approx 11.034$ denoting the Madelung constant obtained by lattice sum [192, 193]. The gravity contribution is merely given by

$$U_i^{(\mathrm{gravity})} = m_c g y_i \sin\alpha, \tag{6.4}$$

where m_c is the effective mass of a colloid (corrected for buoyancy), so that the total potential energy associated with particle i at y_i reads

$$U_i = U_i^{(\text{gravity})} + U_i^{(\text{dip})}. \tag{6.5}$$

Within this framework, we are able to write the free energy of the system per unit width L_x, see also setup in Fig. 6.2(a), as [180]

$$\beta F = \int_0^\infty \left\{ \rho(y) \left[\ln(\Lambda^2 \rho(y)) - 1 \right] + \rho(y) \frac{y}{\ell_s} + \frac{2M}{5} \Gamma \ell_s^3 \rho(y)^{5/2} \right\} \mathrm{d}y, \tag{6.6}$$

where Λ is the (irrelevant) thermal wavelength. The first term in Eq. (6.6) represents the ideal gas part. The second term is the gravity contribution with

$$\ell_s = (\beta m_c g \sin\alpha)^{-1} \tag{6.7}$$

denoting the sedimentation length, where $\beta = 1/k_B T$ (k_B is the Boltzmann constant and T the temperature). The last term corresponds to the dipole-dipole interaction with

$$\Gamma \equiv \frac{\mu_0}{4\pi} \frac{\chi^2 B^2}{k_B T \ell_s^3} \tag{6.8}$$

being the dimensionless magnetic coupling. At equilibrium, the free energy is minimized, subjected to the condition of conservation of the total number of particles, i.e.

$$\int_0^\infty \rho(y) \mathrm{d}y = \rho_x, \tag{6.9}$$

where ρ_x is the projected density, obtained as the total number of particles divided by L_x. The Euler-Lagrange equation related to Eq. (6.6) is given by

$$\frac{1}{\beta} \left[\ln(\Lambda^2 \rho(y)) - 1 + \Lambda^2 + \frac{y}{\ell_s} + M \Gamma \ell_s^3 \rho(y)^{3/2} \right] - \lambda = 0. \tag{6.10}$$

where λ is the Lagrange multiplier associated with constraint (6.9). By denoting $\rho_0 = \rho(y=0) = \rho_0(\rho_x)$ we also have

$$\frac{1}{\beta} \left[\ln(\Lambda^2 \rho_0) - 1 + \Lambda^2 + M \Gamma \ell_s^3 \rho_0^{3/2} \right] - \lambda = 0. \tag{6.11}$$

Finally, by combining Eq. (6.11) and Eq. (6.10), the Euler-Lagrange equation can be written as:

$$\ln\frac{\rho(y)}{\rho_0} + M\Gamma\left(\rho(y)^{3/2} - \rho_0^{3/2}\right)\ell_s^3 = -\frac{y}{\ell_s}. \tag{6.12}$$

At this stage, static quantities are fully determined by assigning values to Γ and ρ_x and employing ℓ_s as unity of length. In the high temperature limit $\Gamma\rho_x^3\ell_s^3 \ll 1$, the logarithmic term in Eq. (6.12) dominates and the well known Perrin's result $\rho(y) = \frac{\rho_x}{\ell_s}\exp(-y/\ell_s)$ is recovered [178]. Interestingly, in the low temperature limit $\Gamma\rho_x^3\ell_s^3 \gg 1$, the logarithmic term in Eq. (6.12) becomes negligible. In that regime which corresponds to experimental conditions, the following relevant result is obtained

$$\left(\frac{\rho(y)}{\rho_0}\right)^{3/2} = 1 - \frac{y}{y_{\max}}, \tag{6.13}$$

where

$$\rho_0 = (5/3)^{2/5}\gamma^{2/5}\rho_x^2, \tag{6.14}$$

$$y_{\max} = (5/3)^{3/5}\gamma^{-2/5}\rho_x^{-1} \tag{6.15}$$

with

$$\gamma = (\Gamma\rho_x^4\ell_s^4 M)^{-1} = \frac{4\pi m_c g\sin\alpha}{M\mu_0\chi^2 B^2\rho_x^4} \tag{6.16}$$

reflecting the ratio between the gravity potential and the magnetic interaction. Equation (6.13) will be referred to as the zero-temperature local density approximation (LDA) result (or model). In what follows, this remarkably simple analytical expression (6.13) will be tested against experiments and simulations.

6.4 Monte Carlo simulations

To gain further insight into the physical mechanisms of sedimenting paramagnetic colloids in two dimensions, Monte Carlo (MC) simulations [194, 195] based on the (exact) Hamiltonian,

$$\beta U_{\rm MC} = \sum_i \frac{y_i}{\ell_s} + \frac{1}{2}\sum_{i\neq j}\frac{\Gamma\ell_s^3}{r_{ij}^3}, \tag{6.17}$$

are performed in the canonical ensemble mimicking the experimental situation. The number of particles N is fixed at $N = 1000$. [2] The simulation cell consists of a

[2] We have performed beforehand some simulations with N=2000. It turns out that the density profiles are virtually indistinguishable from those obtained with with N=1000. Hence we are

$L_x \times L_y$ rectangular box with periodicity in the x-direction, consistent with the setup in Fig. 6.2. The long-range dipole-dipole interactions are computed using a Lekner-like sum technique adapted for systems with periodicity in one direction [112]. Typically $10^5 - 10^6$ MC steps are devoted for equilibration and statistics are gathered over an additional 10^6 MC steps.

6.5 Density profiles

The experimental density profiles normalized according to the zero-temperature LDA model, see Eq. (6.13), are displayed in Fig. 6.3(a) and (b). [3] We adopt as our baseline conditions $\alpha = 2°$ and $B = 0.9$ mT, corresponding to $\gamma \approx 3.0 \times 10^{-4}$ [4]. Figure 6.3 shows the effect (a) of varying the strength of the magnetic field and (b) of changing the slope. In both cases, an excellent agreement between theory and experiment is found. Figure 6.3(d)-(e) shows experimental snapshots for $\alpha = 2°$ and different strengths of the magnetic field. A similar structural evolution is observed upon increasing the slope at constant magnetic field. In the same spirit as the experiments, we also choose a reference system in our simulations ($\Gamma = 100, g^* = 1$) defining the reference sedimentation length $\ell_s^{(\mathrm{ref})}$ In order to establish a tractable comparison between experiments and simulations, we introduce a reduced effective gravity $g^* \equiv \frac{g_{\mathrm{eff}}}{g_{\mathrm{ref}}}$ where $g_{\mathrm{eff}} = g \sin\alpha$ and $g_{\mathrm{ref}} = g \sin\alpha_{\mathrm{ref}}$. For the reference case, $\ell_s = \ell_s^{(\mathrm{ref})}$ where $g^* = 1$ and $\Gamma = 100$. A rectangular cell with $L_x = 25\ell_s^{(\mathrm{ref})}$ and $L_y = 1000\ell_s^{(\mathrm{ref})}$ has been used for all the presented simulations. The density profile of the reference case is displayed in Fig. 6.4(b). A smoothing of the simulation density profiles [5] covering a wide range of Γ and g^* values (see Fig. 6.4), leads to a virtually quantitative agreement with theory, see Fig. 6.3(c). Hence, the experimental profiles exhibit an identical behavior to that of the smoothed density profiles stemming from the MC simulations. The absence of oscillations in the experiments is due to polycrystallinity, detectable in Fig. 6.2(c), which averages out the density oscillations of single domains.

confident that our two-dimensional systems with N=1000 do not suffer from finite size effects.

[3] Density profiles $\rho(y)$ are obtained by counting the number of particles located in a window of width $d_y = 100$ μm centered around the coordinate y. When a smaller width is used, the resulting profiles become very noisy, due to window becoming smaller than the polycrystal sizes.

[4] The corresponding value of the gravitational length in our experiments, based on a temperature $T \approx 300$ K and a particle buoyant weight $m_c g \approx 2.210^{-13}$ N, is $l_s \approx 1$ μm.

[5] The smoothed density profiles are achieved by coarsening the bin width of bare (oscillating) profiles over typically $20\ell_s^{(\mathrm{ref})}$.

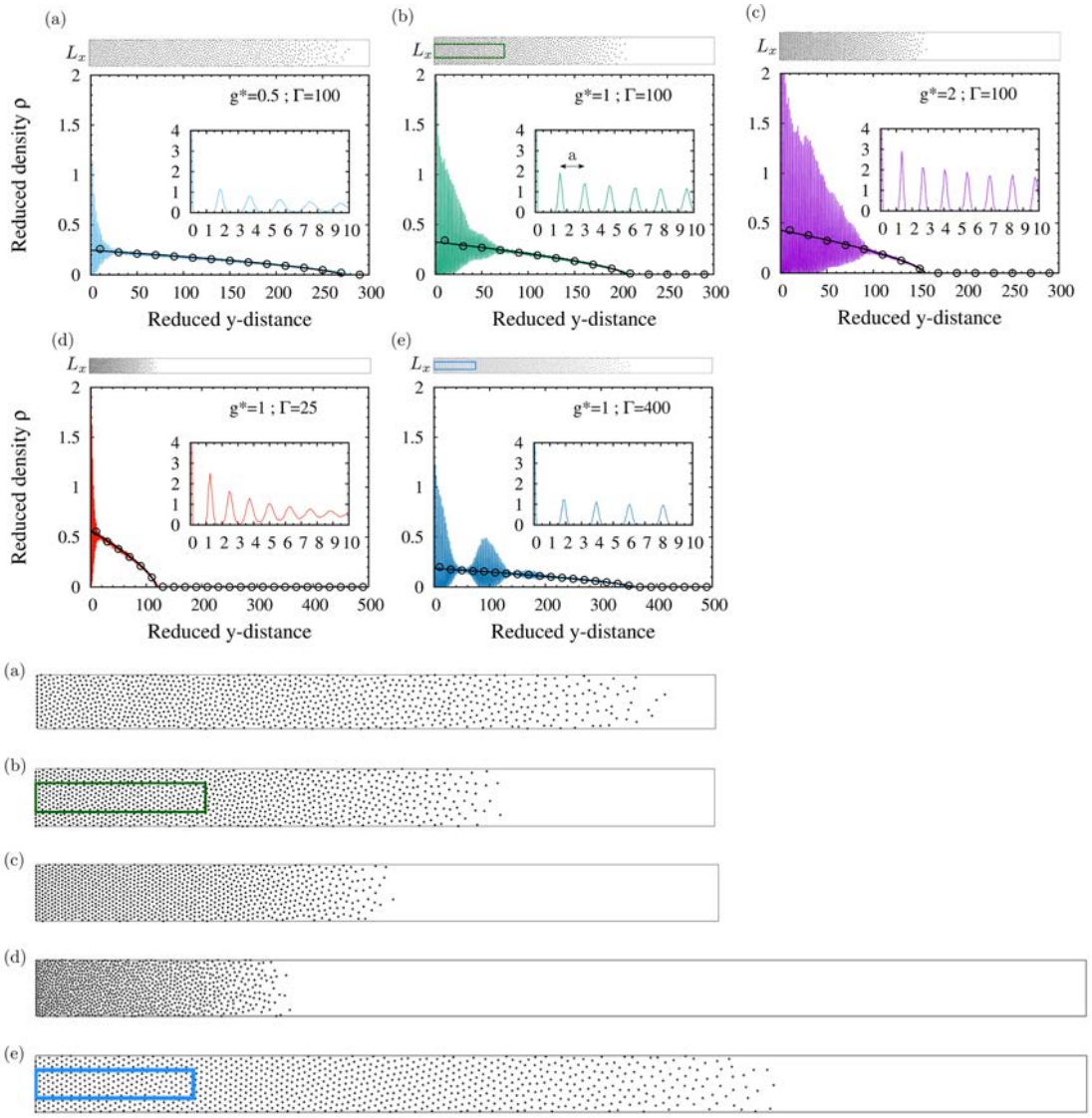

Figure 6.4: Monte Carlo simulation density profiles with magnetic coupling $\Gamma = 100$ for different values of the gravity parameter (a) $g^* = 0.5$, (b) $g^* = 1$, and (c) $g^* = 2$. Three additional profiles at prescribed $g^* = 1$ with (d) $\Gamma = 25$ and (e) $\Gamma = 400$. are also displayed. The thick (black) line is the LDA theoretical prediction, see Eq. (6.13). The circles represent the smoothed density profiles, see also text. The insets show a magnified view. Accompanying microstructure snapshots are sketched on the top of panels (a)-(e) and magnified versions are shown at the bottom half of the figure. The unit length is $\ell_s^{(\mathrm{ref})}$ for the whole figure.

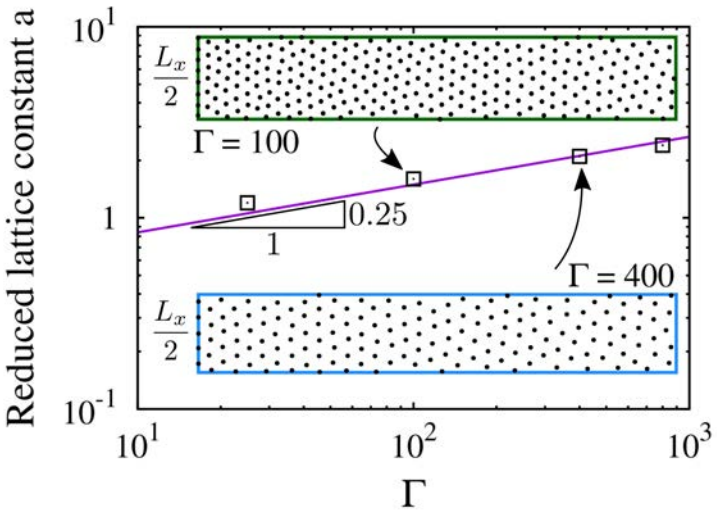

Figure 6.5: Lattice constant a, see inset in Fig. 6.4(b) for illustration, as a function of Γ with $g^* = 1$. The solid line is the best fit for a power law of the form $\Gamma^{0.25}$. The insets are a magnified view of the boxed regions in snapshots shown in Fig. 6.4(b) and (e). The unit length is $\ell_s^{(\mathrm{ref})}$.

The vivid *oscillatory* behavior revealed in the bare simulation density profiles is a signature of the strong layering occurring around the bottom edge, see Fig. 6.4 [180, 182]. Sufficiently far away from the bottom edge, non-smoothed profiles quantitatively match with theory, signaling a disordered state, see also snapshots provided in Fig. 6.4. Increasing gravity alone at prescribed magnetic field ($\Gamma = 100$) enhances the ordering and its range, see Fig. 6.4(a)-(c). Concomitantly, the (apparent) lattice constant a (distance between two successive peaks, see inset in Fig. 6.4(a)) decreases with gravity. Upon increasing the magnetic field at prescribed gravity ($g^* = 1$), see Fig. 6.4(b), (d) and (e) the range of the layering becomes broader. Thereby, the lattice constant increases with Γ, see Fig. 6.4 and Fig. 6.5. More specifically, a remarkable power law like $a/\ell_s \sim \Gamma^{1/4}$ emerges, see Fig. 6.5. The latter can be rationalized with the simple idea of a balance between gravity force ($\sim g = constant$) and repulsive magnetic force ($\sim \Gamma/a^4$). Interestingly, at strong coupling $\Gamma \geq 400$, see Fig. 6.4(e) , the density profile is reminiscent of a standing wave as a result of a non trivial balance between gravity (pushing the particles towards the bottom) and strong repulsive magnetic interaction (expelling particles from the bottom). In the situation of moderate layering with $\Gamma = 25$, see Fig. 6.4(d), it is worth mentioning that the simple zero-temperature LDA prediction remains robust to describe the smoothed density profile. Thereby, even at a finite

temperature well above zero, the zero-temperature LDA approach remains suited to characterize density profiles far from strong ordering.

6.6 Concluding remarks

In summary, we have experimentally and theoretically advocated the ordering mediated by a non-trivial balance between sedimentation and long-ranged dipole-dipole interparticle repulsion occurring within a colloidal monolayer. The experimental density profiles are in excellent agreement with predictions from density functional theory and Monte Carlo simulations. Thereby, a strikingly simple analytical solution, based on the zero-temperature limit in the local density approach, has been derived, see Eq. (6.13). The latter accounts for the experimentally found density profiles ranging from the solid-like state (close to the bottom edge) to liquid-like state (far from the bottom edge). Computer simulations indicate that strong crystal layering occurs, near the container's bottom wall, as signaled by vivid oscillations in density profiles. The associated lattice constant is roughly dictated by $\Gamma^{1/4}$, reflecting merely a force balance between gravity and dipole-dipole interaction. Such oscillations are smoothed out in experiments, an effect attributed to polycrystallinity. It would be interesting for future studies to check whether our approach can be generalized to other soft repulsive potentials such as a power law of the interparticle distance [196] or a screened Coulomb potential. Overall, our findings demonstrate that the microstructure of the sediment can be tuned and predicted by choosing the sedimentation slope and the external magnetic field, thus providing an efficient and convenient technique for the fabrication of controlled ordered monolayers.

Chapter 7

Layered dipolar particles in external magnetic field

This chapter is devoted to the theoretical investigation of mono- and bilayer systems under an external perpendicular magnetic field whose results will be published soon [197].

Contents

7.1 Introduction 83
7.2 Model 84
7.3 Method 85
7.4 Monolayer in external field 86
7.5 Bilayer in external field 89
7.6 Concluding remarks 91

7.1 Introduction

Two-dimensional dipolar systems (monolayers or few-layer systems) are a fertile area of research [103, 171, 198]. Some experimental examples are (thin) magnetic films [198, 199, 200], magnetic bubbles in garnet films [201, 202], magnetic particles on a substrate [7, 166, 203, 204, 205] or floating on the surface or the meniscus of a liquid [206, 207, 208]. Such systems can benefit to the design of novel materials (e.g. photonic band-gap [209] and data storage devices [210]) and can also act as a model to better understand biological certain mechanisms/processes (e.g. microtubule [211] and lipid layers formations [212]). Large two-dimensional dipolar systems exhibit a rich phase behavior especially observed in computational simulations [213, 214, 215, 216] including systems in an external field [217] (for a review, see [103]). In

a pioneering theoretical work, the ground state of a planar rhombic lattice with an arbitrary rhombicity angle has been addressed [81, 218]. In particular, the influence of an (imposed) lattice symmetry on the resulting dipole moment distribution (in the ground state) was advocated. A related recent study involving an interaction cutoff confirmed the latter findings [219]. Conversely, under a tilting magnetic field, many structural transitions are induced in a two-dimensional superparamagnetic suspension depending on the field strength and the density [220].

In our study where we have to deal with permanent dipole moments (i.e., ferromagnetic particles), the only relevant component of the external magnetic field is perpendicular one.

7.2 Model

The crystal layered structures made up of dipolar particles are illustrated in Fig. 7.1 for the monolayer and in Fig. 7.4 for the bilayer. The constitutive dipolar particles are hard spheres of diameter d that sets the unit of length. They each possess a dipole moment of identical magnitude $\|\vec{m}\| = m$ set to unity. The presence of the external normal magnetic field, $\vec{B} = B\vec{e}_z$ (with $\vec{e}_z$ standing for the unit vector along the z-axis), involves the Zeeman term $-\vec{m} \cdot \vec{B}$ $(= -m_z B)$. Hence, in general, for a prism unit cell containing N dipolar particles located at $\vec{r}_1, \ldots, \vec{r}_N$, the dipolar energy per unit cell, U_{cell}, follows:

$$\begin{aligned} U_{\text{cell}} &= \frac{1}{2} \sum_{i,j}^{N} {\sum_{\vec{n}}}' \frac{C}{|\vec{r}_{ij} + \overleftrightarrow{t} \cdot \vec{n}|^3} \left[\vec{m}_i \cdot \vec{m}_j \right. \\ &\quad \left. -3 \frac{\vec{m}_i \cdot (\vec{r}_{ij} + \overleftrightarrow{t} \cdot \vec{n}) \vec{m}_j \cdot (\vec{r}_{ij} + \overleftrightarrow{t} \cdot \vec{n})}{|\vec{r}_{ij} + \overleftrightarrow{t} \cdot \vec{n}|^2} \right] \\ &\quad - \sum_{i=1}^{N} m_{i,z} B, \end{aligned} \tag{7.1}$$

where $\overleftrightarrow{t}$ is a 2×2 matrix whose two columns are given by the spanning vectors $\vec{a}$ and $\vec{b}$. $\vec{n}$ designates a vector with integer components (n_x, n_y), each ranging from $-\infty$ to $+\infty$. The prime in Eq. (7.1) indicates that, when $\vec{n} = 0$, i must be different from j.

On the numerical computational side, in order to overcome the slow (conditional) convergence [221] in Eq. (7.1), an efficient Ewald sum technique adapted to the

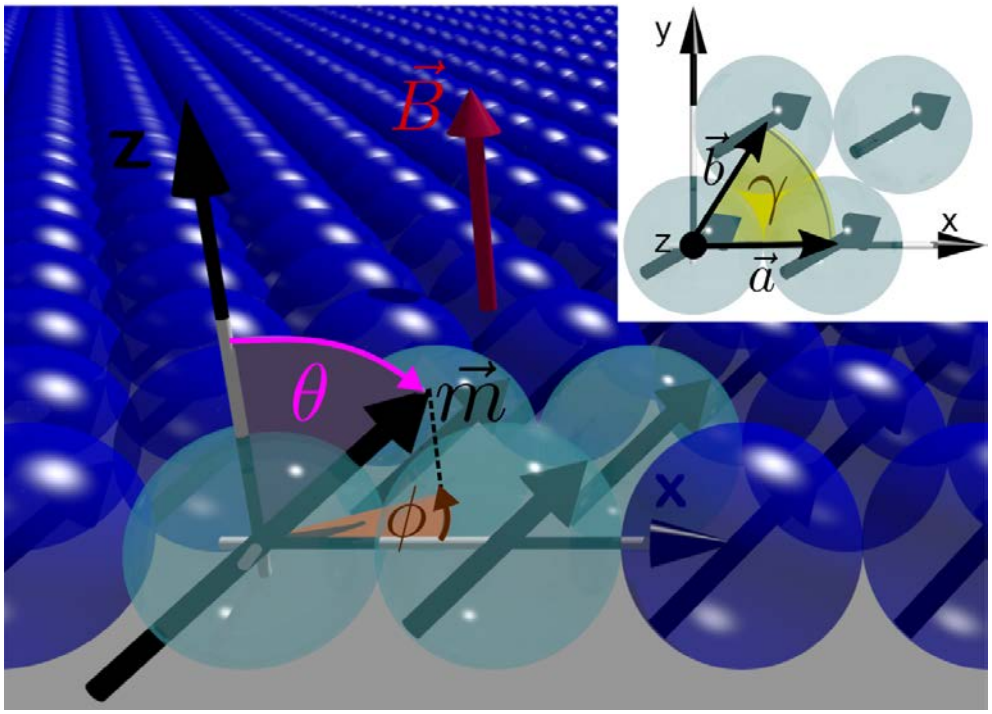

Figure 7.1: Sketch of the geometric setup for an infinite monolayer in an external magnetic field. A monoatomic unit cell (light spheres) with its replica (dark spheres) are shown. A top-view of the unit cell is provided as inset.

parallelogram base with periodicity in two dierctions was used [222]. As far as the (exact) analytical approach is concerned, an innovative dedicated tractable sum was developed, see details in Appendix B. The energy scale is set by $U_{\uparrow\uparrow}$, see Eq. (2.10). Thereby, the reduced dipolar energy per particle, u, is merely given by $u = \frac{1}{N}\frac{U_{\text{cell}}}{U_{\uparrow\uparrow}}$.

7.3 Method

Ground states are obtained by minimization procedures starting with a generic parallelogram cell made up of two particles. Thus, for the one-layer case, the minimization of u at prescribed magnetic field involves nine parameters corresponding to the two modules of spanning vectors a and b, the angle $\gamma = \widehat{(\vec{a}, \vec{b})}$, the two Cartesian coordinates of the second constitutive particle, and the four related dipole orientation angles, see also Fig. 7.1. In the two-layer situation, an additional variable sets in which is the transverse shift between the two layers. The efficient SLSQP method taking natively into account constraints and requiring derivatives of the objective function [62] is employed, see Section 2.3.2. Typically 2×10^3 starting

random configurations were needed to reach the global minimum.

7.4 Monolayer in external field

Results about the monolayer are now presented. Preliminary numerical calculations indicate that the unit cell of the crystal ground state is always *rhombic* ($a = b = 1$) and monoatomic ($N = 1$). Thereby, the angle γ will be referred to as the rhombicity angle. A major finding is the slight but relevant symmetry breaking of the hexagonal lattice upon applying an external magnetic field, i.e. $\gamma > 60°$ when $B > 0$. This intriguing result can be inspected in Fig. 7.2(a), where $\gamma(B)$ is plotted. Clearly, the deviation from the hexagonal lattice increases monotonically with the magnetic field B, see Fig. 7.2(a). An important physical consequence is that the *continuous degeneracy* of the inplane dipole $\vec{m}_\rho = \vec{m} - m_z\vec{e}_z$, existing in a perfect hexagonal lattice ($\gamma = 60°$) [218], is now suppressed in presence of an external magnetic field that induces rhombicity ($\gamma > 60°$). The related profile of the induced magnetization $m_z(B)$ is displayed in Fig. 7.2(b). It exhibits a quasi linear in the crystal phase and reaches a value of the order of 20% around the solid/gas transition, see Fig. 7.2(b). [1] The latter is merely reached when the decohesion energy is beaten by the Zeeman term, see also Eq. 7.2. The related profile of the ground state energy as a function of the applied magnetic field B, $u(B)$, can be found in Fig. 7.2(c). As expected, the cohesive energy increases with B (i.e., getting less favorable) whereas the total energy decreases. The gas/solid transition occurs at $B = B_{tr} = 3.04$ dictated by a vanishing cohesive energy, see also Fig. 7.2(c).

Deeper understanding can be gained by solving exactly and analytically the depicted problem of magnetic layers exposed to a magnetic field. It turns out that this formidable challenge is feasible noticing the still strong symmetry of the problem and upon dexterously rewriting the Hamiltonian given by Eq. (7.1) in a tractable way. In a general manner, it is insightful to write the dipolar energy u for a rhombic lattice in the following (exact) form:

$$u = E_0(\gamma) + E_1 m_z + E_2(\gamma) m_z^2 \tag{7.2}$$

with $E_0(\gamma)$ representing the cohesive energy of the rhombic lattice, $E_1 = -B$ stemming from the Zeeman term, and $E_2(\gamma) > 0$ causing the dipolar decohesion. In

[1] Concomitantly, the azimuthal angle ϕ of the dipole corresponds to $\gamma/2$ in agreement with past studies without external magnetic field [218, 219].

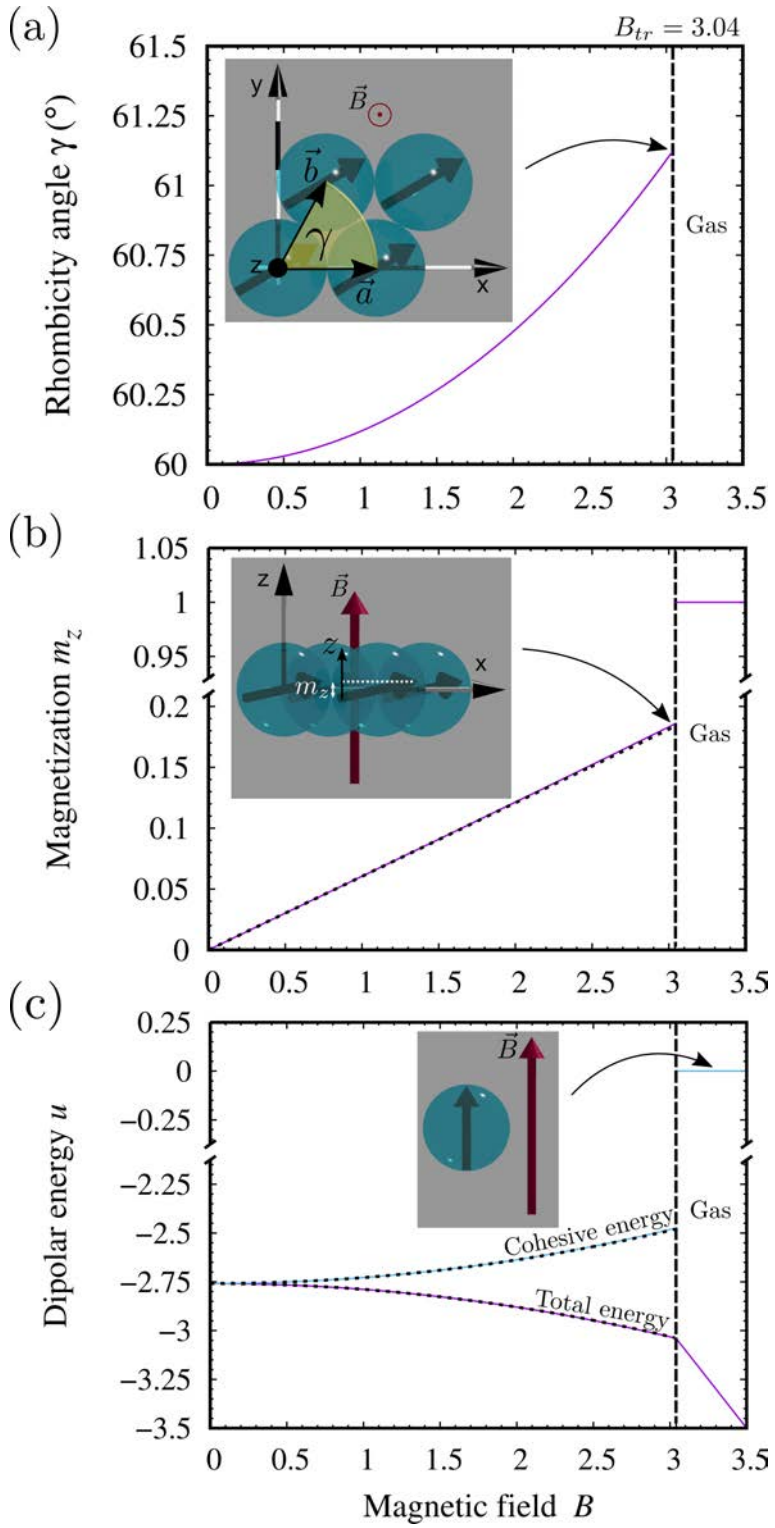

Figure 7.2: (a) Rhombicity angle γ, (b) z-component of the dipole moment m_z and (c) total and cohesive energy profiles as a function of the external magnetic field intensity B for the monolayer. A top- and side-view of the rhombic unit cell are displayed as insets.

Table 7.1: Numerical values of χ,B_{tr} and E_0 in different scenarios.

	Monolayer		**Bilayer**
	Exact theory	HLA model	Exact theory
χ	B-dependent	6.042×10^{-2}	5.868×10^{-2}
B_{tr}	3.0391	3.0372	3.2062
E_0	B-dependent	-2.759	-2.905

Appendix B.1, we provide and derive the full exact analytical and tractable expression of $u(m_z, \gamma; B)$ obtained at prescribed magnetic field B. Having this at hand, one can extract the magnetization in the ground state stemming from the condition $\frac{\partial u}{\partial m_z}\Big|_B = 0$ that trivially yields

$$m_z = \frac{B}{2E_2(\gamma)}. \tag{7.3}$$

Hence, the susceptibility χ of the system is merely identical to $(2E_2)^{-1}$. Similarly, the minimum energy condition requires also simultaneously $\frac{\partial u}{\partial \gamma}\Big|_B = 0$, leading to a highly intricate dependence of γ with B, see Appendix B.1.1 for calculation details and Fig. 7.2(a) for a visualization of the corresponding profile $\gamma(B)$. Consequently, the ground state energy of the rhombic phase reads

$$u(B) = E_0(B) - \frac{\chi(B)}{2} B^2, \tag{7.4}$$

whose profile is displayed in Fig. 7.2(c).

Another analytical route which is much more simple, but not exact, would be to neglect the rhombicity angle variation, i.e. always assuming a hexagonal lattice [$\gamma(B) = 60°$], see Appendix B.1.2 for details. The latter approach will be referred to as the *hexagonal lattice approximation* (HLA). In this scenario, the ground state energy reads

$$u^{\mathrm{HLA}} = -2.759 - 3.021 \times 10^{-2} B^2, \tag{7.5}$$

where $E_0 = -2.759$ corresponds to the well known cohesive energy of a hexagonal lattice [41, 219] and $\chi = 6.042$ is the related susceptibility, see Appendix B.1.2 for the full derivation. The profile of $u^{\mathrm{HLA}}(B)$ specified by Eq. (7.5) is displayed in Fig. 7.2(c) too, rationalizing also the (quasi) linear behavior found in $m_z(B)$, see Fig. 7.2(b). The various values of χ and B_{tr} are gathered in Table 7.1.

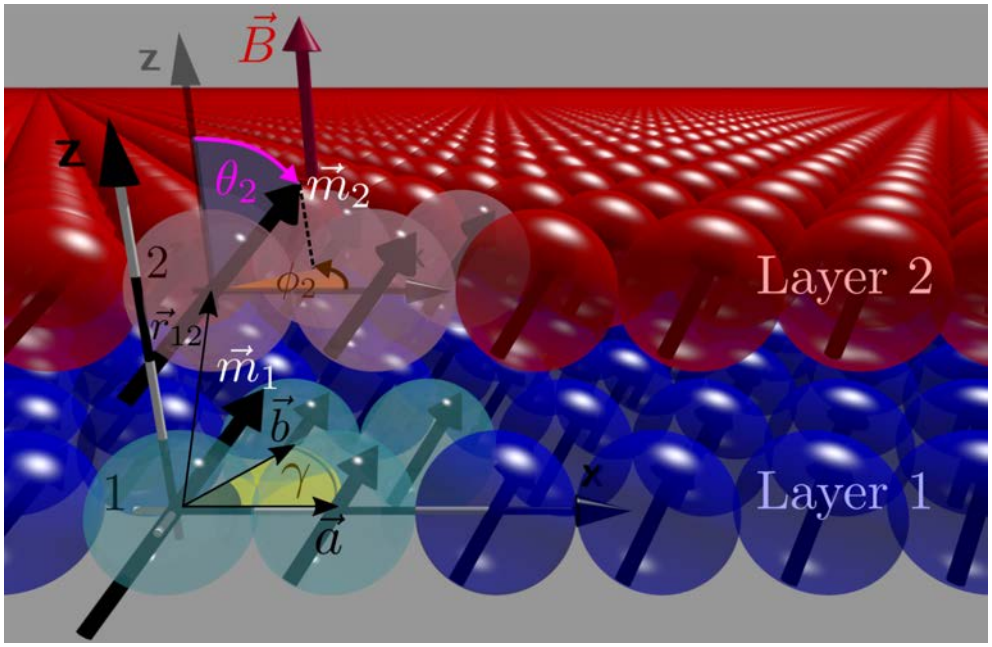

Figure 7.3: Sketch of the geometric setup for an infinite bilayer in an external magnetic field. A diatomic unit cell (light spheres) with its replica (dark spheres) are shown.

7.5 Bilayer in external field

We now address the bilayer system whose setup is sketched in Fig. 7.3. Interestingly, our numerical optimization predicts that the two layers adopt a hexagonal lattice in the crystal ground state at finite applied external magnetic field. It is to say that the two-layer superlattice is invariant upon exerting a magnetic field and coincides with the body-centered tetragonal lattice. [2] This strong symmetry preservation allows an exact analytical description too that is detailed in Appendix B.2. As a matter of fact, relation (7.2) gets simplified where the γ-dependence vanishes. It can be shown, see also Appendix B.2, that the (exact) dipolar energy u in the ground state verifies:

$$u_{\text{bilayer}} = -2.905 - 2.934 \times 10^{-2} B^2, \tag{7.6}$$

whose profile can be found in Fig. 7.4(a). Notice the high ressemblence with the (approximate) monolayer energy u^{HLA}, see Eq. (7.5). The enhanced cohesion upon

[2] The azimuthal angle ϕ of the dipole corresponds to γ, thus the bilayer magnetization matches that of the body-centered tetragonal ground state. In contrast with the monolayer case, here there is no longer a continuous degeneracy of the dipole moment orientation.

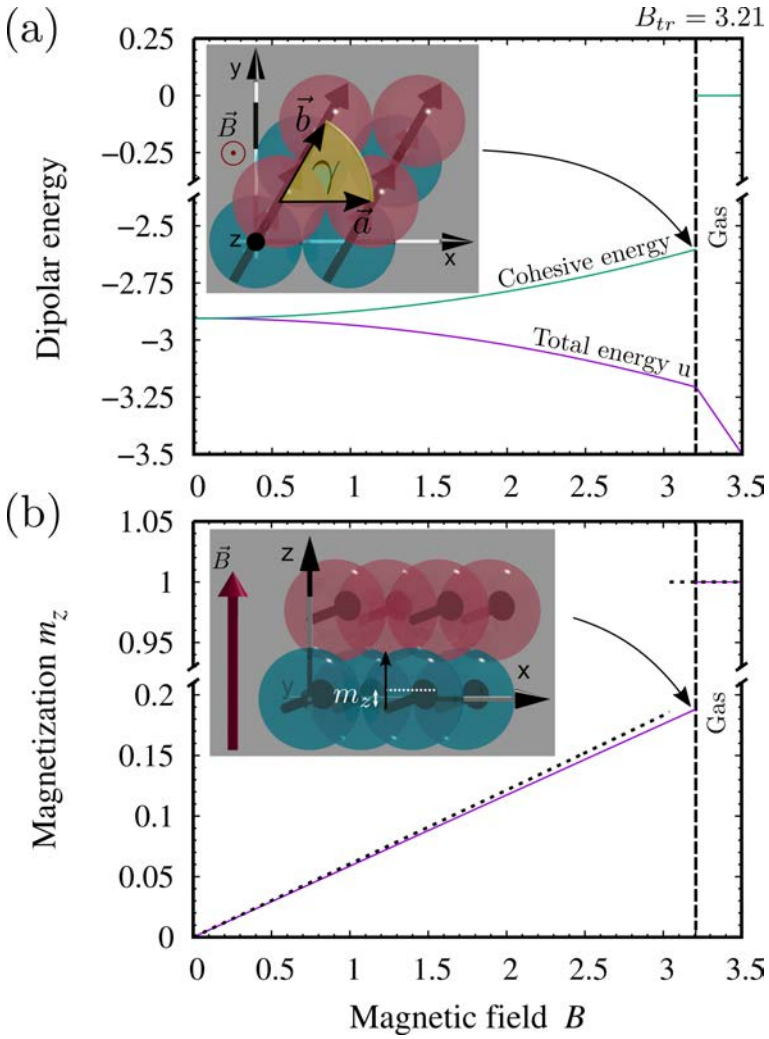

Figure 7.4: (a) Total and cohesive energy profiles and (b) z-component of the dipole moment m_z as a function of the external magnetic field intensity B for the bilayer. A top- and side-view of the two-layer superlattice are displayed as insets.

stacking (here $E_0 = -2.905$) leads to two notable features:

(i) A lower susceptibility emerges where (see Appendix B.2.1 for derivation)

$$m_z^{\text{bilayer}} = 5.868 \times 10^{-2} B, \tag{7.7}$$

whose profile appears in Fig. 7.6(b), see also Table 7.1.

(ii) The solid/gas transition is shifted to higher magnetic field, see Fig. 7.4(a) and also Table 7.1.

7.6 Concluding remarks

In summary, we have investigated theoretically the ground state of mono- and bilayer dipolar systems in a perpendicular external magnetic field. The unit cell of the monalayer ground state is always found to be rhombic. Without external field, the well-known hexagonal lattice with a continuously degenerate ferromagnetic state is recovered as ground state [218]. At non-zero external field, the hexagonal lattice symmetry and the related continuous degeneracy are broken. These features established by numerical minimization are fully supported by an exact analytical solution derived by assuming a rhombic unit cell. The symmetry breaking is very small, noticing that an even more elegant analytical solution based on a hexagonal lattice approaches very closely the exact results. In strong contrast, numerical minimization has predicted that the ground state structure of the bilayer system is invariant under an applied perpendicular magnetic field. At finite external magnetic field, the lattice of each layer is hexagonal and the composite superlattice of the bilayer coincides with the body-centered tetragonal lattice. From the symmetry features predicted by our preliminary minimization calculations, exact analytical expressions have also been developed.

More generally, our findings can lead to new pathways of tuning the crystal structures of magnetic layers. Indeed, in an experimental situation the crystal structure can survive beyond the (theoretically) predicted transition magnetic field (B_{tr}) due to energy barriers.

Chapter 8

Three-dimensional dipolar crystals

The effect of densification on the crystal ground states elucidated in the present chapter are reported in *Physical Review Letters* [116].

Contents

8.1 Introduction 93
8.2 Model 94
8.3 Method 95
8.4 Dipolar crystal phases 97
8.5 Geometric order parameters 100
8.6 Concluding remarks 104

8.1 Introduction

Crystallization of dipolar systems has recently received a great deal of attention due to their intriguing phase behavior [48, 223, 224]. In molecular systems such as hydrogen cyanide, two crystal structures have been experimentally observed (e. g., tetragonal and orthorhombic phases upon decreasing temperature [225] or increasing pressure [226]). In an analogous way and interestingly, so-called complex fluids such as colloidal systems made up of dipolar particles can exhibit such solid-solid transitions too. A great advantage there over the classical molecular systems is that the crystal phases in colloidal suspensions can be visualized in direct real space, e.g., by confocal microscopy [12]. Besides, the possibility to steer the crystal structure by an external (electric and/or magnetic) field, makes colloidal systems very promising candidates for photonic applications [227, 228, 229]. A common feature of all these observed phases at different length scales is the strong orientational

ordering leading to assembled "ferrochains" owing to the anisotropic dipole-dipole driving force.

On the theoretical side, although dipolar hard spheres certainly correspond to the most simple and investigated dipolar system, its full phase diagram is still puzzling [230, 231, 232, 233, 234]. It is by now well-known that the ground state of dipolar hard spheres corresponds to the body-centered tetragonal (bct) structure. Tao and Sun predicted theoretically this phase in the early 90's [38] and it was later confirmed by computer simulations [107, 235, 236] and experiments on colloidal systems [10, 12]. Nevertheless, the delicate problems of freezing and solid-solid transitions are still under debate [236, 237, 238, 239]. The new phase called clinohexagonal prism (chp) merely consists of an oblique prismatic lattice with a hexagonal base. We show that the chp phase, overlooked in the literature, sheds important light on the mechanisms of crystallization in dipolar systems. The remarkable fact that the base is hexagonal is in full agreement with the concept of locally optimized (excluded volume vs dipolar) lateral correlations [45]. Basically, the three-dimensional ground states can be envisioned as the stacking of two-dimensional ground state layers with a continuous shift that is density dependent. [1]

8.2 Model

The constitutive dipolar particles of investigated crystals are hard spheres of diameter d, that sets the length unit, possessing a dipole moment $\vec{m}_i$ with i designating the label of an arbitrary particle. The orientation of the dipole moment $\vec{m}_i$ is stated by means of the azimuthal ϕ_i and the polar angle θ_i according to $\vec{m}_i = (\cos\phi_i \sin\theta_i, \sin\phi_i \sin\theta_i, \cos\theta_i)$, see Fig. 8.1. In general, for a prism unit cell containing N dipolar particles located at $\vec{r}_1, \ldots, \vec{r}_N$, the dipolar energy per unit cell, U_{cell}, is given by:

$$U_{\text{cell}} = \frac{1}{2}\sum_{i,j}^{N}{\sum_{\vec{n}}}' \frac{C}{|\vec{r}_{ij} + \overleftrightarrow{t}\cdot\vec{n}|^3}\left[\vec{m}_i\cdot\vec{m}_j - 3\frac{\vec{m}_i\cdot(\vec{r}_{ij}+\overleftrightarrow{t}\cdot\vec{n})\vec{m}_j\cdot(\vec{r}_{ij}+\overleftrightarrow{t}\cdot\vec{n})}{|\vec{r}_{ij}+\overleftrightarrow{t}\cdot\vec{n}|^2}\right], \tag{8.1}$$

[1] This intuitive pictures breaks down at very high packing, in the vicinity of the hcp phase, where dipole moments point in the normal direction of the dense chains (i.e., perpendicularly to the hexagonal lattice base). It is to say that the latter direction corresponds to that of non-dense chains, see also Fig. 8.2.

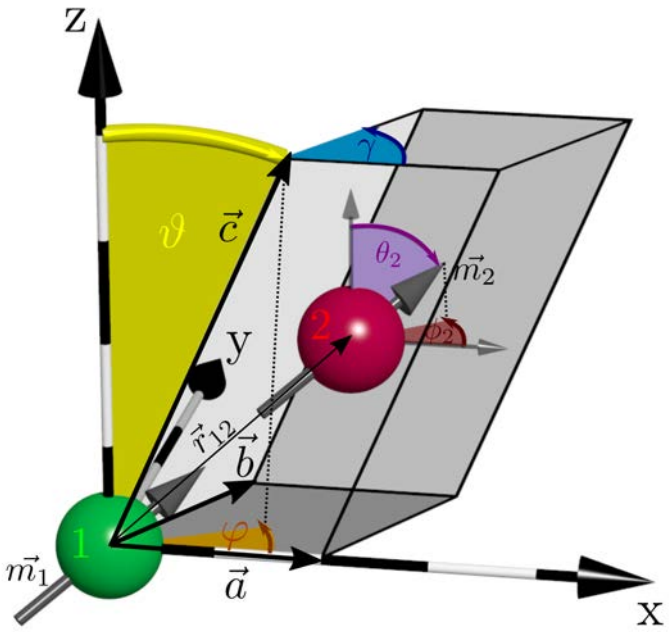

Figure 8.1: Scheme of a parallelogram-based prism as unit cell containing two dipolar particles ($N = 2$). The size of the constitutive beads is reduced for the sake of clarity.

where $\overleftrightarrow{t}$ is a 3×3 matrix whose three columns are given by the spanning vectors $\vec{a}$, $\vec{b}$, and $\vec{c}$, also denoted in Fig. 8.1. $\vec{n}$ designates a vector with integer components n_x, n_y, n_z, each ranging from $-\infty$ to $+\infty$. The prime in Eq. (8.1) indicates that, when $\vec{n} = 0$, i must be different from j. In order to overcome the slow convergence [221] in Eq. (8.1), an efficient Ewald sum technique adapted to the prism cell was used [222]. The energy scale is set by $U_{\uparrow\uparrow}$, see Eq. (2.10). Thereby, the reduced potential energy of interaction per particle, u, is merely given by $u = \frac{1}{N}\frac{U_{\text{cell}}}{U_{\uparrow\uparrow}}$.

8.3 Method

In what follows, ground states are obtained by minimization procedure [62] called COBYLA, see Section 2.3.1, starting with a generic parallelogram-based prism made up of two particles ($N = 2$). The parallelogram base is generated by the spanning vectors $\vec{a} = a(1, 0, 0)$ and $\vec{b} = b(\cos\gamma, \sin\gamma, 0)$ where $\gamma = \widehat{(\vec{a}, \vec{b})}$. In turn, the prism is generated by the oblique spanning vector $\vec{c} = (c_x, c_y, c_z) = c(\sin\vartheta\cos\varphi, \sin\vartheta\sin\varphi, \cos\vartheta)$ with $\vartheta \equiv \arccos(c_z/c)$ and $\varphi \equiv \arctan(c_y/c_x)$, see

Structure	Standard cell	Energy u
chp (F) $a = b, c$ $\gamma = \frac{\pi}{3}$ $\alpha, \beta \in [\frac{\pi}{3}, \frac{\pi}{2}]$	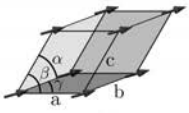	-
bco (F) a, b, c $\alpha = \beta = \gamma = \frac{\pi}{2}$	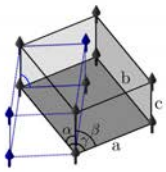	-
bct (F) $a = b = \frac{\sqrt{6}}{2}$ $c = 1$ $\alpha = \beta = \gamma = \frac{\pi}{2}$ $\eta_{\text{bct}} = \frac{2\pi}{9} = 0.698$	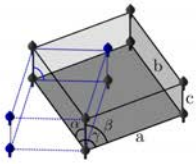	-3.050
hcp (F) $a = b = 1$ $c = 2\sqrt{\frac{2}{3}}$ $\alpha = \beta = \frac{\pi}{2}$ $\gamma = \frac{\pi}{3}$ $\eta_{\text{hcp}} = \frac{\sqrt{2}\pi}{6} = 0.74$	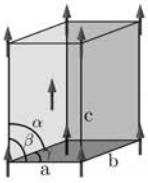	-2.965
fcc (F) $a = b = c = \sqrt{2}$ $\alpha = \beta = \gamma = \frac{\pi}{2}$ $\eta_{\text{fcc}} = \eta_{\text{hcp}}$	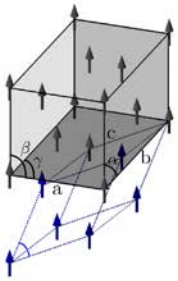	-2.962
hp (AF) $a = b = 1$ $c = 2$ $\alpha = \beta = \frac{\pi}{2}$ $\gamma = \frac{\pi}{3}$ $\eta_{\text{hp}} = \frac{\pi}{3\sqrt{3}} = 0.605$	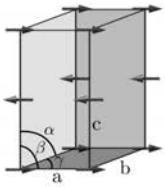	-2.871

Figure 8.2: Clinohexagonal prism (chp) crystal structure and some special relevant limits/cases bco, bct, hcp, fcc, and hp. Corresponding values of the reduced cohesive energy u are provided too. Standard unit cells are in gray and equivalent (special) chp cells for the phases bco, bct, and fcc are represented by blue dashed lines. The characteristic angle of 60° is indicated as well. (F) and (AF) stands for ferromagnetic and antiferromagnetic arrangements, respectively. Lengths (a, b, c) are given in units of the bead diameter d. The packing fractions η_{bct}, $\eta_{\text{hcp}}, \eta_{\text{fcc}}$, η_{hp} of bct, hcp, fcc, hp structures, respectively, are reported too. The constitutive beads are omitted for the sake of clarity.

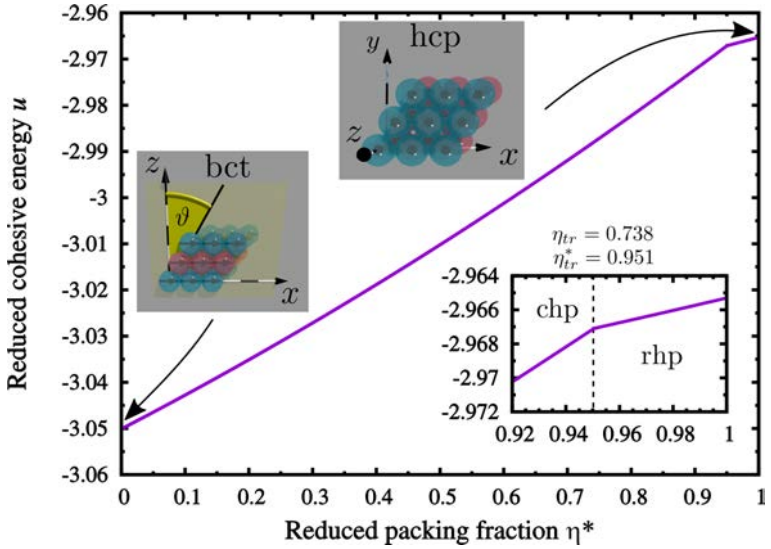

Figure 8.3: Reduced crystal cohesive energy u as a function of the rescaled packing fraction η^*. The two (chp) special/limit structures bct and hcp are illustrated with obliquity $\vartheta = 30°, 0°$, respectively, see also text. The inset is a magnification around the chp/rhp transition occurring close to $\eta^* = 0.951$.

Fig. 8.1. Thereby, ϑ and φ will be referred to as the *prism obliquity* and *prism azimuthal angle*, respectively. At prescribed density, thirteen variables are involved for the system: three for the Cartesian coordinates stemming from the center of one particle (the other one is set at the origin), four for the angular parameters of the dipole moments (θ, ϕ), three for the sidelengths of the cell (a, b and c), and three for the angular parameters of the cell (γ, φ and ϑ). Typically, 10^3-10^4 starting simplex were considered to reach the global minima.

8.4 Dipolar crystal phases

As a major result, *all* the ground states at any density fall within the new clino-hexagonal (chp) phase. The crystal lattices associated with the chp phase has the following properties, see also Fig. 8.2 and inset of Fig. 8.3: The base is hexagonal with spanning vectors $\vec{a} = a(1, 0, 0)$ and $\vec{b} = a(1/2, \sqrt{3}/2, 0)$. On the other hand, the prism is generated by the oblique spanning vector $\vec{c}$ with an obliquity ϑ and azimuthal angle φ. An overview of the relevant dipolar crystal phases can be found in Fig. 8.2. This catalog emphasizes nicely the crucial role and ubiquity of the chp phase in dipolar crystals. Indeed, the chp phase can extrapolate between the bct phase (the overall ground state with $u = -3.050$) and the hcp phase at highest

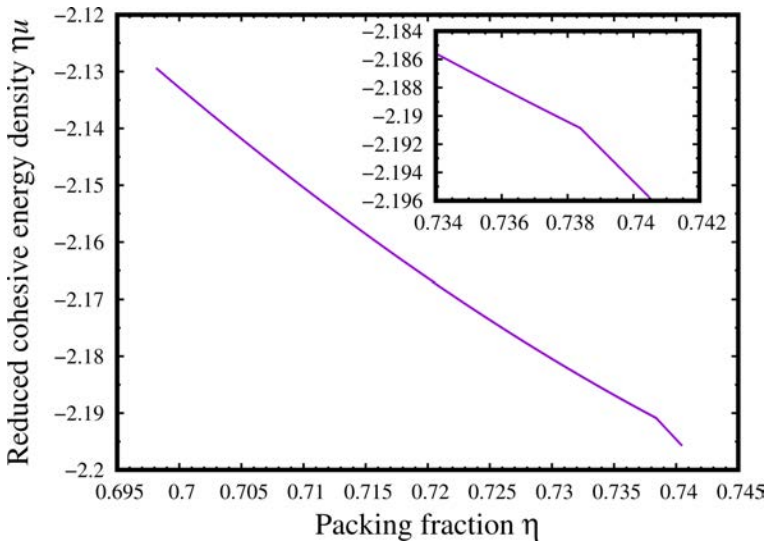

Figure 8.4: Reduced crystal cohesive energy per unit volume ηu as a function of the packing fraction η. The inset is a magnification around the chp/rhp transition occurring at around $\eta = 0.738$.

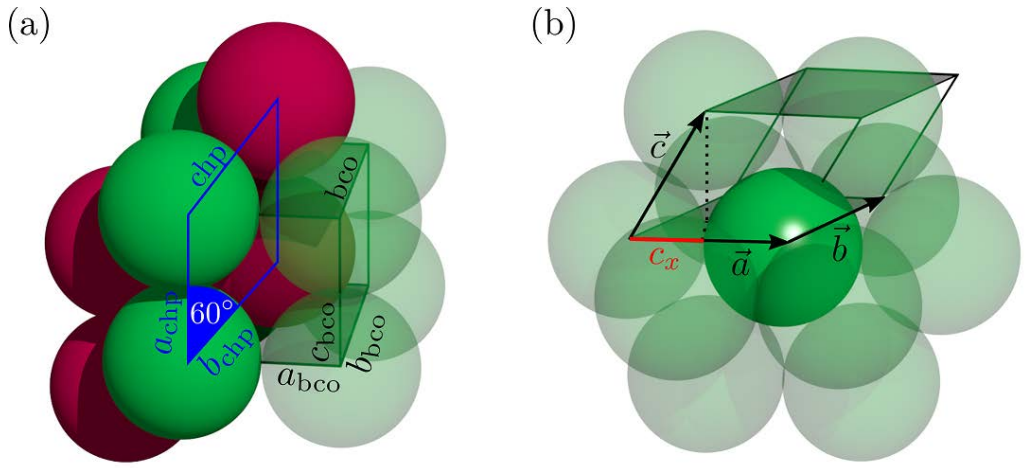

Figure 8.5: (a) Same bco cell as in Fig. 8.2 with the beads shown explicitly. (b) Representation of the ten neighbors surrounding one constitutive bead of the chp cell coinciding with the bco cell.

compaction, see Fig. 8.2. The face-centered cubic (fcc) phase possessing the same packing fraction as that of hcp is slightly beaten by the latter (compare $u = -2.965$ vs -2.962, respectively), see Fig. 8.2. Interestingly, the bco phase turns out to coincide with the chp phase in the ground state of dipolar hard sphere as already evoked. This striking fact is illustrated in Fig. 8.2 and Fig. 8.5(a), where a chp equivalent cell is shown. Similarly, special equivalent chp cells for bct and fcc structures are also provided in Fig. 8.2. For an antiferromagnetic coupling, the hexagonal primitive (hp) structure is the ground state which is the zero-obliquity-limit of the chp crystal structure with $c_x = c_y = 0, c_z = 2$, see Fig. 8.2.

The dependency of the cohesive energy u of the dipolar crystal on the packing fraction η is now analyzed. It is useful to introduce the following rescaled packing fraction η^* defined as

$$\eta^* \equiv \frac{\eta - \eta_{\text{bct}}}{\eta_{\text{hcp}} - \eta_{\text{bct}}}, \tag{8.2}$$

where the values of η_{bct} and η_{hcp} are given in Fig. 8.2. In the absence of external field, as it is the case here, the ground states are always found to be ferromagnetic, where all dipoles point in the same dense direction (except for hcp) as intuitively expected from the picture of assembled ferrochains. In the low packing regime (typically $\eta^* < 0$), a coexistence between the bct phase and its vapor (at infinite dilution) is found. It is to say that if a system is prepared below η_{bct}, it will spontaneously fully condense to the bct crystal and leave accordingly an empty space at zero temperature. These features fully agree with Groh and Dietrich results [239]. This bct-void coexistence was also reported experimentally [12] and by Monte Carlo simulations on electrorheological ER fluids [236]. The situation becomes less simple for denser systems ($\eta^* > 0$), see energy profile $u(\eta^*)$ in Fig. 8.3. Upon increasing the packing fraction, the cohesive energy u increases monotonically and continuously from bct to hcp, see Fig. 8.3. However, there is a first-order transition as signaled by a discontinuity of the derivative of $u(\eta^*)$ at $\eta* = 0.951 =: \eta^*_{\text{tr}}$ corresponding to a packing fraction $\eta_{tr} = 0.738$, see also inset in Fig. 8.3. Thereby, the phase diagram is as follows: (i) Below the transition point $\eta < \eta_{\text{tr}}$, the ground state corresponds to the chp phase with a single particle per unit cell. In that situation, the chp phase corresponds also to a (special) bco crystal and vice versa. (ii) Above the transition point $\eta > \eta_{\text{tr}}$, the ground state corresponds to a *right hexagonal prism* (rhp) phase (which is a limit of chp with zero obliquity)

characterized by two particles per unit cell, see also inset in Fig. 8.3. The inner particle of rhp phase, in the ground state, is found to be located at $z = \vec{c}/2$ whereas the $x-$ and $y-$positions correspond to the center of mass of the hexagonal base, i.e. $(\vec{a}+\vec{b})/3$. In other words, the rhp cell can be seen as a (very slightly) distorted hcp cell. We have analyzed the possibility of density jumps by considering the Maxwell construction in the adequate $(\eta, \eta u)$-plane shown in Fig. 8.4. Doing so, no common tangent is detectable and hence *no phase coexistence* prevails. This result is in qualitative contrast with the phase coexistence reported in [239].

8.5 Geometric order parameters

To deepen our understanding of crystallization of dipolar hard spheres, we have monitored the geometric order parameters of the unit cells as a function of density. In order to take into account the special duality of the bco and chp phases, Fig. 8.6(a) displays the chp obliquity ϑ and the chp azimuthal angle φ, whereas Fig. 8.6(b) shows the sidelengths of the bco unit cell. Below the transition point $\eta < \eta_{\rm tr}$, ϑ and φ increase with η^* indicating a compaction-mediated tilting of the vector $\vec{c}$, see Fig. 8.6(a). The profile of $\vartheta(\eta)$ has a simple geometric interpretation and can be rationalized as follows. In the ground state, the chp structure is found to be close packed with $a = b = c = 1$, see inset of Fig. 8.6(a) and Fig. 8.5(b), as a consequence from the packing fraction

$$\eta = \frac{V_{\rm bead}}{V_{\rm chp\ cell}}, \tag{8.3}$$

ϑ is merely dictated by

$$\vartheta(\eta) = \arccos\left(\frac{\pi}{3\sqrt{3}}\frac{1}{\eta}\right), \tag{8.4}$$

see Fig. 8.6(a). Besides, the ground state at prescribed η is such that each particle possesses ten neighbours (six within a hexagonal layer and four with the two adjacent ones) as illustrated in Fig. 8.5(b). Thus, in the chp representation:

$$c^2 = c_x^2 + c_y^2 + c_z^2 = 1 \tag{8.5}$$

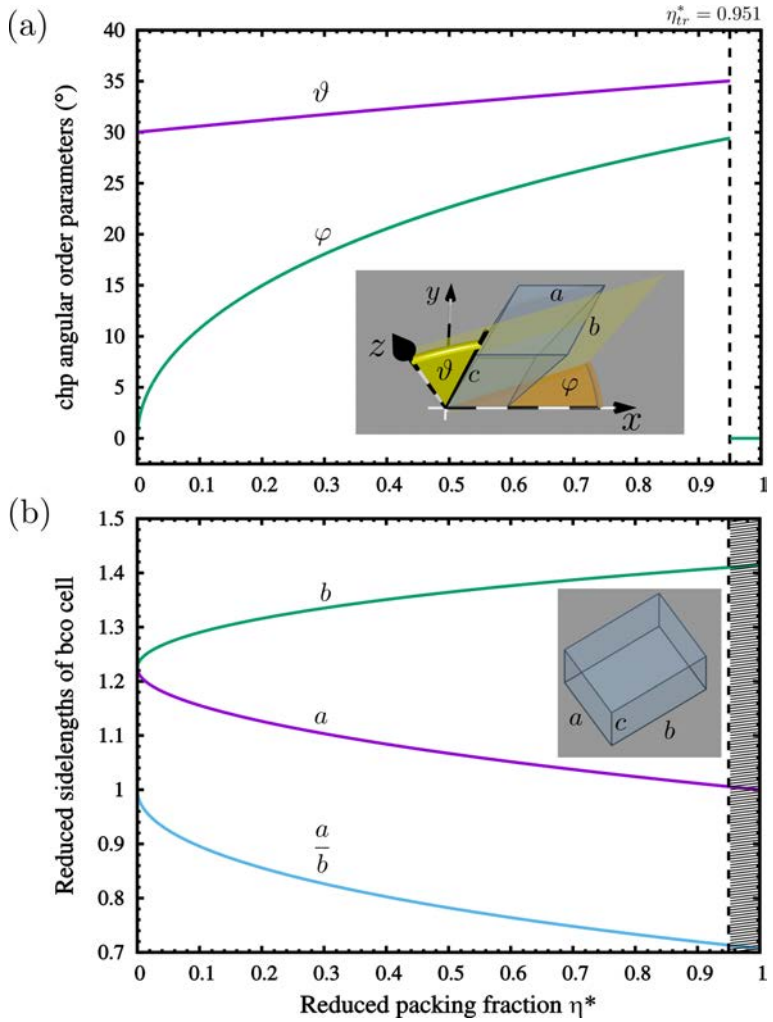

Figure 8.6: (a) Angular order parameters ϑ and φ as a function of the relative packing fraction η^* in the chp representation, see Eqs. (8.4) and (8.6). The inset illustrates ϑ and φ in the chp unit cell. (b) Sidelengths $a, b \geq a, c = 1$ of the bco unit cell, see also inset, as a function of η^*. The shaded region corresponds to $\eta^* > \eta^*_{\mathrm{tr}}$ where the bco phase is beaten by rhp. The profile $a(\eta^*)$, $b(\eta^*)$ and a/b are obtained from Eqs. (8.10a) and (8.10b).

with $c_x = 1/2$, $c_y = \sin\vartheta \sin\varphi$ and $c_z = \cos\varphi$. This feature leads to the following constraint

$$\sin^2\vartheta \sin^2\varphi + \cos^2\vartheta = \frac{3}{4} \tag{8.6}$$

Hence, combining Eqs. (8.4) and (8.6) provide $\varphi(\eta)$ analytically as well:

$$\varphi(\eta) = \arcsin\left(\frac{1}{2}\sqrt{\frac{4\pi^2 - 81\eta^2}{\pi^2 - 27\eta^2}}\right), \tag{8.7}$$

see Fig. 8.6(a). Concomitantly, the ground states coincide with a bco structure polarized along $\vec{c}$ with $c_{\mathrm{bco}} = 1$ and the required angle of 60° between $\vec{c}$ and the bco body diagonal to match an equivalent chp cell involving

$$\tan 60^\circ = \frac{\sqrt{\left(\frac{a_{\mathrm{bco}}}{2}\right)^2 + \left(\frac{b_{\mathrm{bco}}}{2}\right)^2}}{\frac{c_{\mathrm{bco}}}{2}} \tag{8.8}$$

see also Fig. 8.2 and Fig. 8.5(a). Thus the particular sidelengths of the bco structure $a = a_{\mathrm{bco}}$ and $b = b_{\mathrm{bco}}$, see Fig. 8.6(b), must verify

$$a_{\mathrm{bco}}^2 + b_{\mathrm{bco}}^2 = 3. \tag{8.9}$$

Moreover, the packing fraction being given by $\eta = \frac{\pi ab}{3}$ recalling that $c = c_{\mathrm{bco}} = 1$ in the ground state, we arrive at the following expression for the sidelength a and b ($a \leq b$):

$$a = a_{\mathrm{bco}}(\eta) = \sqrt{\frac{3}{2} - \frac{\sqrt{81\eta^2 - 4\pi^2}}{6\eta}}, \tag{8.10a}$$

$$b = b_{\mathrm{bco}}(\eta) = \sqrt{\frac{3}{2} + \frac{\sqrt{81\eta^2 - 4\pi^2}}{6\eta}}, \tag{8.10b}$$

see Fig. 8.6(b). Similar results were obtained by Groh and Dietrich [239] by analyzing close packed bco structures. The physical interpretation of the crystallization under compaction is as follows: $c = 1$ is a signature of chains polarized along $\vec{c}$. These chains self-assemble into hexagonal lattice sheets giving rise to the chp phase that coincides with a unique bco structure at prescribed packing fraction η, see also Fig. 8.2. In the overall ground state ($\eta^* = 0$), the bct state is characterized by a

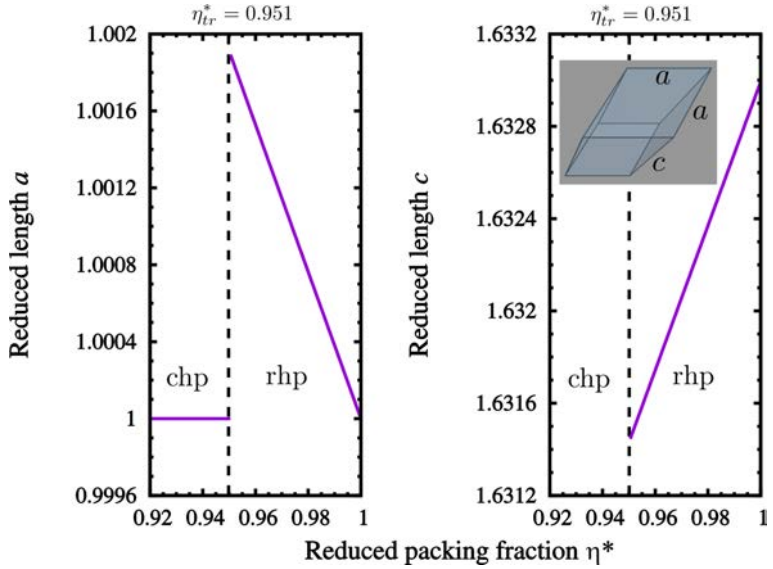

Figure 8.7: Sidelengths behavior of a (left) and c (right), around chp/rhp transition, as a function of η^*. The inset illustrates the corresponding geometric order parameters of the chp cell. Notice that $c = 1$ when $\eta^* < \eta^*_{\rm tr}$, not shown due to the severe difference in length scale variation involved there.

square base ($a = b = \frac{\sqrt{6}}{2} = 1.225$) in the bco representation. Upon compressing the system, the bco cell shrinks by getting elongated from $a/b = 1$ (bct at $\eta^* = 0$) to $a/b = 1/\sqrt{2} = 0.707$ (fcc at $\eta^* = 1$), see Fig. 8.6(b). In the highly packed regime $\eta^* > \eta^*_{\rm tr}$, the rhp phase is characterized by $\vartheta = \varphi = 0$, see Fig. 8.6(a). At the chp/rhp transition ($\eta^* = \eta^*_{\rm tr}$), a strong discontinuity of the angular order parameters is reported, see Fig. 8.6(a).

To have a complete vision of the crystal phase behavior of the system, we also analyze the the sidelengths of the chp and rhp unit cells as a function of density, see Fig. 8.7. Below the transition $\eta^* < \eta^*_{\rm tr}$, $a = b = c = 1$, see Fig. 8.7, showing that the chp structure is close packed where each particle possesses ten touching nearest neighbors. Above the transition $\eta^* > \eta^*_{\rm tr}$, a non-trivial scenario occurs where the hexagonal base $(\vec{a}, \vec{b})$ is no longer close packed as signaled by $a = b$ slightly but non-negligibly larger than unity, see Fig. 8.7. This slight base stretching ($a = b > 1$) is concomitantly accompanied by a little compression of the transverse height ($c < \sqrt{8/3} = 1.633$) when compared to the "ideal" hcp structure, see Fig. 8.7. The non compactness of the hexagonal lattice sheets is however in qualitative agreement with the idea that within a sheet, local dipole-dipole interactions are repulsive due to the (perpendicular) polarization along $\vec{c}$ in the rhp phase. In the

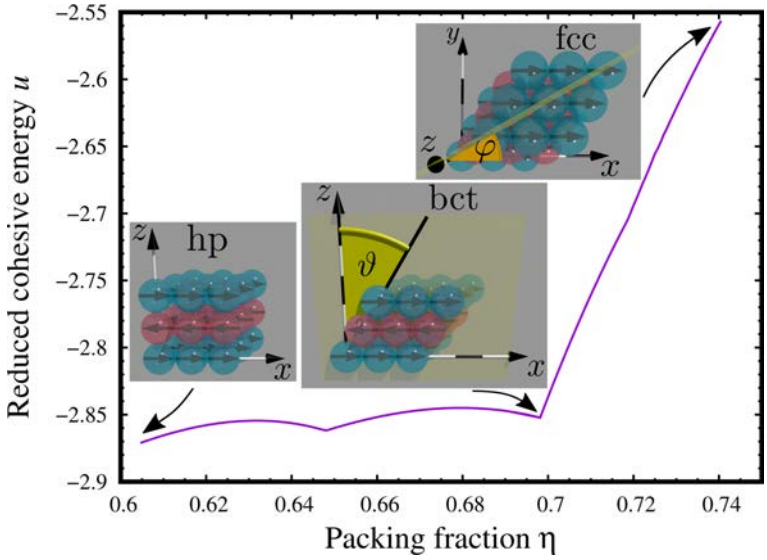

Figure 8.8: Reduced crystal cohesive energy u as a function of the packing fraction η. The three (chp) special/limit structures hp ($\vartheta, \varphi = 0°$), bct ($\vartheta = 30°, \varphi = 0°$) and fcc ($\vartheta = 30°, \varphi = 30°$) are illustrated.

same spirit, a contraction of the height c favors dipole-dipole attractive interactions lying along the (non-touching bead) chains parallel to $\vec{c}$.

As a final result, we briefly discuss the relevance of the chp phase in the *antiferromagnetic* state. In this situation, the unit cell is made up of two opposite dipoles. The complete energy profile at prescribed density is reported in Fig. 8.8. Firstly, we confirm the overall ground state advocated by Lavender et al. [240] two decades ago, namely the hp phase corresponding to the packing fraction η_{hp}, see Fig. 8.2 and Fig. 8.8. Then, when $\eta > \eta_{\text{hp}}$, it is a *pure* chp superlattice that wins with no bco equivalent. Dipoles are always coplanar to the hexagonal lattice sheet where each layer is antiferromagnetically coupled with its two adjacent ones, just as with the hp case, see Fig. 8.2 and Fig. 8.8.

8.6 Concluding remarks

To summarize, we have discovered a new phase, clinohexagonal prism (chp), that provides a unified view on crystallization of dipolar systems at vanishing temperature. At *any* prescribed density (or equivalently packing fraction η) the ground state can always be described by a chp phase with a proper obliquity. Typically, the obliquity increases monotonically when densifying the system below the chp/rhp

transition. If an antiferromagnetic coupling is imposed, say due to an external spatially varying E/B-field, then the overall ground state is the hexagonal primitive (hp) phase. At larger densities ($\eta > \eta_{\rm hp}$), ground states consist of *pure* chp structures (with finite obliquity) that have *no* common bco structures.

This work should be helpful to predict and/or to explain at some extend the phase behavior encountered in experimental dipolar systems such as ferrofluids [241], self-assembly of magnetic magnetite nanoparticles [10], or electrorheological fluids [12, 242]. In this respect, it would be interesting to investigate in a future work the stability/evolution of the chp phase when subject to a biaxial electric or magnetic field [101, 163]. The role of the chp phase should also be relevant in solid-solid transitions such as colloidal martensitic ones where stacked hexagonal layers structures set in [243, 244].

On the theoretical side, this discovery should trigger new interest in the crystal structure prediction ranging from molecular materials to colloidal/granular systems. Indeed, a future robust work should from now on include this phase to assess the veracity of the predicted ground states, especially when bco/hcp or bco/hp phase boundaries are involved. In this respect, the possible occurrence of the chp phase will play a decisive role in better understanding the phase behavior (in the low entropy limit [2]) of closely related model dipolar fluids [236, 239, 245, 246, 247, 248], ionic microgels [249, 250], or star polymers solutions [251].

[2] Given the fact that bco and chp phases coincide in the ground state at intermediate densities, it is expected that both phases can emerge at *finite temperature* due to the tiny cohesive energy difference there. For similar reasons, rhp/hcp and fcc phases can both emerge at high densities.

Chapter 9

Conclusion and perspectives

We have seen that self-assembly is the spontaneous organization of a system due to interactions between pre-existing components. Besides fascinating and intriguing human being, the magnetic interactions offer a way to guide the self-assembly and develop new technologies in many fields (e.g. medicine and nanotechnology). Some self-assembling processes in biological world rely also on dipolar particles (e.g. magnetosome chain and alpha helix). In that respect, it is crucial to understand how dipolar particles interact and assemble. To reach this objective, the first part of this thesis has been dedicated to dipolar chains which are the most simple and common self-assembled ordered structure. In a second part, the aggregation of dipolar particles into crystal structures which is primordial to build functional materials has been addressed.

As far as dipolar chains are concerned, an original approach involving dipolar filaments is considered. In this approach, the understanding of interacting needles was important to grasp that of dipolar chains. There, a relevant softening at short separation sets in. However, at very short separation (comparable to the bead size) the chain-chain interaction exhibits a remarkable hardening due to the discrete nature of the chains. On the other hand, the regime where the two dipolar chains are touching has received attention as well. Thereby, a remarkable non-trivial oscillatory behavior depending on the shift between the two chains has been observed. The lowest energies have been found when dipolar chains are out-of-registry. Such a trend has been recovered in a subsequent work dealing with the columnar aggregation of dipolar (infinite) chains. Indeed, bundles of dipolar chains in zipper configuration with narrow sections and underlying body-centered tetragonal lattice have emerged from our minimization calculations. In addition, the bundles of dipolar chains with a square section or a rectangular one (whose the aspect ratio is close to unity) display a remarkable stability (i.e., low-energy ground states). Additional calculations on bundles of chains of finite size have also indicated that these chains need to be long enough (few hundred beads) to recover the qualita-

tive features of the infinite limit. Our findings should be helpful to rationalize and to explain experimentally observed ribbons formation of magnetic chains. Dipolar linear chains, then zigzag chains have been successfully used as limiting cases to capture the main features of interacting helical chains. It was shown that linear as well as zigzag chains allowed a precise and clear description of the mechanisms of the ferromagnetic/antiferromagnetic (i.e., chains with parallel/opposite dipoles) transitions. Moreover, a similar behavior has been noticed between: (i) the non-monotonic energy profile stemming from the single zigzag case (as a function of its compaction) and (ii) the energy profile of the interacting zigzags as a function of their separation distance (at prescribed compaction). It was also found the the linear chain is energetically beaten only for highly compress zigzag chains. Concerning the helical chains, two main regimes have been identified depending on their radius. When the helix radius is large enough (comparable to the bead size), the ground state is found to be concentric. Conversely, when the helix radius is small enough, the ground state is found to be non-concentric. The profiles of the overall ground state energy as a function of the helix pitch (i.e., the compression of the helix) for the single and the double helical chain turned out to be very similar. In addition, if the pitch is not too small, single and double helical chains exhibit the same dipole moment distribution.

The crystallization matter has been the main subject of the second part of this manuscript. In particular, two-dimensional confinement has been addressed through two investigations: (i) sedimentation experiments of (repulsive) *superparamagnetic* colloids in a monolayer and (ii) layered (attractive) ferromagnetic particles in an external magnetic field. An original sedimentation experiment with dipolar particles in a tilted monolayer and subject to a perpendicular external field has been realized and also mimicked in Monte Carlo simulations. In conjunction, we have successfully developed a simple density functional theory approach based on a zero-temperature local density approximation. Indeed, an excellent agreement has been obtained with the density profiles stemming from the experiments and simulations. Simulations have been insightful upon providing more details on the crystallization properties of the equilibrium structure. Especially, the vivid oscillations in density profiles have shown that the lattice constant of the crystal formed near the container's bottom roughly obeys a very simple power law reflecting the force balance between gravity and dipolar interaction. Coming to the layered (attractive) ferromagnetic particles in an external magnetic field, an exact analytical solution is

found. There, we were in position to describe exactly and analytically the crystal ground state as a function of the magnitude of the applied perpendicular external magnetic field. The latter expressions have been established relaying on lattice symmetries revealed by our preliminary numerical minimization. As a major results, we have discovered that the hexagonal lattice as well as the continuous degeneracy of the ferromagnetic state are broken when an external perpendicular magnetic field is applied. In strong contrast, we have seen that the bilayer system provides more stability since the hexagonal superlattice of each of the two constitutive layers is invariant under external magnetic field. Moreover, the bilayer's superlattice coincides with the body-centered tetragonal lattice which corresponds to the bulk ground state. Bulk crystallization of dipolar particles was also in the scope of this thesis. A new phase has been discovered which consists of an oblique prismatic lattice with a hexagonal base called clinohexagonal prism. Our calculations have demonstrated that this new phase describes all the ground states of dipolar hard spheres prepared at any density. The ability of the clinohexagonal prism phase to extrapolate from the body-centered tetragonal phase to the hexagonal close-packed provides a unified and clarified view of freezing and solid-solid transitions in dipolar systems at vanishing temperature.

All these related findings should help to deeper understand the intimate physical mechanisms involved in the self-assembly of dipolar particles. Besides, these results rationalize recent experimental observations. Moreover our findings should open a whole new range of possibilities to pursue further investigations. For instance, the study of dipolar chains provides an excellent starting point to probe confinement effect (e.g. by means of a cylinder) and/or gravity effect on self-assembly of dipolar hard spheres. Concerning our investigations on the sedimentation-mediated crystallization, the density functional theory developed to describe the density profiles in sedimentation experiments does not reproduce the vivid oscillations revealed by the computer simulations. As a consequence, a future density functional theory with the ability to account for the oscillating density profiles near by the bottom of the container would be a significant achievement. Larger distortions of the lattice of the monolayer made up of ferromagnetic (attractive) particles under external magnetic field might be experimentally observed due to energy barriers. Except the sedimentation study, we have only dealt with athermal systems. In that respect, studies including finite temperature could be very promising. For instance, it would be interesting to check if the body-centred orthorgonal/clinohexagonal prism coex-

istence in the bulk prevails. In a more fundamental perspective, the phase diagram of dipolar particles in one-dimensional should be advocated. Notice that in this thesis, we have only considered one-component system, but the relatively unexplored binary mixtures should reveal a rich and complex phase behavior.

Appendix A

SLSQP algorithm

A.1 Nonlinear programming problem

The Sequential Least SQuares Programming (SLSQP) algorithm including the Fortran source code has been published by Kraft in 1994 [252, supplements] on the basis of its own technical report previously issued in 1988 [60]. Only the main features of the SLSQP algorithm will be summarized in this section, for further details, refer to the Kraft's technical report [60] used as guideline for this appendix. The SLSQP algorithm belongs to the class of methods for optimization problems called sequential quadratic programming (SQP). The SQP methods have been introduced for the first time by Wilson in 1963 [253] to treat constrained nonlinear optimization problems. Since then, the SQP methods have been gradually developed to become one of the most popular ways to solve nonlinear optimization problems. The success of these methods is mainly due to its remarkable efficiency for a wide range of optimization problems and especially its ability to handle robustly the optimization problems with both the inequality and the equality constraints. A nonlinear programming problem (NLP) with constraints may be written in the general form as [60, p. 8] [254, p. 421]

$$\min_{\vec{x}\in\mathbb{R}^n} f(\vec{x}) \tag{A.1a}$$

$$\text{subject to } g_j(\vec{x}) = 0, \quad j = 1, ..., m_{eq}, \tag{A.1b}$$

$$g_j(\vec{x}) \geq 0, \quad j = m_{eq} + 1, ..., m, \tag{A.1c}$$

$$l_i \leq x_i \leq u_i, \quad i = 1, ..., n, \tag{A.1d}$$

where $f : \mathbb{R}^n \to \mathbb{R}$ relating to the objective function and $g : \mathbb{R}^n \to \mathbb{R}^m$ relating to the constraints are smooth functions. The number of equality constraints m_{eq}, the total number of constraints m and the number of variables n are integers. The values l_i and u_i are the lower and upper bounds on the variables x_i.

A.2 Line search strategy

Basically, the SQP methods rest on the line search strategy, that is solving iteratively the optimization problem from an initial guess $\vec{x}^0$ for the solution and then using a search direction $\vec{p}$ to reduce the objective function $f(\vec{x})$ in Eq. (A.1a). In each iteration, a new vector solution $\vec{x}^{k+1}$ is obtained from the current vector $\vec{x}^k$ according to the relation [60, p. 9] [254, p. 30]

$$\vec{x}^{k+1} = \vec{x}^k + \alpha^k \vec{p}^k, \tag{A.2}$$

where $\vec{p}^k$ and α^k are the search direction and the step length at the k^{th} iteration, respectively.

A.3 Quadratic programming problem

The SQP methods can be seen as the Newton's method applied to the Karush-Kuhn-Tucker (KKT) optimality conditions of the NLP problem in Eq. (A.1) [254, p. 321]

$$\vec{\nabla}_{\vec{x}} \mathcal{L}(\vec{x}^*, \vec{\lambda}^*) = 0 \tag{A.3a}$$

$$g_j(\vec{x}^*) = 0, \quad j = 1, ..., m_{eq}, \tag{A.3b}$$

$$g_j(\vec{x}^*) \geq 0, \quad j = m_{eq} + 1, ..., m, \tag{A.3c}$$

$$\lambda_j^* \geq 0, \quad j = m_{eq} + 1, ..., m, \tag{A.3d}$$

$$\lambda_j^* g_j(\vec{x}^*) = 0, \quad j = 1, ..., m, \tag{A.3e}$$

where $\mathcal{L}(\vec{x}^*, \vec{\lambda}^*)$ is the Lagrange function at the optimum point $\vec{x}^*$ associated with the optimum Lagrange multiplier vector $\vec{\lambda}^*$ according to the relation

$$\mathcal{L}(\vec{x}^*, \vec{\lambda}^*) = f(\vec{x}^*) - \sum_{j=1}^{m} \lambda_j^* g_j(\vec{x}^*). \tag{A.4}$$

Another (and more transparent) way to explain the SQP methods is to make a quadratic approximation of the Lagrange function $\mathcal{L}(\vec{x}, \vec{\lambda})$ in Eq. (A.4) and a linear approximation of the constraints $g_j(\vec{x})$ in Eq. (A.1b) and Eq. (A.1c). Both approaches lead to transform the initial problem in Eq. (A.1) (NLP) into a quadratic

programming (QP) subproblem of the following form [60, p. 9] [254, p. 533]:

$$\min_{\vec{p}\in\mathbb{R}^n} \frac{1}{2}\vec{p}^T \overleftrightarrow{B}(\vec{x},\vec{\lambda})\vec{p} + \vec{\nabla}_{\vec{x}} f(\vec{x})\vec{p} + f(\vec{x}) \tag{A.5a}$$

$$\text{subject to } \vec{\nabla}_{\vec{x}} g_j(\vec{x})\vec{p} + g_j(\vec{x}) = 0, \quad j = 1, ..., m_{eq}, \tag{A.5b}$$

$$\vec{\nabla}_{\vec{x}} g_j(\vec{x})\vec{p} + g_j(\vec{x}) \geq 0, \quad j = m_{eq}+1, ..., m, \tag{A.5c}$$

where $\overleftrightarrow{B}(\vec{x},\vec{\lambda}) = \vec{\nabla}^2_{\vec{x}\vec{x}}\mathcal{L}(\vec{x},\vec{\lambda})$ is the Hessian matrix. Note that the last term $f(\vec{x})$, being a constant, can be latter ignored. Upon inspecting the Eqs. (A.2) and (A.5), at the k^{th} iteration, three parameters ($\alpha, \vec{p}$ and $\vec{\lambda}$) are needed to obtain an updated vector $\vec{x}^{k+1}$ in the SQP methods. Obviously, there are as many varieties of SQP methods as possibilities to determine these three parameters [254, Chapter 18].

A.4 The search direction

The SLSQP approach starts with the LDL^T-factorization [255] of the Hessian matrix $\overleftrightarrow{B}(\vec{x}^k,\vec{\lambda}^k)$. Doing so, the QP subproblem in Eq. (A.5) can be transformed into the following Linear least Squares with Equality and Inequality constraints (LSEI) subproblem [60, p. 13]:

$$\min_{\vec{p}\in\mathbb{R}^n} \| \overleftrightarrow{D}^{1/2} \overleftrightarrow{L}^T \vec{p} + \overleftrightarrow{D}^{-1/2} \overleftrightarrow{L}^{-1} \vec{\nabla}_{\vec{x}} f(\vec{x}) \| \tag{A.6a}$$

$$\text{subject to } \vec{\nabla}_{\vec{x}} g_j(\vec{x})\vec{p} + g_j(\vec{x}) = 0, \quad j = 1, ..., m_{eq}, \tag{A.6b}$$

$$\vec{\nabla}_{\vec{x}} g_j(\vec{x})\vec{p} + g_j(\vec{x}) \geq 0, \quad j = m_{eq}+1, ..., m, \tag{A.6c}$$

where $\overleftrightarrow{L}$ is a lower triangular matrix and $\overleftrightarrow{D}$ is a diagonal matrix. After appropriate successive variables changes and a reduced QR factorization, doing so, the SLSQP approach is in a position to provide the search direction $\vec{p}$ verifying Eq. (A.5), see Refs. [60, pp. 21 ff] and [61, pp. 158 ff].

A.5 The step length

Notice that by setting the step length to the unity ($\alpha = 1$), the global convergence is ensured only if the starting point is near a local optimum, otherwise an erratic behavior of the algorithm may occur. In order to guarantee a global convergence of the SLSQP algorithm, the step length α needs to be adjusted by using the so-called

ℓ_1 merit function [60, p. 10] [254, p. 540] defined as

$$\varphi(\vec{x}^k, \vec{\lambda}^k) = f(\vec{x}^k) + \sum_{j=1}^{m_{eq}} \rho_j^k(\vec{\lambda}^k)|g_j(\vec{x}^k)| + \sum_{j=m_{eq}+1}^{m} \rho_j^k(\vec{\lambda}^k)|\min(0, g_j(\vec{x}^k))| \quad \text{(A.7)}$$

with the penalty parameters

$$\rho_j^k(\vec{\lambda}^k) = \max\left(\frac{\rho_j^{k-1} + |\lambda_j^k|}{2}, |\lambda_j^k|\right), \quad \text{(A.8)}$$

knowing that the starting parameters ρ_j^0 can be set to zero. Since $\vec{\lambda}^k$ and $\vec{p}^k$ are now known at this stage, the step length α^k is obtained by minimization of the merit function $\varphi(\vec{x}^k + \alpha^k \vec{p}^k, \vec{\lambda}^k)$ via a modified version of Brent's method [256].

A.6 The Hessian matrix

The calculation of the Hessian matrix $\overleftrightarrow{B}(\vec{x}^k, \vec{\lambda}^k)$ in Eq. (A.5) requires to compute the second derivatives of the Lagrange function, that is, those of the objective function and the constraints in Eq. (A.4). For computational efficiency reasons and because it is also sometimes complicated to obtain the second derivative expressions, resort to the Broyden, Fletcher, Goldfarb and Shanno (BFGS) approximation can be useful. The BFGS approximation consists in updating the $\overleftrightarrow{B}^k = \overleftrightarrow{B}(\vec{x}^k, \vec{\lambda}^k)$ matrix by following the relation [60, p. 11] [254, p. 536]

$$\overleftrightarrow{B}^{k+1} = \overleftrightarrow{B}^k + \frac{\vec{q}^k (\vec{q}^k)^T}{(\vec{q}^k)^T \vec{s}^k} - \frac{\overleftrightarrow{B}^k \vec{s}^k (\vec{s}^k)^T \overleftrightarrow{B}^k}{(\vec{s}^k)^T \overleftrightarrow{B}^k \vec{s}^k} \quad \text{(A.9)}$$

with

$$\vec{s}^k = \vec{x}^{k+1} - \vec{x}^k = \alpha^k \vec{d}^k, \quad \text{(A.10a)}$$

$$\vec{q}^k = \theta^k \vec{\eta}^k + (1 - \theta^k) \overleftrightarrow{B}^k \vec{s}^k, \quad \text{(A.10b)}$$

$$\vec{\eta}^k = \vec{\nabla}_{\vec{x}} \mathcal{L}(\vec{x}^{k+1}, \vec{\lambda}^k) - \vec{\nabla}_{\vec{x}} \mathcal{L}(\vec{x}^k, \vec{\lambda}^k), \quad \text{(A.10c)}$$

$$\theta^k = \begin{cases} 1, & (\vec{s}^k)^T \vec{\eta}^k \geq 0.2 (\vec{s}^k)^T \overleftrightarrow{B}^k \vec{s}^k, \\ \dfrac{0.8 (\vec{s}^k)^T \overleftrightarrow{B}^k \vec{s}^k}{(\vec{s}^k)^T \overleftrightarrow{B}^k \vec{s}^k - (\vec{s}^k)^T \vec{\eta}^k} & (\vec{s}^k)^T \vec{\eta}^k < 0.2 (\vec{s}^k)^T \overleftrightarrow{B}^k \vec{s}^k. \end{cases} \quad \text{(A.10d)}$$

Appendix B

Layered dipolar particles in external magnetic field: Analytical expressions

B.1 Monolayer in external field

When we have considered the case of a monolayer in an external perpendicular magnetic field, preliminary numerical minimization has revealed two major symmetries. The monolayer's lattice is always rhombic (i.e., $\|\vec{a}\| = \|\vec{b}\|$) and the phase is a ferromagnetic state, see Chapter 7. To obtain an analytical description of the problem, it is useful to choose the y-axis (or equivalently x-axis) to coincide with the bisector of $\widehat{(\vec{a},\vec{b})}$, see Fig. B.1. Thereby, the dipole moment $\vec{m}$ forms an angle α with the y-axis, so that $\vec{m} = (m_\rho \sin\alpha, m_\rho \cos\alpha, m_z)$ with $m^2 = m_\rho^2 + m_z^2 = 1$, see Fig. B.1. Within this framework and after some lengthy algebra, one arrives at the following exact expression for the energy per particle at prescribed rhombicity γ:

$$u(m_z, \gamma, \alpha; B) = S_1(\gamma) + \cos(2\alpha) S_2(\gamma)(1 - m_z^2) - 3S_1(\gamma) m_z^2 - B m_z \tag{B.1}$$

with

$$\begin{aligned} S_1(\gamma) = &- \frac{1}{16\left(\cos(\gamma/2)\right)^3} \left\{ \zeta(3) + \frac{4\pi^2}{3\left(\tan(\gamma/2)\right)^2} \right. \\ &+ \frac{8\pi}{\tan(\gamma/2)} \sum_{n=1}^{\infty} \sum_{u=1}^{\infty} \left[\frac{n}{u} K_1\left(2\pi \tan(\gamma/2) n u\right) \right. \\ &\left. \left. + \frac{n\cos(n\pi)}{u - 1/2} K_1\left(2\pi \tan(\gamma/2) n\left(u - 1/2\right)\right) \right] \right\} \end{aligned} \tag{B.2}$$

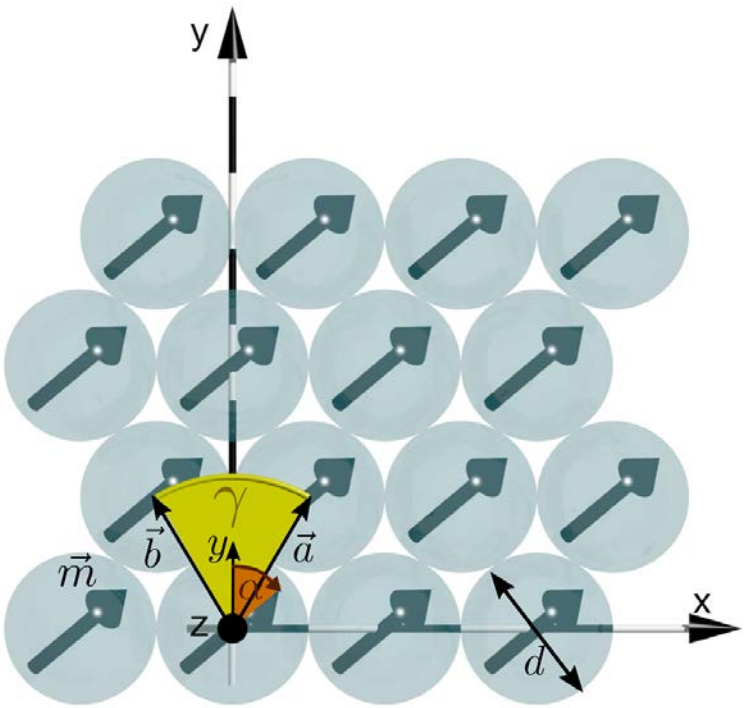

Figure B.1: Sketch of the geometric setup for an infinite monolayer in a perpendicular magnetic field where the bisector of $\widehat{(\vec{a},\vec{b})}$ coincides with the y-axis.

and

$$\begin{aligned} S_2(\gamma) = &-\frac{1}{16\left(\cos(\gamma/2)\right)^3}\left\{3\zeta(3) - \frac{4\pi^2}{3\left(\tan(\gamma/2)\right)^2}\right. \\ &- 8\pi^2 \sum_{n=1}^{\infty}\sum_{u=1}^{\infty}\Big(n^2\left[K_2\left(2\pi\tan(\gamma/2)nu\right) + 3K_0\left(2\pi\tan(\gamma/2)nu\right)\right] \\ &+ n^2\cos(n\pi)\left[K_2\left(2\pi\tan(\gamma/2)n(u-1/2)\right)\right. \\ &\left.\left. + \ 3K_0\left(2\pi\tan(\gamma/2)n(u-1/2)\right)\right]\Big)\right\}. \end{aligned} \tag{B.3}$$

B.1.1 General expressions for the ground state

One can shows $S_2 < 0$ with $60° < \gamma < 120°$. Hence, in the ground state $\alpha = 0°$ in Eq. (B.1). For the hexagonal case $\gamma = 60°$ (or equivalently 120°), we have $S_2 = 0$ so that α is arbitrary demonstrating the continuous degeneracy of the dipole moment in the hexagonal ground state. In general, in all cases, the total energy per particle of the monolayer can be cast into the form

$$u_{\text{monolayer}}(m_z,\gamma;B) = E_0^{\text{monolayer}}(\gamma) + E_1^{\text{monolayer}} m_z + E_2^{\text{monolayer}}(\gamma)\, m_z^2 \tag{B.4}$$

with

$$E_0^{\text{monolayer}}(\gamma) = S_1 + S_2 \tag{B.5}$$

$$= -\frac{1}{4\left(\cos(\gamma/2)\right)^3}\Big\{\zeta(3) - 8\pi^2 \sum_{n=1}^{\infty}\sum_{u=1}^{\infty}\Big[n^2 K_0\left(2\pi\tan(\gamma/2)nu\right) + n^2\cos(n\pi)K_0\left(2\pi\tan(\gamma/2)n(u-1/2)\right)\Big]\Big\} \tag{B.6}$$

$$E_1^{\text{monolayer}} = -B \tag{B.7}$$

$$E_2^{\text{monolayer}}(\gamma) = -3S_1 - S_2 \tag{B.8}$$

$$\begin{aligned} =&\frac{1}{8\left(\cos(\gamma/2)\right)^3}\Big\{3\zeta(3) + \frac{4\pi^2}{3\left(\tan(\gamma/2)\right)^2} \\ &+ 8\pi^2\sum_{n=1}^{\infty}\sum_{u=1}^{\infty}\Big(n^2\left[K_2\left(2\pi\tan(\gamma/2)nu\right) - 3K_0\left(2\pi\tan(\gamma/2)nu\right)\right] \\ &+ n^2\cos(n\pi)\left[K_2\left(2\pi\tan(\gamma/2)n(u-1/2)\right)\right. \\ &\left. - 3K_0\left(2\pi\tan(\gamma/2)n(u-1/2)\right)\right]\Big)\Big\}. \end{aligned} \tag{B.9}$$

where $\zeta(3)$ is a zeta function, $K_0(r)$ and $K_2(r)$ are modified Bessel functions of the second kind. By minimizing the energy given in Eq. (B.4) with respect to m_z ($\frac{\partial u}{\partial m_z}\Big|_B = 0$), we obtain the magnetization

$$m_z(\gamma; B) = \frac{B}{2E_2^{\text{monolayer}}(\gamma)} \tag{B.10}$$

and consequently the total energy

$$u_{\text{monolayer}}(\gamma; B) = E_0^{\text{monolayer}}(\gamma) - \frac{B^2}{4E_2^{\text{monolayer}}(\gamma)}. \tag{B.11}$$

At prescribed magnetic field B, further minimization of Eq. (B.4) with respect to γ ($\frac{\partial u}{\partial \gamma}\Big|_B = 0$) provides a value $\gamma = \gamma^*$, leading to the final ground state

$$u_{\text{monolayer}}^{\min}(B) = E_0^{\text{monolayer}}(\gamma^*(B)) - \frac{B^2}{4E_2^{\text{monolayer}}(\gamma^*(B))} \tag{B.12}$$

and magnetization

$$m_z(B) = \frac{B}{2E_2^{\text{monolayer}}(\gamma^*(B))}. \tag{B.13}$$

B.1.2 Hexagonal lattice approximation (HLA)

If we neglect the rhombicity and always assume a perfect hexagonal lattice for the ground state, Eq. (B.4) becomes

$$u_{\text{monolayer}}(m_z; B) = E_0^{\text{monolayer}}(60^\circ) + E_1^{\text{monolayer}} m_z + E_2^{\text{monolayer}}(60^\circ)\, m_z^2. \quad \text{(B.14)}$$

With this approximation the corresponding minimal energy reads

$$u_{\text{monolayer}}^{\text{HLA}}(B) = E_0^{\text{monolayer}}(60^\circ) - \frac{B^2}{4E_2^{\text{monolayer}}(60^\circ)} \quad \text{(B.15)}$$

and the related magnetization is

$$m_z(B) = \frac{B}{2E_2^{\text{monolayer}}(60^\circ)} = \chi B \quad \text{(B.16)}$$

with $\chi = \dfrac{1}{2E_2^{\text{monolayer}}(60^\circ)} = 0.0604183.$

B.1.3 Solid/Gas transition

The critical value of the magnetic field B_{tr} where the crystal phase is beaten by the gas one is given by the condition

$$u_{\text{monolayer}}^{\min}(B_{\text{tr}}) = u_{gas} = -B_{\text{tr}}. \quad \text{(B.17)}$$

By solving Eq. (B.17), we find

$$B_{\text{tr}} = -u_{\text{monolayer}}^{\min}(\gamma_{\text{tr}}^*, B_{\text{tr}}) \approx 3.0391119, \quad \text{(B.18)}$$

$$\gamma_{\text{tr}}^* \approx 61.1212. \quad \text{(B.19)}$$

Notice that the energy difference between the deformed lattice and the ideal one is small but not negligible. For instance

$$u_{\text{monolayer}}^{\min}(B_{\text{tr}}) = -3.0391119, \quad \text{(B.20)}$$

$$u_{\text{monolayer}}^{\text{HLA}}(B_{\text{tr}}) = -3.0375619. \quad \text{(B.21)}$$

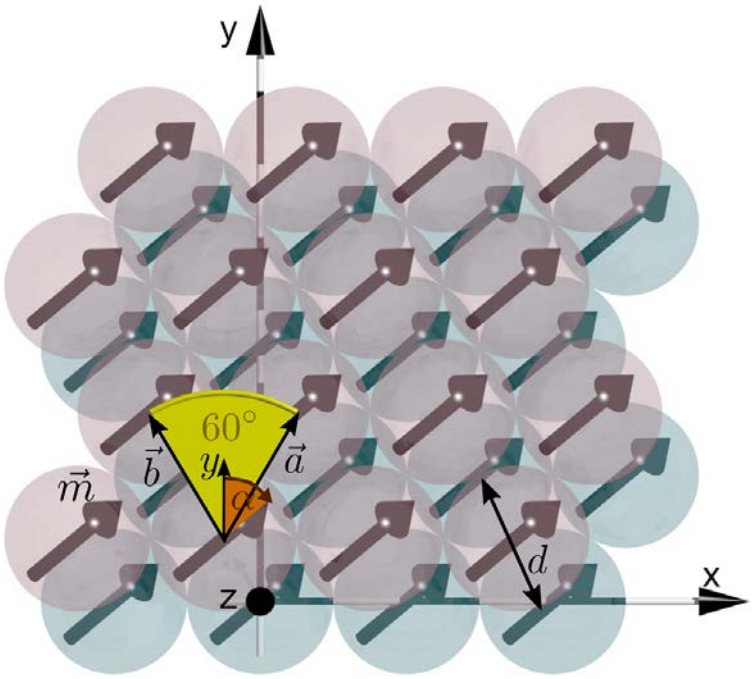

Figure B.2: Sketch of the geometric setup for an infinite bilayer in a perpendicular magnetic field where the bisector of $\widehat{(\vec{a},\vec{b})}$ is parallel to the y-axis.

B.2 Bilayer in external field

In the case of a bilayer in a external perpendicular magnetic field, preliminary numerical minimization has shown that the lattice of each of both constitutive layers is hexagonal (i.e., $\gamma = 60°$) in the ground state, see Chapter 7 and also Fig. B.2. In addition, the bilayer's supperlattice coincides with the body-centered tetragonal lattice and the phase is a ferromagnetic state, see Chapter 7 and also Fig. B.2. Similarly to the monolayer case, we choose the y-axis (or equivalently x-axis) parallel to the bisector of $\widehat{(\vec{a},\vec{b})}$, see Fig. B.2. Within this framework, the energy per particle reads

$$u_{\text{bilayer}}(m_z, \alpha; B) = 2u_{\text{monolayer}}(m_z; B) + u_{\text{interlayer}}(m_z, \alpha; B) \tag{B.22}$$

where $u_{\text{monolayer}}(m_z; B)$ is given by Eq. (B.14) and the energy between the two interacting layers represents

$$u_{\text{interlayer}}(m_z; B) = -\frac{1}{2}(I_1 + I_2(\alpha)) \tag{B.23}$$

with

$$\begin{aligned} I_1 =& \frac{32\pi}{3\sqrt{3}} \sum_{n=1}^{\infty} \sum_{m=-\infty}^{\infty} \frac{n\cos(\frac{3n\pi}{2})}{\sqrt{1+\frac{1}{3}(2m-\frac{3}{2})^2}} K_1\left(n\pi\sqrt{1+\frac{1}{3}(2m-\frac{3}{2})^2}\right) \\ &+ \frac{8}{3}\pi\tanh\left(\sqrt{3}\pi\right) \end{aligned} \tag{B.24}$$

and

$$I_2(\alpha) = -3\left[3m_0^2\cos^2(\alpha)D_1 + \frac{m_0^2\sin^2(\alpha)}{4}D_2 + \frac{3m_z^2}{4}D_3 - \frac{\sqrt{3}m_0^2}{2}\sin(2\alpha)D_4\right] \tag{B.25}$$

where

$$\begin{aligned} D_1 =& \frac{32\pi}{27\sqrt{3}} \sum_{m=-\infty}^{\infty} \sum_{n=1}^{\infty} \cos\left(\frac{n\pi}{2}\right) \left[-n^2 K_0\left(n\pi\sqrt{1+\frac{1}{3}(2m-\frac{1}{2})^2}\right)\right. \\ &\left. + \frac{nK_1\left(n\pi\sqrt{1+\frac{1}{3}(2m-\frac{3}{2})^2}\right)}{\sqrt{1+\frac{1}{3}(2m-\frac{3}{2})^2}}\right] + \frac{8\pi}{27}\tanh\left(\sqrt{3}\pi\right), \end{aligned} \tag{B.26}$$

$$\begin{aligned} D_2 =& \frac{128\pi^2}{27\sqrt{3}} \sum_{m=-\infty}^{\infty} \frac{(2m-\frac{1}{2})^2}{1+\frac{1}{3}(2m-\frac{1}{2})^2} \sum_{n=1}^{\infty} n^2\cos\left(\frac{n\pi}{2}\right) K_2\left(n\pi\sqrt{1+\frac{1}{3}(2m-\frac{1}{2})^2}\right) \\ &+ \frac{16\pi}{9\sqrt{3}}\left[6\pi + \sqrt{3}\sinh(2\sqrt{3}\pi)\right]\operatorname{sech}^2\left(\sqrt{3}\pi\right), \end{aligned} \tag{B.27}$$

$$\begin{aligned} D_3 =& \frac{128\pi^2}{27\sqrt{3}} \sum_{m=-\infty}^{\infty} \frac{1}{1+\frac{1}{3}(2m-\frac{1}{2})^2} \sum_{n=1}^{\infty} n^2\cos\left(\frac{n\pi}{2}\right) K_2\left(n\pi\sqrt{1+\frac{1}{3}(2m-\frac{1}{2})^2}\right) \\ &+ \frac{32\pi}{27\sqrt{3}}\left[-3\pi\operatorname{sech}^2\left(\sqrt{3}\pi\right) + \sqrt{3}\tanh(\sqrt{3}\pi)\right], \end{aligned} \tag{B.28}$$

$$D_4 = -\frac{64\pi^2}{27\sqrt{3}} \sum_{m=-\infty}^{\infty} \frac{(2m-\frac{1}{2})}{\sqrt{1+\frac{1}{3}(2m-\frac{1}{2})^2}} \sum_{n=1}^{\infty} n^2\sin\left(\frac{n\pi}{2}\right) K_1\left(n\pi\sqrt{1+\frac{1}{3}(2m-\frac{1}{2})^2}\right). \tag{B.29}$$

B.2.1 General expressions for the ground state

The minimization of the energy given by Eq. (B.22) with respect to the angle α ($\frac{\partial u_{\text{bilayer}}}{\partial \alpha}\Big|_B = 0$) leads to the value $\alpha = -30°$ and consequently the total energy becomes

$$u_{\text{bilayer}}(m_z; B) = E_0^{\text{bilayer}} + E_1^{\text{bilayer}} m_z + E_2^{\text{bilayer}} m_z^2, \tag{B.30}$$

where

$$E_0^{\text{bilayer}} = E_0^{\text{monolayer}}(60°) + \frac{1}{2} I_1 + \frac{3}{4}(D_4 - 6D_1), \tag{B.31}$$

$$E_1^{\text{bilayer}} = -B, \tag{B.32}$$

$$E_2^{\text{bilayer}} = \frac{3}{8}\left(9D_1 + \frac{1}{4}D_2 - 3D_3 - 3D_4\right) + A. \tag{B.33}$$

The term $E_0^{\text{monolayer}}(60°)$ in Eq. (B.31), see also Eq. (B.5), reads:

$$\begin{aligned} E_0^{\text{monolayer}}(60°) = -\frac{1}{3\sqrt{3}} \Bigg\{ 2\zeta(3) - 16\pi^2 \sum_{n=1}^{\infty} \sum_{u=1}^{\infty} \Bigg[n^2 K_0\left(\frac{2\pi}{\sqrt{3}} nu\right) \\ + n^2 \cos(n\pi) K_0\left(\frac{2\pi}{\sqrt{3}} n(u-1/2)\right) \Bigg] \Bigg\}, \end{aligned} \tag{B.34}$$

and the term $A_{2\text{D}}$ in Eq. (B.33) is

$$\begin{aligned} A = \frac{1}{3\sqrt{3}} \Bigg\{ 3\zeta(3) + 4\pi^2 + 8\pi^2 \sum_{n=1}^{\infty} \sum_{u=1}^{\infty} \Bigg[n^2 K_2\left(\frac{2\pi}{\sqrt{3}} nu\right) \\ + n^2 \cos(n\pi) K_2\left(\frac{2\pi}{\sqrt{3}} n(u-1/2)\right) - 3n^2 K_0\left(\frac{2\pi}{\sqrt{3}} nu\right) \\ - 3n^2 \cos(n\pi) K_0\left(\frac{2\pi}{\sqrt{3}} n(u-1/2)\right) \Bigg] \Bigg\}. \end{aligned} \tag{B.35}$$

Then, by minimizing the energy established in Eq. (B.30) with respect to m_z ($\frac{\partial u_{\text{bilayer}}}{\partial m_z}\Big|_B = 0$), we obtain the following magnetization

$$m_z(B) = \frac{B}{2E_2^{\text{bilayer}}} = \chi B \tag{B.36}$$

with $\chi = \dfrac{1}{2E_2^{\text{bilayer}}} = 0.05868$ and the corresponding minimal energy

$$u_{\text{bilayer}}^{\min}(B) = E_0^{\text{bilayer}} - \frac{B^2}{4E_2^{\text{bilayer}}}. \tag{B.37}$$

B.2.2 Solid/Gas transition

The critical value of the magnetic field B_{tr} where the crystal phase is beaten by the gas one is given by the condition

$$u_{\text{bilayer}}^{\min}(B_{\text{tr}}) = u_{gas} = -B_{\text{tr}}. \tag{B.38}$$

By solving Eq. (B.38), we find

$$B_{\text{tr}} = -u_{\text{bilayer}}^{\min}(B_{\text{tr}}) \approx 3.2062124. \tag{B.39}$$

Bibliography

[1] Egor V. Yakovlev, Kirill A. Komarov, Kirill I. Zaytsev, Nikita P. Kryuchkov, Kirill I. Koshelev, Arsen K. Zotov, Dmitry A. Shelestov, Victor L. Tolstoguzov, Vladimir N. Kurlov, Alexei V. Ivlev, and Stanislav O. Yurchenko. Tunable two-dimensional assembly of colloidal particles in rotating electric fields. *Scientific Reports*, 7(1):13727, dec 2017. Creative Commons Attribution 4.0 International License. (Cited on page 1.)

[2] G. M. Whitesides. Self-Assembly at All Scales. *Science*, 295(5564):2418–2421, mar 2002. (Cited on pages 1 and 2.)

[3] Bartosz A. Grzybowski, Christopher E. Wilmer, Jiwon Kim, Kevin P. Browne, and Kyle J. M. Bishop. Self-assembly: from crystals to cells. *Soft Matter*, 5(6):1110, 2009. (Cited on page 1.)

[4] R. Gross and M. Dorigo. Self-Assembly at the Macroscopic Scale. *Proceedings of the IEEE*, 96(9):1490–1508, sep 2008. (Cited on page 1.)

[5] Mingsheng Wang, Le He, and Yadong Yin. Magnetic field guided colloidal assembly. *Materials Today*, 16(4):110–116, April 2013. (Cited on pages 1, 2, 18, 36 and 37.)

[6] O. Carvente, G. G. Peraza-Mues, J. M. Salazar, and J. C. Ruiz-Suárez. Self-assembling of non-Brownian magnetized spheres. *Granular Matter*, 14(3):303–308, may 2012. (Cited on page 2.)

[7] René Messina, Sarah Aljawhari, Lydiane Bécu, Julien Schockmel, Geoffroy Lumay, and Nicolas Vandewalle. Quantitatively mimicking wet colloidal suspensions with dry granular media. *Sci. Rep.*, 5:10348, 06 2015. (Cited on pages 2, 71 and 83.)

[8] X. N. Hou, Y. H. Liu, O. V. Kravchenko, T. A. Lapushkina, O. A. Azarova, Z. Y. Chen, and F. Huang. Structures and dynamics in a two-dimensional dipolar dust particle system. *Physics of Plasmas*, 25(5):053701, may 2018. (Cited on page 2.)

[9] A. Darras, J. Fiscina, M. Pakpour, N. Vandewalle, and G. Lumay. Ribbons of superparamagnetic colloids in magnetic field. *Eur. Phys. J. E*, 39(4):47, apr 2016. (Cited on pages 2, 18, 36, 37 and 53.)

[10] Antara Pal, Vikash Malik, Le He, Ben H Erné, Yadong Yin, Willem K Kegel, and Andrei V Petukhov. Tuning the Colloidal Crystal Structure of Magnetic Particles by External Field. *Angew. Chem. Int. Ed.*, 54(6):1803–1807, December 2014. (Cited on pages 2, 94 and 105.)

[11] U Gasser. Crystallization in three- and two-dimensional colloidal suspensions. *Journal of Physics: Condensed Matter*, 21(20):203101, may 2009. (Cited on page 2.)

[12] A. Yethiraj and A. van Blaaderen. A colloidal model system with an interaction tunable from hard sphere to soft and dipolar. *Nature*, 421:513–517, 2003. (Cited on pages 2, 93, 94, 99 and 105.)

[13] Sven van Teeffelen, Christos N. Likos, and Hartmut Löwen. Colloidal Crystal Growth at Externally Imposed Nucleation Clusters. *Physical Review Letters*, 100(10):108302, mar 2008. (Cited on page 2.)

[14] C HOLM and J WEIS. The structure of ferrofluids: A status report. *Current Opinion in Colloid & Interface Science*, 10(3-4):133–140, oct 2005. (Cited on page 2.)

[15] Valentin S. Mendelev and Alexey O. Ivanov. Ferrofluid aggregation in chains under the influence of a magnetic field. *Phys. Rev. E*, 70:051502, Nov 2004. (Cited on page 2.)

[16] Juan de Vicente, Daniel J. Klingenberg, and Roque Hidalgo-Alvarez. Magnetorheological fluids: a review. *Soft Matter*, 7(8):3701, 2011. (Cited on page 2.)

[17] Frank Smallenburg, Hanumantha Rao Vutukuri, Arnout Imhof, Alfons van Blaaderen, and Marjolein Dijkstra. Self-assembly of colloidal particles into strings in a homogeneous external electric or magnetic field. *Journal of Physics: Condensed Matter*, 24(46):464113, nov 2012. (Cited on page 2.)

[18] D Samsonov, S Zhdanov, G Morfill, and V Steinberg. Levitation and agglomeration of magnetic grains in a complex (dusty) plasma with magnetic field. *New Journal of Physics*, 5:24–24, mar 2003. (Cited on page 2.)

[19] Yang Lu, Liang Dong, Le-Cheng Zhang, Yu-De Su, and Shu-Hong Yu. Biogenic and biomimetic magnetic nanosized assemblies. *Nano Today*, 7(4):297–315, aug 2012. (Cited on pages 2, 17 and 36.)

[20] R. Tao and D. Xiao. Three-dimensional dielectric photonic crystals of body-centered-tetragonal lattice structure. *Applied Physics Letters*, 80(25):4702–4704, jun 2002. (Cited on page 2.)

[21] T. Imthiyaz Ahamed, R. Sundarrajan, G.T. Prasaath, and V. Raviraj. Implementation of Magneto-rheological Dampers in Bumpers of Automobiles for Reducing Impacts during Accidents. *Procedia Engineering*, 97:1220–1226, 2014. (Cited on page 2.)

[22] Xianzhou Zhang, Weihua Li, and X L Gong. Study on magnetorheological shear thickening fluid. *Smart Materials and Structures*, 17(1):015051, feb 2008. (Cited on page 2.)

[23] G. Yang, B.F. Spencer, J.D. Carlson, and M.K. Sain. Large-scale MR fluid dampers: modeling and dynamic performance considerations. *Engineering Structures*, 24(3):309–323, mar 2002. (Cited on page 2.)

[24] Brandon A. Jackson, Kurt J. Terhune, and Lyon B. King. Ionic liquid ferrofluid interface deformation and spray onset under electric and magnetic stresses. *Physics of Fluids*, 29(6):064105, jun 2017. (Cited on page 2.)

[25] Paul Brown, Alexey Bushmelev, Craig P. Butts, Jing Cheng, Julian Eastoe, Isabelle Grillo, Richard K. Heenan, and Annette M. Schmidt. Magnetic Control over Liquid Surface Properties with Responsive Surfactants. *Angewandte Chemie International Edition*, 51(10):2414–2416, mar 2012. (Cited on page 2.)

[26] M. Belkin, A. Snezhko, I. S. Aranson, and W.-K. Kwok. Driven Magnetic Particles on a Fluid Surface: Pattern Assisted Surface Flows. *Physical Review Letters*, 99(15):158301, oct 2007. (Cited on page 2.)

[27] Andy Tay, Alireza Sohrabi, Kate Poole, Stephanie Seidlits, and Dino Di Carlo. A 3D Magnetic Hyaluronic Acid Hydrogel for Magnetomechanical Neuromodulation of Primary Dorsal Root Ganglion Neurons. *Advanced Materials*, 30(29):1800927, jul 2018. (Cited on page 2.)

[28] Joo H Kang, Michael Super, Chong Wing Yung, Ryan M Cooper, Karel Domansky, Amanda R Graveline, Tadanori Mammoto, Julia B Berthet, Heather Tobin, Mark J Cartwright, Alexander L Watters, Martin Rottman, Anna Waterhouse, Akiko Mammoto, Nazita Gamini, Melissa J Rodas, Anxhela Kole, Amanda Jiang, Thomas M Valentin, Alexander Diaz, Kazue Takahashi, and Donald E Ingber. An extracorporeal blood-cleansing device for sepsis therapy. *Nature Medicine*, 20(10):1211–1216, oct 2014. (Cited on page 2.)

[29] Sara Reardon. Artificial spleen cleans up blood. *Nature*, sep 2014. (Cited on page 2.)

[30] Riccardo Di Corato, Gaëlle Béalle, Jelena Kolosnjaj-Tabi, Ana Espinosa, Olivier Clément, Amanda K. A. Silva, Christine Ménager, and Claire Wilhelm. Combining Magnetic Hyperthermia and Photodynamic Therapy for Tumor Ablation with Photoresponsive Magnetic Liposomes. *ACS Nano*, 9(3):2904–2916, mar 2015. (Cited on page 2.)

[31] E. F. Borra, D. Brousseau, M. Cliche, and J. Parent. Aberration correction with a magnetic liquid active mirror. *Monthly Notices of the Royal Astronomical Society*, 391(4):1925–1930, dec 2008. (Cited on page 2.)

[32] A. J. Bandodkar, C. S. Lopez, A. M. Vinu Mohan, L. Yin, R. Kumar, and J. Wang. All-printed magnetically self-healing electrochemical devices. *Science Advances*, 2(11):e1601465–e1601465, nov 2016. (Cited on page 2.)

[33] I. S. Jacobs and C. P. Bean. Approach to elongated fine-particle magnets. *Phys. Rev.*, 100(4):1060–1067, 1955. (Cited on pages 2 and 38.)

[34] P. G. de Gennes and P. A. Pincus. Pair correlations in a ferromagnetic colloid. *Phys. kondens. Materie*, 11(3):189–198, 1970. (Cited on pages 2 and 38.)

[35] J. M. Luttinger and L. Tisza. Theory of dipole interaction in crystals. *Phys. Rev.*, 70:954–964, Dec 1946. (Cited on page 2.)

[36] Thomas C. Halsey and Will Toor. Structure of electrorheological fluids. *Phys. Rev. Lett.*, 65(22):2820–2823, November 1990. (Cited on pages 2, 18, 37 and 38.)

[37] Thomas C. Halsey and Will Toor. Fluctuation-induced couplings between defect lines or particle chains. *Journal of Statistical Physics*, 61(5-6):1257–1281, dec 1990. (Cited on pages 2, 18 and 38.)

[38] R. Tao and J. M. Sun. Three-dimensional structure of induced electrorheological solid. *Phys. Rev. Lett.*, 67(3):398–401, Jul 1991. (Cited on pages 2, 18, 38, 42, 52, 53, 55 and 94.)

[39] Johannes Schönke and Eliot Fried. Stability of vertical magnetic chains. *Proceedings of the Royal Society A: Mathematical, Physical and Engineering Science*, 473(2198):20160703, feb 2017. (Cited on page 3.)

[40] Johannes Schönke, Tobias M. Schneider, and Ingo Rehberg. Infinite geometric frustration in a cubic dipole cluster. *Phys. Rev. B*, 91:020410, Jan 2015. (Cited on page 3.)

[41] Rene Messina, Lara Abou Khalil, and Igor Stankovic. Self-assembly of magnetic balls: From chains to tubes. *Phys. Rev. E*, 89:011202, 2014. (Cited on pages 3, 38, 62 and 88.)

[42] R. Messina and I. Stanković. Reply to "Comment on 'Self-assembly of magnetic balls: From chains to tubes' ". *Phys. Rev. E*, 91(5):057202, mai 2015. (Cited on pages 3, 18 and 42.)

[43] Florian Deißenbeck, Hartmut Löwen, and Erdal C Oğuz. Ground state of dipolar hard spheres confined in channels. *Physical Review E*, 97(5):052608, may 2018. (Cited on page 3.)

[44] René Messina and Igor Stanković. Self-assembly of magnetic spheres in two dimensions: The relevance of onion-like structures. *Europhys. Lett.*, 110(4):46003, may 2015. (Cited on pages 3, 38, 40 and 43.)

[45] Rene Messina and Igor Stanković. Assembly of magnetic spheres in strong homogeneous magnetic field. *Physica A: Statistical Mechanics and its Applications*, 466:10–20, January 2017. (Cited on pages 3, 35, 38, 53 and 94.)

[46] Dominic Vella, Emmanuel du Pontavice, Cameron L. Hall, and Alain Goriely. The magneto-elastica: from self-buckling to self-assembly. *Proc. R. Soc. A*, 470(2162):20130609, 2014. (Cited on page 3.)

[47] J Hernández-Rojas, D Chakrabarti, and D J Wales. Self-assembly of colloidal magnetic particles: energy landscapes and structural transitions. *Physical Chemistry Chemical Physics*, 18(38):26579–26585, 2016. (Cited on page 3.)

[48] K Butter, P H H Bomans, P M Frederik, G J Vroege, and A P Philipse. Direct observation of dipolar chains in iron ferrofluids by cryogenic electron microscopy. *Nature Materials*, 2(2):88–91, January 2003. (Cited on pages 3, 37, 45 and 93.)

[49] Jean-Baptiste Biot and Felix Savart. Note sur le magnetisme de la pile de volta. *Ann. Chem. Phys*, 15:222, 1820. (Cited on page 5.)

[50] John David Jackson. *Classical electrodynamics*. Wiley, New York, 1999. (Cited on pages 6, 7 and 9.)

[51] D J Griffiths. *Introduction to electrodynamics; 4th ed.* Pearson Education, 4th ed. edition, 2014. (Cited on page 6.)

[52] Kira Seleznyova, Mark Strugatsky, and Janis Kliava. Modelling the magnetic dipole. *European Journal of Physics*, 37(2):025203, mar 2016. (Cited on page 6.)

[53] Wikipedia contributors. Magnetic field — Wikipedia, the free encyclopedia, 2018. [Online; accessed 8-June-2018]. (Cited on page 8.)

[54] J. P. Mc Tavish. Field pattern of a magnetic dipole. *American Journal of Physics*, 68(6):577–578, jun 2000. (Cited on page 9.)

[55] Boyd F. Edwards, D. M. Riffe, Jeong-Young Ji, and William A. Booth. Interactions between uniformly magnetized spheres, 2016. (Cited on page 9.)

[56] P.W. Atkins. *The Elements of Physical Chemistry: With Applications in Biology*. W.H. Freeman, New York, 2001. (Cited on page 11.)

[57] Konstantin G. Kornev, Derek Halverson, Guzeliya Korneva, Yury Gogotsi, and Gary Friedman. Magnetostatic interactions between carbon nanotubes

filled with magnetic nanoparticles. *Appl. Phys. Lett.*, 92(23):233117, 2008. (Cited on pages 11, 18, 36 and 53.)

[58] M. J. D. Powell. *A Direct Search Optimization Method That Models the Objective and Constraint Functions by Linear Interpolation*, pages 51–67. Springer Netherlands, Dordrecht, 1994. (Cited on page 12.)

[59] J. A. Nelder and R. Mead. A Simplex Method for Function Minimization. *The Computer Journal*, 7(4):308–313, jan 1965. (Cited on page 12.)

[60] Dieter Kraft. *A software package for sequential quadratic programming*. Forschungsbericht / Deutsche Forschungs- und Versuchsanstalt für Luft- und Raumfahrt. Köln, 1988. (Cited on pages 12, 111, 112, 113 and 114.)

[61] Charles L. Lawson and Richard J. Hanson. *Solving Least Squares Problems*. Classics in Applied Mathematics. Society for Industrial and Applied Mathematics, 1995. (Cited on pages 12 and 113.)

[62] Steven G. Johnson. The NLopt nonlinear-optimization package, 2014. Version 2.4.2. http://ab-initio.mit.edu/nlopt. (Cited on pages 13, 40, 52, 85 and 95.)

[63] René Messina and Ludovic Spiteri. On the interaction of dipolar filaments. *Eur. Phys. J. E*, 39:81, aug 2016. (Cited on pages 17, 38, 52 and 53.)

[64] R. Blakemore. Magnetotactic bacteria. *Science*, 190:377–379, 1975. (Cited on pages 17 and 37.)

[65] Tanya Prozorov, Dennis A. Bazylinski, Surya K. Mallapragada, and Ruslan Prozorov. Novel magnetic nanomaterials inspired by magnetotactic bacteria: Topical review. *Materials Science and Engineering: R: Reports*, 74(5):133–172, may 2013. (Cited on pages 17 and 36.)

[66] Michael Winklhofer, Elke Holtkamp-Rötzler, Marianne Hanzlik, Gerta Fleissner, and Nikolai Petersen. Clusters of superparamagnetic magnetite particles in the upper-beak skin of homing pigeons: evidence of a magnetoreceptor? *European Journal of Mineralogy*, 13(4):659–669, jul 2001. (Cited on page 17.)

[67] F.F. Torres de Araujo, M.A. Pires, R.B. Frankel, and C.E. M. Bicudo. Magnetite and magnetotaxis in algae. *Biophysical Journal*, 50(2):375 – 378, 1986. (Cited on page 17.)

[68] Q. A. Pankhurst, J. Connolly, S. K. Jones, and J. Dobson. Applications of magnetic nanoparticles in biomedicine. *Journal of Physics D: Applied Physics*, 36(13):R167, 2003. (Cited on page 17.)

[69] Hui Wang, Yifei Yu, Yubin Sun, and Qianwang Chen. Magnetic nanochains: a review. *Nano*, 06(01):1–17, February 2011. (Cited on page 17.)

[70] Ji-Ho Park, Geoffrey von Maltzahn, Lianglin Zhang, Michael P. Schwartz, Erkki Ruoslahti, Sangeeta N. Bhatia, and Michael J. Sailor. Magnetic iron oxide nanoworms for tumor targeting and imaging. *Adv. Mater.*, 20(9):1630–1635, may 2008. (Cited on page 17.)

[71] Carlos Martinez-Boubeta, Konstantinos Simeonidis, Antonios Makridis, Makis Angelakeris, Oscar Iglesias, Pablo Guardia, Andreu Cabot, Lluis Yedra, Sonia Estradé, Francesca Peiró, Zineb Saghi, Paul A. Midgley, Iván Conde-Leborán, David Serantes, and Daniel Baldomir. Learning from nature to improve the heat generation of iron-oxide nanoparticles for magnetic hyperthermia applications. *Scientific Reports*, 3:1652, 04 2013. (Cited on page 17.)

[72] A Fert and L Piraux. Magnetic nanowires. *Journal of Magnetism and Magnetic Materials*, 200(1–3):338 – 358, 1999. (Cited on page 18.)

[73] Monica Tanase, Laura Ann Bauer, Anne Hultgren, Daniel M. Silevitch, Li Sun, Daniel H. Reich, Peter C. Searson, and Gerald J. Meyer. Magnetic Alignment of Fluorescent Nanowires. *Nano Letters*, 1(3):155–158, March 2001. (Cited on pages 18 and 36.)

[74] M. Skarabot, M. Ravnik, S. Zumer, U. Tkalec, I. Poberaj, D. Babic, N. Osterman, and I. Muvsevic. Two-dimensional dipolar nematic colloidal crystals. *Phys. Rev. E*, 76(5):051406, nov 2007. (Cited on pages 18, 36 and 53.)

[75] Yu Gu, Ruslan Burtovyy, John Custer, Igor Luzinov, and Konstantin G. Kornev. A gradient field defeats the inherent repulsion between magnetic nanorods. *Royal Society Open Science*, 1(2):140271, October 2014. (Cited on pages 18, 21 and 53.)

[76] Thomas C. Halsey. Electrorheological fluids. *Science*, 258(5083):761–766, 1992. (Cited on page 18.)

[77] Eric M. Furst and Alice P. Gast. Dynamics and lateral interactions of dipolar chains. *Phys. Rev. E*, 62(5):6916–6925, November 2000. (Cited on pages 18 and 37.)

[78] T. Friedrich, I. Rehberg, and R. Richter. Comment on "Self-assembly of magnetic balls: From chains to tubes". *Phys. Rev. E*, 91(5):057201, mai 2015. (Cited on page 18.)

[79] A. O. Tsebers. Thermodynamic stability of a suspension of magnetic needles. *Magnetohydrodynamics*, 19:146–150, 1983. (Cited on page 18.)

[80] P I Belobrov, R S Gekht, and V A Ignatchenko. Ground state in systems with dipole interaction. *Zh. Eksp. Teor. Fiz*, 84(March 1983):1097–1108, 1983. (Cited on page 18.)

[81] P I Belobrov, V A Voevodin, and V A. Ground state of a dipole system in a plane rhombic lattice. *Soviet Physics JETP*, 88(March 1985):889–893, 1985. (Cited on pages 18 and 84.)

[82] Peter I Belobrov, Ivan V Ermilovit, and Avgust K Tsikh. Stable and Ground States of Dipolic. *Department of Mathematics, Royal Institute of Technology, S-100 44 Stockholm, Sweden*, 1991. (Cited on page 18.)

[83] Yu Gu. *Composite Films with Magnetic Nanorods: Fundamentals, Processing and Applications*. Dissertation, Clemson University, 2014. (Cited on page 21.)

[84] B R Jennings, M Xu, and P J Ridler. Structure in magneto-rheological fluids: a theoretical analysis. *Journal of Physics D: Applied Physics*, 34(11):1617–1623, may 2001. (Cited on page 34.)

[85] X Xie, Y Mai, and X Zhou. Dispersion and alignment of carbon nanotubes in polymer matrix: A review. *Materials Science and Engineering: R: Reports*, 49(4):89–112, may 2005. (Cited on page 36.)

[86] Yixing Ye and Baoyou Geng. Magnetic nanotubes: Synthesis, properties, and applications. *Critical Reviews in Solid State and Materials Sciences*, 37(2):75–93, apr 2012. (Cited on page 36.)

[87] Angel Ríos, Mohammed Zougagh, and Mohamed Bouri. Magnetic (nano)materials as an useful tool for sample preparation in analytical methods. a review. *Analytical Methods*, 5(18):4558, 2013. (Cited on page 36.)

[88] J. Velazquez, K. R. Pirota, and M. Vazquez. About the dipolar approach in magnetostatically coupled bistable magnetic micro and nanowires. *IEEE Transactions on Magnetics*, 39(5):3049–3051, September 2003. (Cited on page 36.)

[89] Sang Jun Son, Jonathan Reichel, Bo He, Mattan Schuchman, and Sang Bok Lee. Magnetic nanotubes for magnetic-field-assisted bioseparation, biointeraction, and drug delivery. *J. Am. Chem. Soc.*, 127(20):7316–7317, may 2005. (Cited on page 36.)

[90] C. Eisenmann, U. Gasser, P. Keim, and G. Maret. Anisotropic defect-mediated melting of two-dimensional colloidal crystals. *Phys. Rev. Lett.*, 93(10):105702, sep 2004. (Cited on page 36.)

[91] Genovéva Filipcsei, Ildikó Csetneki, András Szilágyi, and Miklós Zrínyi. *Oligomers - Polymer Composites - Molecular Imprinting*, volume 206 of *Advances in Polymer Science*, chapter Magnetic Field-Responsive Smart Polymer Composites, pages 137–189. Springer Berlin Heidelberg, Berlin, Heidelberg, 2007. (Cited on page 36.)

[92] Pietro Tierno. Recent advances in anisotropic magnetic colloids: realization, assembly and applications. *Phys. Chem. Chem. Phys.*, 16(43):23515–23528, August 2014. (Cited on page 36.)

[93] G. Lumay, S. Dorbolo, and N. Vandewalle. Compaction dynamics of a magnetized powder. *Phys. Rev. E*, 80(4):041302, oct 2009. (Cited on page 36.)

[94] Sara Mehdizadeh Taheri, Maria Michaelis, Thomas Friedrich, Beate Förster, Markus Drechsler, Florian M. Römer, Peter Bösecke, Theyencheri Narayanan, Birgit Weber, Ingo Rehberg, and et al. Self-assembly of smallest magnetic particles. *Proc Natl Acad Sci USA*, 112(47):14484–14489, Nov 2015. (Cited on pages 36, 37 and 53.)

[95] Ludovic Spiteri and René Messina. Columnar aggregation of dipolar chains. *Europhys. Lett.*, 120(3):36001, 2017. (Cited on pages 37, 53 and 55.)

[96] E. Alphandery, Y. Ding, A. T. Ngo, Z. L. Wang, L. F. Wu, and M. P. Pileni. Assemblies of aligned magnetotactic bacteria and extracted magnetosomes: What is the main factor responsible for the magnetic anisotropy? *ACS Nano*, 3(6):1539–1547, JUN 2009. (Cited on page 37.)

[97] Bahareh Kiani, Damien Faivre, and Stefan Klumpp. Elastic properties of magnetosome chains. *New Journal of Physics*, 17(4):043007–12, April 2015. (Cited on page 37.)

[98] Melanie Ewerlin, Derya Demirbas, Frank Brüssing, Oleg Petracic, Ahmet A. Ünal, Sergio Valencia, Florian Kronast, and Hartmut Zabel. Magnetic dipole and higher pole interaction on a square lattice. *Phys. Rev. Lett.*, 110:177209, Apr 2013. (Cited on page 37.)

[99] A. T. Skjeltorp. One- and two-dimensional crystallization of magnetic holes. *Phys. Rev. Lett.*, 51:2306–2309, Dec 1983. (Cited on page 37.)

[100] Eric M. Furst and Alice P. Gast. Micromechanics of dipolar chains using optical tweezers. *Phys. Rev. Lett.*, 82:4130–4133, May 1999. (Cited on page 37.)

[101] Mirjam E Leunissen, Hanumantha Rao Vutukuri, and Alfons van Blaaderen. Directing Colloidal Self-Assembly with Biaxial Electric Fields. *Advanced Materials*, 21(30):3116–3120, August 2009. (Cited on pages 37 and 105.)

[102] James E. Martin, Kimberly M. Hill, and Chris P. Tigges. Magnetic-field-induced optical transmittance in colloidal suspensions. *Phys. Rev. E*, 59:5676–5692, May 1999. (Cited on page 37.)

[103] J J Weis. Simulation of quasi-two-dimensional dipolar systems. *Journal of Physics: Condensed Matter*, 15(15):S1471–S1495, April 2003. (Cited on pages 38 and 83.)

[104] J J Weis. Low density quasi-two-dimensional dipolar hard spheres in an external field. *Molecular Physics*, 103(1):7–10, January 2005. (Cited on page 38.)

[105] Jordi Faraudo, Jordi S Andreu, Carles Calero, and Juan Camacho. Predicting the Self-Assembly of Superparamagnetic Colloids under Magnetic Fields. *Advanced Functional Materials*, 26(22):3837–3858, January 2016. (Cited on page 38.)

[106] James E. Martin, Robert A. Anderson, and Chris P. Tigges. Simulation of the athermal coarsening of composites structured by a uniaxial field. *J. Chem. Phys.*, 108(9):3765–3787, mar 1998. (Cited on pages 38 and 53.)

[107] R. Tao and J. M. Sun. Ground state of electrorheological fluids from monte carlo simulations. *Phys. Rev. A*, 44(10):R6181–R6184, nov 1991. (Cited on pages 38 and 94.)

[108] Weijia Wen, F. Kun, K. F. Pál, D. W. Zheng, and K. N. Tu. Aggregation kinetics and stability of structures formed by magnetic microspheres. *Phys. Rev. E*, 59:R4758–R4761, May 1999. (Cited on page 38.)

[109] Taisia A. Prokopieva, Victor A. Danilov, Sofia S. Kantorovich, and Christian Holm. Ground state structures in ferrofluid monolayers. *Phys. Rev. E*, 80:031404, Sep 2009. (Cited on page 38.)

[110] Victor Danilov, Taisia Prokopyeva, and Sofia Kantorovich. Ground-state structures and structural transitions in a monolayer of magnetic dipolar particles in the presence of an external magnetic field. *Phys. Rev. E*, 86:061408, Dec 2012. (Cited on page 38.)

[111] Francisca Guzmán-Lastra, Andreas Kaiser, and Hartmut Löwen. Fission and fusion scenarios for magnetic microswimmer clusters. *Nature Communications*, 7:13519, November 2016. (Cited on page 38.)

[112] A. Grzybowski and A. Brodka. Lekner type method for summing the dipole—dipole interactions in computer simulations of one- and two-dimensionally periodic systems. *Molec. Phys.*, 101:1079–1088, 2003. (Cited on pages 38, 51 and 78.)

[113] Cheol Park and Richard E. Robertson. Alignment of particles by an electric field. *Materials Science and Engineering: A*, 257(2):295–311, dec 1998. (Cited on pages 45 and 46.)

[114] David A Norman and Richard E Robertson. The effect of fiber orientation on the toughening of short fiber-reinforced polymers. *Journal of Applied Polymer Science*, 90(10):2740–2751, September 2003. (Cited on page 45.)

[115] Cheol Park, John Wilkinson, Sumanth Banda, Zoubeida Ounaies, Kristopher E Wise, Godfrey Sauti, Peter T Lillehei, and Joycelyn S Harrison. Aligned single-wall carbon nanotube polymer composites using an electric field. *Journal of Polymer Science Part B: Polymer Physics*, 44(12):1751–1762, 2006. (Cited on page 46.)

[116] Ludovic Spiteri and René Messina. Dipolar crystals: The crucial role of the clinohexagonal prism phase. *Phys. Rev. Lett.*, 119:155501, Oct 2017. (Cited on pages 46, 53 and 93.)

[117] Galen T. Pickett, Mark Gross, and Hiroko Okuyama. Spontaneous chirality in simple systems. *Phys. Rev. Lett.*, 85:3652–3655, Oct 2000. (Cited on pages 46 and 48.)

[118] EC Oğuz, R Messina, and H Löwen. Helicity in cylindrically confined yukawa systems. *Europhys. Lett.*, 94(2):28005, 2011. (Cited on pages 46 and 48.)

[119] Igor Stanković, Miljan Dašić, and René Messina. Structure and cohesive energy of dipolar helices. *Soft Matter*, 12(12):3056–3065, 2016. (Cited on pages 46, 48 and 60.)

[120] Ludovic Spiteri, Igor Stanković, and René Messina. Interaction of dipolar helical chains including linear- and zigzag-chains. *The Journal of chemical physics*, 2018. Submitted. (Cited on page 47.)

[121] A Wada. The alpha-helix as an electric macro-dipole. *Advances in biophysics*, pages 1–63, 1976. (Cited on page 48.)

[122] J. Martin Scholtz and Robert L. Baldwin. The mechanism of alpha-helix formation by peptides. *Annual Review of Biophysics and Biomolecular Structure*, 21(1):95–118, 1992. PMID: 1525475. (Cited on page 48.)

[123] Andrew H J Wang, Gary J Quigley, Francis J Kolpak, James L Crawford, Jacques H van Boom, Gijs van der Marel, and Alexander Rich. Molecular structure of a left-handed double helical DNA fragment at atomic resolution. *Nature*, 282(5740):680–686, December 1979. (Cited on page 48.)

[124] Howard C Berg. The Rotary Motor of Bacterial Flagella. *Annual Review of Biochemistry*, 72(1):19–54, 2003. (Cited on page 48.)

[125] Iain M Cheeseman and Arshad Desai. Molecular architecture of the kinetochore–microtubule interface. *Nature Reviews Molecular Cell Biology*, 9(1):33–46, January 2008. (Cited on page 48.)

[126] Sumio Iijima. Helical microtubules of graphitic carbon. *Nature*, 354(6348):56–58, November 1991. (Cited on page 48.)

[127] X B Zhang, X F Zhang, D Bernaerts, G van Tendeloo, S Amelinckx, J van Landuyt, V Ivanov, J B Nagy, Ph Lambin, and A A Lucas. The Texture of Catalytically Grown Coil-Shaped Carbon Nanotubules. *Europhys. Lett.*, 27(2):141–146, July 1994. (Cited on page 48.)

[128] Takahiro Shimada, Junichi Okuno, and Takayuki Kitamura. Chiral Selectivity of Unusual Helimagnetic Transition in Iron Nanotubes: Chirality Makes Quantum Helimagnets. *Nano Letters*, 13(6):2792–2797, May 2013. (Cited on page 48.)

[129] Yukihito Kondo and Kunio Takayanagi. Synthesis and Characterization of Helical Multi-Shell Gold Nanowires. *Science*, 289(5479):606–608, July 2000. (Cited on page 48.)

[130] Feng Li, Xavier Badel, Jan Linnros, and John B Wiley. Fabrication of Colloidal Crystals with Tubular-like Packings. *J. Am. Chem. Soc.*, 127(10):3268–3269, March 2005. (Cited on page 48.)

[131] M A Lohr, A M Alsayed, B G Chen, Z Zhang, R D Kamien, and A G Yodh. Helical packings and phase transformations of soft spheres in cylinders. *Phys. Rev. E*, 81(4):040401, April 2010. (Cited on page 48.)

[132] Mahdi Zaeifi Yamchi and Richard K. Bowles. Helical defect packings in a quasi-one-dimensional system of cylindrically confined hard spheres. *Phys. Rev. Lett.*, 115:025702, Jul 2015. (Cited on page 48.)

[133] Yadong Yin and Younan Xia. Self-Assembly of Spherical Colloids into Helical Chains with Well-Controlled Handedness. *J. Am. Chem. Soc.*, 125(8):2048–2049, February 2003. (Cited on page 48.)

[134] Yumino Hayase, Takahiro Sakaue, and Hiizu Nakanishi. Compressive response and helix formation of a semiflexible polymer confined in a nanochannel. *Phys. Rev. E*, 95(5):052502, May 2017. (Cited on page 48.)

[135] Sid Ahmed Sabeur, Fatima Hamdache, and Friederike Schmid. Kinetically driven helix formation during the homopolymer collapse process. *Phys. Rev. E*, 77:020802, Feb 2008. (Cited on page 48.)

[136] Wenrong Zhao, Shuli Dong, and Jingcheng Hao. Colloidal Wormlike Micelles with Highly Ferromagnetic Properties. *Langmuir*, 31(41):11243–11248, October 2015. (Cited on page 48.)

[137] D Zerrouki, J Baudry, D Pine, P Chaikin, and J Bibette. Chiral colloidal clusters. *Nature*, 455(7211):380–382, September 2008. (Cited on pages 48 and 68.)

[138] Gurvinder Singh, Henry Chan, Artem Baskin, Elijah Gelman, Nikita Repnin, Petr Král, and Rafal Klajn. Self-assembly of magnetite nanocubes into helical superstructures. *Science*, 345(6201):1149–1153, 2014. (Cited on pages 48 and 68.)

[139] Qian Chen, Jonathan K. Whitmer, Shan Jiang, Sung Chul Bae, Erik Luijten, and Steve Granick. Supracolloidal Reaction Kinetics of Janus Spheres. *Science*, 331(6014):199–202, JAN 14 2011. (Cited on pages 48 and 68.)

[140] M Sobrino Fernández, V R Misko, and F M Peeters. Self-assembly of Janus particles into helices with tunable pitch. *Phys. Rev. E*, 92(4):042309, October 2015. (Cited on pages 48 and 68.)

[141] Ruohai Guo, Jian Mao, Xu-Ming Xie, and Li-Tang Yan. Predictive supracolloidal helices from patchy particles. *Scientific Reports*, 4(1):2418, November 2014. (Cited on pages 48 and 68.)

[142] Helmut H Strey, Rudi Podgornik, Donald C Rau, and V Adrian Parsegian. DNA-DNA interactions. *Current Opinion in Structural Biology*, 8(3):309–313, June 1998. (Cited on page 48.)

[143] H M Harreis, A A Kornyshev, C N Likos, H Löwen, and G Sutmann. Phase Behavior of Columnar DNA Assemblies. *Phys. Rev. Lett.*, 89(1):018303, June 2002. (Cited on page 48.)

[144] M Kanduč, J Dobnikar, and R Podgornik. Counterion-mediated electrostatic interactions between helical molecules. *Soft Matter*, 5(4):868–877, February 2009. (Cited on page 48.)

[145] A G Cherstvy. Electrostatic interactions in biological DNA-related systems. *Physical Chemistry Chemical Physics*, 13(21):9942–27, 2011. (Cited on page 48.)

[146] Albert P. Philipse and Diana Maas. Magnetic Colloids from Magnetotactic Bacteria: Chain Formation and Colloidal Stability. *Langmuir*, 18(25):9977–9984, dec 2002. (Cited on page 53.)

[147] Stoyan K Smoukov, Sumit Gangwal, Manuel Marquez, and Orlin D Velev. Reconfigurable responsive structures assembled from magnetic Janus particles. *Soft Matter*, 5(6):1285, 2009. (Cited on pages 53, 58 and 68.)

[148] Jorge L C Domingos, François M Peeters, and W P Ferreira. Self-assembly of rigid magnetic rods consisting of single dipolar beads in two dimensions. *Phys. Rev. E*, 96(1):012603, July 2017. (Cited on page 53.)

[149] D A Rozhkov, E S Pyanzina, E V Novak, J J Cerdà, T Sintes, M Ronti, P A Sánchez, and S S Kantorovich. Self-assembly of polymer-like structures of magnetic colloids: Langevin dynamics study of basic topologies. *Molecular Simulation*, 44(6):507–515, 2018. (Cited on page 53.)

[150] Ivan A Sergienko, Cengiz Şen, and Elbio Dagotto. Ferroelectricity in the Magnetic E-Phase of Orthorhombic Perovskites. *Phys. Rev. Lett.*, 97(22):220401, November 2006. (Cited on page 55.)

[151] J C Tung and G Y Guo. Systematic ab initiostudy of the magnetic and electronic properties of all 3dtransition metal linear and zigzag nanowires. *Phys. Rev. B*, 76(9):094413, September 2007. (Cited on page 55.)

[152] G E Astrakharchik, Giovanna Morigi, Gabriele De Chiara, and J Boronat. Ground state of low-dimensional dipolar gases: Linear and zigzag chains. *Phys. Rev. A*, 78(6):063622, December 2008. (Cited on page 55.)

[153] Dengxu Wang, Haiyan He, Xiaohui Chen, Shengyu Feng, Yuzhong Niu, and Daofeng Sun. A 3D porous metal–organic framework constructed of 1D zigzag and helical chains exhibiting selective anion exchange. *CrystEngComm*, 12(4):1041–1043, 2010. (Cited on page 55.)

[154] Arthur V Straube, Roel P A Dullens, Lutz Schimansky-Geier, and Ard A Louis. Zigzag transitions and nonequilibrium pattern formation in colloidal chains. *J. Chem. Phys.*, 139(13):134908, October 2013. (Cited on page 55.)

[155] Stefano Sacanna, Laura Rossi, and David J Pine. Magnetic Click Colloidal Assembly. *J. Am. Chem. Soc.*, 134(14):6112–6115, April 2012. (Cited on page 58.)

[156] Lydiane Becu, Marc Basler, Miodrag L. Kulić, and Igor M. Kulić. Resonant reshaping of colloidal clusters on a current carrying wire. *The European Physical Journal E*, 40(12):107, Dec 2017. (Cited on page 68.)

[157] Jing Yan, Kundan Chaudhary, Sung Chul Bae, Jennifer A Lewis, and Steve Granick. Colloidal ribbons and rings from Janus magnetic rods. *Nature Communications*, 4:1516, 2013. (Cited on page 68.)

[158] Timothy J Richmond and Frederic M Richards. Packing of α-helices: Geometrical constraints and contact areas. *Journal of Molecular Biology*, 119(4):537–555, 1978. (Cited on page 68.)

[159] W G J Hol, P T van Duijnen, and H J C Berendsen. The α-helix dipole and the properties of proteins. *Nature*, 273(5662):443–446, June 1978. (Cited on page 68.)

[160] Graziano Vernizzi, Kevin L Kohlstedt, and Monica Olvera de la Cruz. The electrostatic origin of chiral patterns on nanofibers. *Soft Matter*, 5(4):736–739, February 2009. (Cited on page 68.)

[161] Y Ding, H C Öttinger, A D Schlüter, and M Kröger. From atomistic simulation to the dynamics, structure and helical network formation of dendronized polymers: The Janus chain model. *The Journal of Chemical Physics*, 127(9):094904, September 2007. (Cited on page 68.)

[162] Martin Kröger, Orit Peleg, Yi Ding, and Yitzhak Rabin. Formation of double helical and filamentous structures in models of physical and chemical gels. *Soft Matter*, 4(1):18–28, 2008. (Cited on page 68.)

[163] Frank Smallenburg and Marjolein Dijkstra. Phase diagram of colloidal spheres in a biaxial electric or magnetic field. *The Journal of Chemical Physics*, 132(20):204508, may 2010. (Cited on pages 68 and 105.)

[164] Ludovic Spiteri, René Messina, David Gonzalez-Rodriguez, and Lydiane Bécu. Ordering of sedimenting paramagnetic colloids in a monolayer. *Physical Review E*, 98(2):020601, aug 2018. (Cited on page 71.)

[165] P. N. Pusey and W. van Megen. Phase behaviour of concentrated suspensions of nearly hard colloidal spheres. *Nature*, 320(6060):340–342, mar 1986. (Cited on page 71.)

[166] K. Zahn, R. Lenke, and G. Maret. Two-stage melting of paramagnetic colloidal crystals in two dimensions. *Phys. Rev. Lett.*, 82:2721–2724, Mar 1999. (Cited on pages 71 and 83.)

[167] K. Zahn and G. Maret. Dynamic criteria for melting in two dimensions. *Phys. Rev. Lett.*, 85:3656–3659, Oct 2000. (Cited on page 71.)

[168] U. Gasser, Eric R. Weeks, Andrew Schofield, P. N. Pusey, and D. A. Weitz. Real-space imaging of nucleation and growth in colloidal crystallization. *Science*, 292(5515):258–262, 2001. (Cited on page 71.)

[169] Jacob P. Hoogenboom, Didi Derks, Peter Vergeer, and Alfons van Blaaderen. Stacking faults in colloidal crystals grown by sedimentation. *The Journal of Chemical Physics*, 117(24):11320–11328, dec 2002. (Cited on page 71.)

[170] Aurore Merlin, Jean-Baptiste Salmon, and Jacques Leng. Microfluidic-assisted growth of colloidal crystals. *Soft Matter*, 8(13):3526, 2012. (Cited on page 71.)

[171] U Gasser. Crystallization in three- and two-dimensional colloidal suspensions. *Journal of Physics: Condensed Matter*, 21(20):203101, 2009. (Cited on pages 71 and 83.)

[172] Juan F. Galisteo-López, Marta Ibisate, Riccardo Sapienza, Luis S. Froufe-Pérez, Álvaro Blanco, and Cefe López. Self-Assembled Photonic Structures. *Advanced Materials*, 23(1):30–69, jan 2011. (Cited on page 71.)

[173] Sanford A. Asher and John H. Holtz. Polymerized colloidal crystal hydrogel films as intelligent chemical sensing materials. *Nature*, 389(6653):829–832, oct 1997. (Cited on page 71.)

[174] O. D. Velev and E. W. Kaler. Structured Porous Materials via Colloidal Crystal Templating: From Inorganic Oxides to Metals. *Advanced Materials*, 12(7):531–534, apr 2000. (Cited on page 71.)

[175] P N Pusey, W van Megen, S M Underwood, P Bartlett, and R H Ottewill. Colloidal fluids, crystals and glasses. *Journal of Physics: Condensed Matter*, 2(S):SA373–SA377, dec 1990. (Cited on page 71.)

[176] P N Pusey. *Liquids, freezing and the glass transition*. North-Holland: Amsterdam, 1991. (Cited on page 71.)

[177] Lahcen Assoud, Florian Ebert, Peter Keim, René Messina, Georg Maret, and Hartmut Löwen. Ultrafast quenching of binary colloidal suspensions in an external magnetic field. *Phys. Rev. Lett.*, 102:238301, Jun 2009. (Cited on pages 71 and 74.)

[178] Perrin, Jean. Mouvement brownien et molécules. *J. Phys. Theor. Appl.*, 9(1):5–39, 1910. (Cited on pages 71 and 77.)

[179] A Vrij. Sedimentation equilibrium in concentrated, multicomponent particle dispersions. hard spheres in the percus–yevick approximation. *The Journal of Chemical Physics*, 72(6):3735–3739, 1980. (Cited on page 72.)

[180] Thierry Biben, Jean-Pierre Hansen, and Jean-Louis Barrat. Density profiles of concentrated colloidal suspensions in sedimentation equilibrium. *J. Chem. Phys.*, 98(9):7330–7344, may 1993. (Cited on pages 72, 76 and 80.)

[181] T Biben and J P Hansen. Sedimentation equilibrium in concentrated charge-stabilized colloidal suspensions. *Journal of Physics: Condensed Matter*, 6(23A):A345, 1994. (Cited on page 72.)

[182] T Biben, R Ohnesorge, and H Löwen. Crystallization in Sedimentation Profiles of Hard Spheres. *Europhys. Lett.*, 28(9):665–670, December 1994. (Cited on pages 72 and 80.)

[183] C Patrick Royall, Joachim Dzubiella, Matthias Schmidt, and Alfons van Blaaderen. Nonequilibrium Sedimentation of Colloids on the Particle Scale. *Phys. Rev. Lett.*, 98(18):77–4, May 2007. (Cited on page 72.)

[184] A Esztermann and H Löwen. Colloidal Brazil-nut effect in sediments of binary charged suspensions. *Europhys. Lett.*, 68(1):120–126, October 2004. (Cited on page 72.)

[185] Tobias Kruppa, Tim Neuhaus, Rene Messina, and Hartmut Löwen. Soft repulsive mixtures under gravity: Brazil-nut effect, depletion bubbles, boundary layering, nonequilibrium shaking. *J. Chem. Phys.*, 136(13):134106, April 2012. (Cited on page 72.)

[186] Matthias Schmidt, Marjolein Dijkstra, and Jean-Pierre Hansen. Floating Liquid Phase in Sedimenting Colloid-Polymer Mixtures. *Physical Review Letters*, 93(8):088303, aug 2004. (Cited on page 72.)

[187] Matthias Schmidt, Marjolein Dijkstra, and Jean-Pierre Hansen. Competition between sedimentation and phase coexistence of colloidal dispersions under gravity. *Journal of Physics: Condensed Matter*, 16(38):S4185–S4194, sep 2004. (Cited on page 72.)

[188] Alice L Thorneywork, Joshua L Abbott, Dirk G A L Aarts, and Roel P A Dullens. Two-Dimensional Melting of Colloidal Hard Spheres. *Phys. Rev. Lett.*, 118(15):158001–5, April 2017. (Cited on page 72.)

[189] Ekaterina A Elfimova, Alexey O Ivanov, Ekaterina V Lakhtina, Alexander F Pshenichnikov, and Philip J Camp. Sedimentation equilibria in polydisperse ferrofluids: critical comparisons between experiment, theory, and computer simulation. *Soft Matter*, 12:4103–4112, April 2016. (Cited on page 72.)

[190] Roberto Piazza. Settled and unsettled issues in particle settling. *Reports on Progress in Physics*, 77(5):056602, may 2014. (Cited on page 72.)

[191] K. Zahn, J. M. Méndez-Alcaraz, and G. Maret. Hydrodynamic interactions may enhance the self-diffusion of colloidal particles. *Phys. Rev. Lett.*, 79:175–178, 1997. (Cited on page 72.)

[192] E. Madelung. Das elektrische feld in systemen von regelmäßig angeordneten punktladungen. *Phys. Z.*, 19:542, 1918. (Cited on page 75.)

[193] M M Hurley and Sherwin J Singer. Domain energies of the dipolar lattice gas. *The Journal of Physical Chemistry*, 96(4):1938–1950, February 1992. (Cited on page 75.)

[194] N. Metropolis, A. W. Rosenbluth, M. N. Rosenbluth, A. N. Teller, and E. Teller. To fill. *J. Chem. Phys.*, 21:1087, 1953. (Cited on page 77.)

[195] Michael P. Allen and Dominic J. Tildesley. *Computer Simulation of Liquids*, volume 1. Oxford University Press, nov 2017. (Cited on page 77.)

[196] Sebastian C Kapfer and Werner Krauth. Two-Dimensional Melting: From Liquid-Hexatic Coexistence to Continuous Transitions. *Phys. Rev. Lett.*, 114(3):035702–5, January 2015. (Cited on page 81.)

[197] Ludovic Spiteri, Hervé Mohrbach, and René Messina. Layered dipolar particles in external magnetic field. 2018. To be submitted. (Cited on page 83.)

[198] K. De'Bell, A. B. MacIsaac, and J. P. Whitehead. Dipolar effects in magnetic thin films and quasi-two-dimensional systems. *Reviews of Modern Physics*, 72(1):225–257, jan 2000. (Cited on page 83.)

[199] Ching-Yao Chen and C.-S. Li. Ordered microdroplet formations of thin ferrofluid layer breakups. *Physics of Fluids*, 22(1):014105, jan 2010. (Cited on page 83.)

[200] Jing Yan, Sung Chul Bae, and Steve Granick. Colloidal Superstructures Programmed into Magnetic Janus Particles. *Advanced Materials*, 27(5):874–879, feb 2015. (Cited on page 83.)

[201] R. Seshadri and R. M. Westervelt. Statistical mechanics of magnetic bubble arrays. I. Topology and thermalization. *Physical Review B*, 46(9):5142–5149, sep 1992. (Cited on page 83.)

[202] R. Seshadri and R. M. Westervelt. Statistical mechanics of magnetic bubble arrays. II. Observations of two-dimensional melting. *Physical Review B*, 46(9):5150–5161, sep 1992. (Cited on page 83.)

[203] I. Musevic. Two-Dimensional Nematic Colloidal Crystals Self-Assembled by Topological Defects. *Science*, 313(5789):954–958, aug 2006. (Cited on page 83.)

[204] Weijia Wen, F. Kun, K. F. Pál, D. W. Zheng, and K. N. Tu. Aggregation kinetics and stability of structures formed by magnetic microspheres. *Physical Review E*, 59(5):R4758–R4761, may 1999. (Cited on page 83.)

[205] J. Schockmel, E. Mersch, N. Vandewalle, and G. Lumay. Melting of a confined monolayer of magnetized beads. *Phys. Rev. E*, 87(6):062201, JUN 10 2013. (Cited on page 83.)

[206] M. Golosovsky, Y. Saado, and D. Davidov. Self-assembly of floating magnetic particles into ordered structures: A promising route for the fabrication of tunable photonic band gap materials. *Applied Physics Letters*, 75(26):4168–4170, dec 1999. (Cited on page 83.)

[207] Weijia Wen, Lingyun Zhang, and Ping Sheng. Planar Magnetic Colloidal Crystals. *Physical Review Letters*, 85(25):5464–5467, dec 2000. (Cited on page 83.)

[208] G. Helgesen and A. T. Skjeltorp. An experimental system for studying dynamic behavior of magnetic microparticles. *Journal of Applied Physics*, 69(12):8277–8284, jun 1991. (Cited on page 83.)

[209] Nina V. Dziomkina and G. Julius Vancso. Colloidal crystal assembly on topologically patterned templates. *Soft Matter*, 1(4):265, 2005. (Cited on page 83.)

[210] CA Ross. Patterned Magnetic Recording Media. *Annual Review of Materials Research*, 31(1):203–235, aug 2001. (Cited on page 83.)

[211] B. Trpišová and J. A. Brown. Ordering of Dipoles in Different Types of Microtubule Lattice. *International Journal of Modern Physics B*, 12(05):543–578, feb 1998. (Cited on page 83.)

[212] Elena Rufeil-Fiori, Natalia Wilke, and Adolfo J. Banchio. Dipolar interactions between domains in lipid monolayers at the air-water interface. *Soft Matter*, 12(21):4769–4777, 2016. (Cited on page 83.)

[213] Jean-Michel Caillol and Jean-Jacques Weis. Monte Carlo simulations of the two-dimensional dipolar fluid. *Molecular Physics*, 113(17-18):2487–2495, sep 2015. (Cited on page 83.)

[214] Heiko Schmidle, Carol K. Hall, Orlin D. Velev, and Sabine H. L. Klapp. Phase diagram of two-dimensional systems of dipole-like colloids. *Soft Matter*, 8(5):1521–1531, 2012. (Cited on page 83.)

[215] J. J. Weis. Orientational structure in a monolayer of dipolar hard spheres. *Molecular Physics*, 100(5):579–594, 2002. (Cited on page 83.)

[216] P. D. Duncan and P. J. Camp. Structure and dynamics in a monolayer of dipolar spheres. *J. Chem. Phys.*, 121(22):11322–11331, décembre 2004. (Cited on page 83.)

[217] E. Lomba, F. Lado, and J. J. Weis. Structure and thermodynamics of a ferrofluid monolayer. *Physical Review E*, 61(4):3838–3849, apr 2000. (Cited on page 83.)

[218] J.G. Brankov and D.M. Danchev. Ground state of an infinite two-dimensional system of dipoles on a lattice with arbitrary rhombicity angle. *Physica A: Statistical Mechanics and its Applications*, 144(1):128 – 139, 1987. (Cited on pages 84, 86 and 91.)

[219] S. Fazekas, J. Kertész, and D. E. Wolf. Two-dimensional array of magnetic particles: The role of an interaction cutoff. *Phys. Rev. E*, 68:041102, Oct 2003. (Cited on pages 84, 86 and 88.)

[220] V. A. Froltsov, R. Blaak, C. N. Likos, and H. Löwen. Crystal structures of two-dimensional magnetic colloids in tilted external magnetic fields. *Physical Review E*, 68(6):061406, dec 2003. (Cited on page 84.)

[221] S. W. de Leeuw, J. W. Perram, and E. R. Smith. Simulation of electrostatic systems in periodic boundary conditions. i. lattice sums and dielectric constants. *Proceedings of the Royal Society A: Mathematical, Physical and Engineering Sciences*, 373(1752):27–56, Oct 1980. (Cited on pages 84 and 95.)

[222] J.-J. Weis and D. Levesque. *Simple Dipolar Fluids as Generic Models for Soft Matter*, pages 163–225. Springer Berlin Heidelberg, Berlin, Heidelberg, 2005. (Cited on pages 85 and 95.)

[223] C. Holm and J.-J. Weis. The structure of ferrofluids: A status report. *Curr. Opin. Colloid Interface Sci.*, 10(3-4):133–140, OCT 2005. (Cited on page 93.)

[224] Dmitri V Talapin, Elena V Shevchenko, Christopher B Murray, Alexey V Titov, and Petr Král. Dipole-Dipole Interactions in Nanoparticle Superlattices. *Nano Letters*, 7(5):1213–1219, May 2007. (Cited on page 93.)

[225] W J Dulmage and W N Lipscomb. The crystal structures of hydrogen cyanide, HCN. *Acta Cryst.*, 4:330–334, July 1951. (Cited on page 93.)

[226] K. Aoki, B. J. Baer, H. C. Cynn, and M. Nicol. High-pressure raman study of one-dimensional crystals of the very polar molecule hydrogen cyanide. *Phys. Rev. B*, 42:4298–4303, Sep 1990. (Cited on page 93.)

[227] R. Tao and D. Xiao. Three-dimensional dielectric photonic crystals of body-centered-tetragonal lattice structure. *Applied Physics Letters*, 80(25):4702–4704, 2002. (Cited on page 93.)

[228] A Yethiraj, J H J Thijssen, A Wouterse, and A van Blaaderen. Large-Area Electric-Field-Induced Colloidal Single Crystals for Photonic Applications. *Advanced Materials*, 16(7):596–600, April 2004. (Cited on page 93.)

[229] Le He, Vikash Malik, Mingsheng Wang, Yongxing Hu, Francesca Edith Anson, and Yadong Yin. Self-assembly and magnetically induced phase transition of three-dimensional colloidal photonic crystals. *Nanoscale*, 4(15):4438–5, 2012. (Cited on page 93.)

[230] René van Roij. Theory of chain association versus liquid condensation. *Phys. Rev. Lett.*, 76:3348–3351, Apr 1996. (Cited on page 94.)

[231] Yan Levin. What happened to the gas-liquid transition in the system of dipolar hard spheres? *Phys. Rev. Lett.*, 83:1159–1162, Aug 1999. (Cited on page 94.)

[232] Philip J. Camp and G. N. Patey. Structure and scattering in colloidal ferrofluids. *Phys. Rev. E*, 62:5403–5408, Oct 2000. (Cited on page 94.)

[233] Peter D. Duncan and Philip J. Camp. Aggregation kinetics and the nature of phase separation in two-dimensional dipolar fluids. *Phys. Rev. Lett.*, 97:107202, Sep 2006. (Cited on page 94.)

[234] Sofia Kantorovich, Alexey O. Ivanov, Lorenzo Rovigatti, José Maria Tavares, and Francesco Sciortino. Nonmonotonic magnetic susceptibility of dipolar hard-spheres at low temperature and density. *Phys. Rev. Lett.*, 110:148306, Apr 2013. (Cited on page 94.)

[235] J. J. Weis and D. Levesque. Ferroelectric phases of dipolar hard spheres. *Phys. Rev. E*, 48:3728–3740, Nov 1993. (Cited on page 94.)

[236] Antti-Pekka Hynninen and Marjolein Dijkstra. Phase diagram of dipolar hard and soft spheres: Manipulation of colloidal crystal structures by an external field. *Phys. Rev. Lett.*, 94(13):138303, apr 2005. (Cited on pages 94, 99 and 105.)

[237] S H L Klapp and G N Patey. Crystallization of dipolar spheres: A discussion of second-order density functional theory. *J. Chem. Phys.*, 112(24):10949–10956, June 2000. (Cited on page 94.)

[238] SHL Klapp. Dipolar fluids under external perturbations. *Journal of Physics: Condensed Matter*, 17(15):R525–R550, 2005. (Cited on page 94.)

[239] B. Groh and S. Dietrich. Crystal structures and freezing of dipolar fluids. *Phys. Rev. E*, 63(2):021203, Jan 2001. (Cited on pages 94, 99, 100, 102 and 105.)

[240] H. B. Lavender, K. A. Iyer, and S. J. Singer. Global orientational order in model polar clusters. *J. Chem. Phys.*, 101(9):7856–7867, novembre 1994. (Cited on page 104.)

[241] F Cousin, E Dubois, and V Cabuil. Tuning the interactions of a magnetic colloidal suspension. *Phys. Rev. E*, 68(2):021405, August 2003. (Cited on page 105.)

[242] U Dassanayake, S Fraden, and A van Blaaderen. Structure of electrorheological fluids. *The Journal of Chemical Physics*, 112(8):3851–3858, February 2000. (Cited on page 105.)

[243] Anand Yethiraj, Alan Wouterse, Benito Groh, and Alfons van Blaaderen. Nature of an Electric-Field-Induced Colloidal Martensitic Transition. *Phys. Rev. Lett.*, 92(5):058301, February 2004. (Cited on page 105.)

[244] Priti S. Mohanty, Payam Bagheri, Sofi Nöjd, Anand Yethiraj, and Peter Schurtenberger. Multiple path-dependent routes for phase-transition kinetics in thermoresponsive and field-responsive ultrasoft colloids. *Physical Review X*, 5(1):011030, mar 2015. (Cited on page 105.)

[245] Antti-Pekka Hynninen and Marjolein Dijkstra. Phase behavior of dipolar hard and soft spheres. *Phys. Rev. E*, 72:051402, Nov 2005. (Cited on page 105.)

[246] G. T. Gao and X. C. Zeng. Freezing transition of a strongly dipolar simple fluid. *Phys. Rev. E*, 61:R2188–R2191, Mar 2000. (Cited on page 105.)

[247] Amit Goyal, Carol K Hall, and Orlin D Velev. Phase diagram for stimulus-responsive materials containing dipolar colloidal particles. *Phys. Rev. E*, 77(3):031401, March 2008. (Cited on page 105.)

[248] Philip C Brandt, Alexei V Ivlev, and Gregor E Morfill. Solid phases in electro- and magnetorheological systems. *J. Chem. Phys.*, 130(20):204513, May 2009. (Cited on page 105.)

[249] D. Gottwald, C. N. Likos, G. Kahl, and H. Löwen. Phase behavior of ionic microgels. *Phys. Rev. Lett.*, 92(6):068301, feb 2004. (Cited on page 105.)

[250] Dieter Gottwald, Gerhard Kahl, and Christos N. Likos. Predicting equilibrium structures in freezing processes. *J. Chem. Phys.*, 122(20):204503, may 2005. (Cited on page 105.)

[251] M. Watzlawek, C. N. Likos, and H. Löwen. Phase diagram of star polymer solutions. *Phys. Rev. Lett.*, 82(26):5289–5292, jun 1999. (Cited on page 105.)

[252] Dieter Kraft. Algorithm 733; TOMP—Fortran modules for optimal control calculations. *ACM Transactions on Mathematical Software*, 20(3):262–281, sep 1994. (Cited on page 111.)

[253] Robert B Wilson. *A simplicial algorithm for concave programming*. Ph.d. thesis, Harvard University, 1963. (Cited on page 111.)

[254] Jorge Nocedal and Stephen J Wright. *Numerical Optimization*. Springer Series in Operations Research and Financial Engineering. Springer New York, 2006. (Cited on pages 111, 112, 113 and 114.)

[255] Klaus Schittkowski. The nonlinear programming method of Wilson, Han, and Powell with an augmented Lagrangian type line search function - Part 2: An Efficient Implementation with Linear Least Squares Subproblems. *Numerische Mathematik*, 38(1):115–127, feb 1982. (Cited on page 113.)

[256] Richard P. Brent. *Algorithms for minimization without derivatives*. Prentice-Hall, Inc., Englewood Cliffs, New Jersey, 1973. (Cited on page 114.)

Auto-assemblage de particules dipolaires

Abrégé : Cette thèse couvre l'auto-assemblage de particules dipolaires (magnétiques/électriques). Ces systèmes sont abondants en physique de la matière condensée (molécules et nanoparticules magnétiques, particules colloïdales magnétiques, bactérie magnétotactique, etc.). Sur un plan fondamental, ils représentent un défi important en raison de l'anisotropie et de la longue portée de l'interaction de paire. Le principal objectif de ce travail de recherche est de prédire les microstructures de ces systèmes en tenant compte de façon adéquate de l'interaction complexe dipôle-dipôle ainsi que des effets stériques et ceux dus à un éventuel confinement. Comprendre et revisiter les interactions de filaments dipolaires tels que des aiguilles et des chaînes faites de billes dipolaires est une première étape importante de cette thèse. En effet, les chaînes sont les constituants élémentaires de nombreux systèmes dipolaires, notamment sous l'effet d'un champ magnétique extérieur appliqué. Ensuite, l'agrégation colonnaire des chaînes dipolaires est examinée, ce qui conduit aussi naturellement à l'étude des cristaux dipolaires massifs où une nouvelle phase est découverte. Le cas plus générique des chaînes hélicoïdales est discuté en considérant les situations limites que sont les chaînes linéaires droites et en zigzag. L'association des chaînes dipolaires, dans le cas bidimensionnel, forme des rubans, puis une monocouche avec un réseau hexagonal. La réponse non triviale d'un tel réseau à un champ magnétique perpendiculaire imposé est aussi étudiée. Il est démontré qu'un réseau rhombique peut être induit de cette façon. Finalement, la sédimentation de particules paramagnétiques dans une monocouche inclinée en présence d'un champ magnétique est explorée via une étude mêlant expériences, théorie et simulations. L'ordre induit par gravité s'avère être une voie prometteuse pour l'élaboration contrôlée de réseaux bidimensionnels.

Mots-clés : Interaction dipôle-dipôle, colloïdes, physique statistique, matière molle, systèmes granulaires

Self-assembly of dipolar particles

Abstract: This thesis covers the self-assembly of dipolar (magnetic/dielectric) particles. These systems are abundant in condensed matter physics (magnetic molecules and nanoparticles, magnetic colloidal particles, magnetotactic bacteria, etc). They also represent a fundamental challenge owing to the both long range and anisotropic nature of the pair interaction. The main objective of this research work is to predict the microstructures of these systems by properly handling the intricate dipole-dipole interaction combined with steric and possibly confinement effects. Understanding and revisiting the interaction of dipolar filaments such as needles or chains made up of dipolar beads is a first important achievement in this thesis. Indeed, the chains are the fundamental building blocks of many dipolar systems especially under applied external magnetic field. Then, the columnar aggregation of dipolar chains is investigated which naturally leads to the study of the bulk dipolar crystals. A new phase is discovered there. The more generic case of helical chains is discussed by considering limiting situations such as straight linear chains and zigzag chains. The association of dipolar chains in two-dimensions forms ribbons then a monolayer with triangular lattice symmetry. The interesting response of such a layer to an imposed perpendicular magnetic is addressed as well. It is demonstrated that rhombicity can be induced that way. Finally, sedimenting paramagnetic particles in a tilted monolayer in presence of a magnetic field are investigated by experiments, theory and simulations. The gravity-mediated ordering is found to be a promising route to elaborate tailored two-dimensional patterns.

Keywords: Dipole-dipole interaction, colloids, statistical physics, soft matter, granular systems